University of Belgrade
Faculty of Physics

Ana Hudomal

NUMERICAL STUDY OF QUANTUM GASES IN OPTICAL LATTICES AND IN SYNTHETIC MAGNETIC FIELDS

Doctoral Dissertation

Belgrade, 2020

Univerzitet u Beogradu
Fizički fakultet

Ana Hudomal

NUMERIČKO PROUČAVANJE KVANTNIH GASOVA U OPTIČKIM REŠETKAMA I U SINTETIČKIM MAGNETNIM POLJIMA

Doktorska disertacija

Beograd, 2020.

Thesis defense committee

Thesis advisor:

Dr. Ivana Vasić
Associate Research Professor
Institute of Physics Belgrade
University of Belgrade

Committee members:

Dr. Antun Balaž
Research Professor
Institute of Physics Belgrade
University of Belgrade

Dr. Milan Knežević
Full Professor
Faculty of Physics
University of Belgrade

Dr. Božidar Nikolić
Associate Professor
Faculty of Physics
University of Belgrade

Acknowledgments

The work presented in this thesis was carried out at the Institute of Physics Belgrade under the supervision of Dr. Ivana Vasić. I am indebted to Ivana for guidance and support in all aspects of my PhD studies. She introduced me to the exciting research field of ultracold quantum gases and passed on valuable knowledge that I will continue to use throughout my scientific career. I am especially grateful that I could rely on her whenever I had a question or encountered an obstacle. Having Ivana as a supervisor significantly contributed to making my PhD studies a positive experience.

During the work on this thesis I was employed at the Scientific Computing Laboratory (SCL) of the Institute of Physics Belgrade. I had many opportunities to participate in international collaboration and to attend schools and conferences. As many of my colleagues from SCL work in different fields, I could hear about a wide variety of research topics. I would like to thank Dr. Antun Balaž, the head of SCL, for giving me the opportunity to work in this stimulating environment, as well as for all his help and useful advice.

I wish to express my gratitude to Dr. Nicolas Regnault for the generous help he provided over the course of my PhD studies, in particular for enlightening discussions, tips for writing better code and valuable career advice. It is rare that someone devotes this amount of time to students from other institutions, and I greatly appreciate it.

I would also like to acknowledge all my other coauthors who contributed to the research presented in this thesis, Dr. Zlatko Papić, Dr. Hrvoje Buljan and Dr. Walter Hofstetter. I thank them all for fruitful collaboration.

Finally, I would like to thank my family and friends for their support and encouragement during the past five years. I am especially thankful to my parents who instilled in me an interest in science and nurtured my curiosity from an early age, which certainly had an impact on my choice of career and ultimately led to this thesis.

This work was financially supported by the Ministry of Education, Science, and Technological Development of the Republic of Serbia through the grant to the Institute of Physics Belgrade and through Projects ON171017, BKMH and TOP-FOP. I also acknowledge the contribution of the COST Action CA16221. Numerical simulations were performed on the PARADOX supercomputing facility at the Scientific Computing Laboratory, National Center of Excellence for the Study of Complex Systems, Institute of Physics Belgrade.

Numerical study of quantum gases in optical lattices and in synthetic magnetic fields

Abstract

Theoretical and experimental advances in the past few decades have resulted in the development of a new research field – quantum simulations with ultracold atoms. The main idea is to create a clean and precisely controllable quantum system which can then be used to simulate another system of interest – one that is not as easy to study experimentally. Although there are several different experimental platforms for quantum simulations, ultracold atoms are often used because they are especially well suited for this role. Progress in cooling and trapping techniques has enabled experimentalists to cool down atomic gases to quantum degeneracy and to easily manipulate them. These systems are well isolated from their environment and do not contain any impurities or defects. In particular, cold atoms in optical lattices – periodic potentials made by interference of laser beams – have shown to be an excellent platform for the study of various condensed matter systems. It is possible to realize different lattice geometries in the desired number of dimensions. The lattice size, number of atoms, temperature of the system and even the strength of interactions between atoms can be precisely tuned. Some of these parameters would be impossible to change in a real condensed matter system. The set of models which can be realized with ultracold atoms can be further extended by the use of Floquet engineering. In this approach, the system is exposed to a suitable time-periodic modulation. The resulting stroboscopic dynamics of this driven system can be related to a corresponding static model through Floquet theory. In particular, Floquet engineering was used to realize synthetic magnetic fields in systems of neutral cold atoms.

In this thesis we use numerical simulations and analytical insights to study dynamics of several relevant systems which have been the focus of recent experiments with ultracold atoms in optical lattices. One of the fundamental open questions that has gained lot of attention recently is related to the thermalization of a general isolated quantum system. Such systems are typically shown to thermalize in experiments, meaning that they lose all memory of their initial state. However, there are several notable counterexamples. In particular, a new class of systems which exhibit unusual thermaization has been recently discovered – the systems with special eigenstates called quantum many-body scars. Another long-standing problem is

realization of topologically nontrivial models with ultracold atoms. These systems usually require magnetic fields, whose effects can be mimicked by driving in a cold atom system. However, interactions between atoms are always present in a realistic system. The interplay of driving and interactions typically leads to the thermalization and additional considerations are necessary in order to identify regimes where this process is slow and allows for the preparation and measurement of an interesting topological state.

Recent experiments on Rydberg atom arrays have found evidence of anomalously slow thermalization and persistent density oscillations, which have been interpreted as a many-body analog of the phenomenon of quantum scars. Periodic dynamics and atypical scarred eigenstates have been obtained in a model with a "hard" kinetic constraint: the neighboring Rydberg atoms cannot be simultaneously excited. In the first part of this thesis we propose a realization of quantum many-body scars in a one-dimensional bosonic lattice model with a "soft" constraint in the form of density-assisted hopping. We discuss the relation of this model to the standard Bose-Hubbard model and possible experimental realizations using ultracold atoms. We find that this model exhibits similar phenomenology to the Rydberg atom chain, including weakly entangled eigenstates at high energy densities and the presence of a large number of exact zero energy states, with distinct algebraic structure.

Realization of strong synthetic magnetic fields in driven optical lattices has enabled implementation of topological bands in cold-atom setups. A milestone has been reached by a recent measurement of a finite Chern number based on the dynamics of incoherent bosonic atoms. The measurements of the quantum Hall effect in semiconductors are related to the Chern-number measurement in a cold-atom setup; however, the design and complexity of the two types of measurements are quite different. Motivated by these recent developments, in the second part of this thesis we investigate the dynamics of weakly interacting incoherent bosons in a two-dimensional driven optical lattice exposed to an external force, which provides a direct probe of the Chern number. We consider a realistic driving protocol in the regime of high driving frequency and focus on the role of weak repulsive interactions. We find that interactions lead to the redistribution of atoms over topological bands both through the conversion of interaction energy into kinetic energy during the expansion of the atomic cloud and due to an additional heating. Remarkably, we observe that the moderate atomic repulsion facilitates the measurement by flattening the distribution of atoms in the quasimomentum space. Our results also show that weak interactions can suppress the contribution of some higher-order nontopological terms in favor of the topological part of the effective model.

Strong interactions and strong synthetic magnetic fields, the main ingredients for the realization of fractional quantum Hall states, are already available in experiments on cold atom gases in periodically driven optical lattices. However, the interplay of the driving and interactions introduces detrimental heating, and for this reason it is still challenging to reach a fractional quantum Hall state in cold-atom setup. By performing a numerical study, in the third part of

this thesis we investigate stability of a bosonic Laughlin state in a small atomic sample exposed to driving. We identify an optimal regime of microscopic parameters, in particular interaction strength U and the driving frequency ω, such that the stroboscopic dynamics supports the basic $\nu = 1/2$ Laughlin state. Moreover, we explore slow ramping of a driving term and show that the considered protocol allows for the preparation of the Laughlin state on experimentally realistic time-scales.

Keywords: ultracold gases, quantum simulations, nonequilibrium dynamics, quantum scars, topological phases of matter, synthetic gauge fields, Floquet systems, exact diagonalization
Research field: Physics
Research subfield: Condensed matter physics
UDC number: 538.9

Numeričko proučavanje kvantnih gasova u optičkim rešetkama i u sintetičkim magnetnim poljima

Sažetak

Teorijski i eksperimentalni napredak u poslednjih nekoliko decenija doveo je do razvoja nove oblasti istraživanja – kvantnih simulacija sa ultrahladnim atomima. Osnovna ideja je da se napravi čist i precizno podesiv kvantni sistem koji se zatim može koristiti za simuliranje nekog drugog sistema od intresa koji nije tako jednostavan za eksperimentalno ispitivanje. Iako postoji nekoliko različitih platformi za kvantne simulacije, ultrahladni atomi se često koriste jer su izuzetno pogodni za ovu ulogu. Napredak u tehnikama za hlađenje i zarobljavanje atoma omogućio je eksperimentalnim fizičarima da ohlade atomske gasove do kvantne degeneracije i lako manipulišu njima. Ovi sistemi su dobro izolovani od svog okruženja i ne sadrže nikakve nečistoće ili defekte. Hladni atomi u optičkim rešetkama, periodičnim potencijalima nastalim interferencijom laserskih zraka, pokazali su se kao odlična platforma za proučavanje raznovrsnih sistema kondenzovane materije. Moguće je realizovati različite geometrije rešetke u željenom broju dimenzija. Veličina rešetke, broj atoma, temperatura sistema, čak i jačina interakcija između atoma mogu se precizno podešavati. Neke od ovih parametara ne bi bilo moguće promeniti u sistemu kondenzovane materije. Skup modela koji se mogu realizovati pomoću ultrahladnih atoma može se dalje proširiti korišćenjem Floke inženjeringa. U ovom pristupu, sistem je izložen pogodnoj vremenski periodičnoj modulaciji. Rezultirajuća stroboskopska dinamika ovog vođenog sistema može se povezati sa odgovarajućim statičkim modelom putem Floke teorije. Floke inženjering je korišćen i za realizaciju sintetičkih magnetnih polja u sistemima neutralnih hladnih atoma.

U ovoj tezi koristićemo numeričke simulacije i analitičke metode u cilju proučavanja dinamike nekoliko relevantnih sistema koji su bili u fokusu skorašnjih eksperimenata sa ultrahladnim atomima u optičkim rešetkama. Jedno od osnovnih otvorenih pitanja koje je nedavno privuklo dosta pažnje povezano je sa termalizacijom izolovanog kvantnog sistema u opštem slučaju. Takvi sistemi se u eksperimentima tipično termalizuju, što znači da gube svu memoriju o svom početnom stanju. Ipak, postoji nekoliko značajnih kontraprimera. Jedna nova klasa sistema sa atipičnom termalizacijom je nedavno otkrivena – to su sistemi sa posebnim svojstvenim stanjima nazvanim kvantni višečestični ožiljci. Još jedan dugogodišnji problem

predstavlja realizacija topološki netrivijalnih modela sa ultrahladnim atomima. Takvi sistemi obično zahtevaju magnetna polja, čiji efekti mogu da se oponašaju vođenjem u sistemu hladnih atoma. Međutim, interakcije između atoma su uvek prisutne u realističnim sistemima. Uzajamno dejstvo dejstvo vođenja i interakcija dovodi do termalizacije, pa su dodatna razmatranja neophodna da bi se identifikovali režimi u kojima je ovaj proces spor i dozvoljava pripremu i merenje interesantnih topoloških stanja.

Nedavni eksperimenti na nizovima Ridbergovih atoma pronašli su dokaze o anomalno sporoj termalizaciji i dugotrajnim oscilacijama gustine, što je bilo interpretirano kao višečestični analogon fenomena kvantnih ožiljaka. Periodična dinamika i atipična svojstvena stanja sa ožiljcima dobijeni su u modelu sa "jakim" kinetičkim ograničenjem: susedni Ridbergovi atomi ne mogu da budu istovremeno pobuđeni. U prvom delu ove teze predstavljena je realizacija kvantnih višečestičnih ožiljaka u jednodimenzionalnom bozonskom modelu na rešetki sa "slabim" ograničenjem u formi tunelovanja potpomognutim gustinom. Diskutovana je veza ovog modela sa standardnim Boze-Habard modelom i mogućnost njegove eksperimentalne realizacije sa ultrahladnim atomima. Ovaj model ispoljava sličnu fenomenologiju kao i lanac Ridbergovih atoma, uključujući slabo kvantno uvezana svojstvena stanja na velikim gustinama energije, kao i prisustvo velikog broja egzaktnih nultih energetskih stanja sa posebnom algebarskom strukturom.

Realizacija jakih sintetičkih magnetnih polja u vođenim optičkim rešetkama je omogućila implementaciju topoloških energetskih zona u sistemima hladnih atoma. Značajno postignuće predstavlja skorašnje merenje nenultog Černovog broja bazirano na dinamici nekoherentnih bezonskih atoma. Merenja kvantnog Holovog efekta u poluprovodnicima povezana su sa merenjem Černovog broja u eksperimentima sa hladnim atomima, ali se dizajn i kompleksnost ove dve vrste eksperimenata dosta razlikuju. Motivisani skorašnjim eksperimentima, u drugom delu ove teze ispitujemo dinamiku slabo interagujućih nekoherentnih bozona u dvodimenzionalnoj vođenoj optičkoj rešetki pod dejstvom spoljašnje sile, što omogućava direktno merenje Černovog broja. Razmaramo realističan protokol vođenja u režimu visoke frekvencije i fokusiramo se na ulogu slabih odbojnih interakcija. Pokazujemo da interakcije dovode do redistribucije atoma na topološke energetske zone kroz konverziju interakcione energije u kineticku energiju u toku širenja atomskog oblaka, kao i zbog dodatnog zagrevanja. Primećujemo da umereno odbijanje između atoma olakšava merenje putem poravnanja distribucije atoma u kvazi-impulsnom prostoru. Naši rezultati takođe pokazuju da slabe interakcije mogu da ponište doprinos nekih netopoloških članova višeg reda u korist topološkog dela efektivnog modela.

Jake interakcije i jaka sintetička magnetna polja, glavni sastojci za realizaciju frakcionog kvantnog Holovog efekta, već su dostupni u eksperimentima sa hladnim atomskim gasovima u periodično vođenim optičkim rešetkama. Međutim, uzajamno dejstvo vođenja i interakcija izaziva neželjeno zagrevanje, pa je iz tog razloga ostvarivanje frakcionog kvantnog Holovog stanja u sistemu hladnih atoma i dalje veliki izazov. Uz pomoć numeričkih simulacija, u trećem

delu ove teze istražujemo stabilnost bozonskih Laflinovih stanja u malom atomskom uzorku pod dejstvom periodičnog vođenja. Pronalazimo optimalan režim mikroskopskih parametara, jačinu interakcija U i frekvenciju vođenja ω, takvih da stroboskopska dinamika podržava osnovno $\nu = 1/2$ Laflinovo stanje. Pored toga, istražujemo postepeno uključivanje člana koji opisuje vođenje i pokazujemo da razmatrani protokol dozvoljava pripremu Lafinovog stanja na eksperimentalno relevantnim vremenskim skalama.

Ključne reči: ultrahladni gasovi, kvantne simulacije, neravnotežna dinamika, kvantni ožiljci, topološke faze materije, sintetička gejdž polja, Floke sistemi, egzaktna dijagonalizacija
Naučna oblast: Fizika
Uža naučna oblast: Fizika kondenzovanog stanja
UDK broj: 538.9

Contents

Thesis defense committee . . . i
Acknowledgments . . . iii
Abstract . . . v
Sažetak . . . ix
List of figures . . . xiv
List of tables . . . xvii

1 Introduction **1**
1.1 Quantum simulations . . . 1
1.2 Bose-Hubbard model . . . 3
1.3 Nonequilibrium dynamics . . . 5
1.4 Synthetic magnetic fields . . . 7
1.5 Floquet engineering . . . 9
1.6 This thesis . . . 12

2 Quantum scars of bosons with correlated hopping **15**
2.1 Models and their Hilbert spaces . . . 17
2.1.1 Models . . . 17
2.1.2 Graph structure and bipartite lattice . . . 19
2.2 Dynamics and entanglement properties . . . 22
2.2.1 Level statistics and entanglement entropy . . . 22
2.2.2 Global quenches . . . 24
2.3 Quantum scars in $\hat{H}_1$ and $\hat{H}_3$ models . . . 26
2.3.1 Perfect revivals in the $\hat{H}_3$ model . . . 26
2.3.2 Cluster approximations for the $\hat{H}_1$ model . . . 28
2.3.3 Generalization to other clusters . . . 34
2.4 Zero modes . . . 36
2.5 Conclusions . . . 39

3 Dynamics of weakly interacting bosons in optical lattices with flux **41**
3.1 Model and method . . . 42
3.1.1 Effective Floquet Hamiltonian . . . 43
3.1.2 Band structure . . . 45
3.1.3 Dynamics of incoherent bosons . . . 46

3.2 Noninteracting case . . . 47
3.3 Interacting case . . . 50
3.3.1 Anomalous drift and dynamics of band populations . . . 50
3.3.2 Real and momentum-space dynamics . . . 53
3.3.3 Staggered detuning . . . 56
3.4 Conclusions . . . 57

4 Bosonic fractional quantum Hall states in driven optical lattices 59
4.1 Model and method . . . 60
4.1.1 Driven model . . . 60
4.1.2 Particle-entanglement spectra . . . 63
4.2 Driven dynamics . . . 64
4.2.1 Heating . . . 65
4.2.2 The stroboscopic time-evolution operator . . . 66
4.3 Slow ramp . . . 68
4.3.1 Model . . . 68
4.3.2 Results . . . 69
4.4 Conclusions . . . 71

5 Conclusions 73

A Relative magnitude of the hopping coefficients 77

B Derivation of fidelity in the extended cluster approximation 79

C The effective model from Chapter 3 81
C.1 Real space . . . 81
C.2 Momentum space . . . 83

D Description of incoherent bosons 87

E Initial quadratic regime 89

F Effects of interactions 91
F.1 Energy . . . 91
F.2 Momentum-space density distribution . . . 92

G The effective model from Chapter 4 95

Bibliography 97

Biography of the author 109

List of figures

1.1 2D and 3D square optical lattice . . . 3
1.2 Superfluid and Mott insulator state . . . 5
1.3 Harper-Hofstadter model . . . 8
1.4 Energy spectrum of the Harper-Hofstadter model . . . 8
1.5 Harper-Hofstadter model with ultracold atoms in an optical lattice . . . 10

2.1 Connectivity of the Hilbert space . . . 19
2.2 Level statistics and entanglement . . . 23
2.3 Dynamics of quantum fidelity and entanglement entropy . . . 25
2.4 Evolution of local observables . . . 26
2.5 Minimal and extended clusters . . . 28
2.6 Comparison of the full dynamics against the minimal cluster and extended cluster approximation schemes . . . 30
2.7 Cluster approximations . . . 31
2.8 First peak height . . . 32
2.9 Evolution of the probability to remain inside the minimal cluster . . . 33
2.10 Non-ergodic eigenstates . . . 34
2.11 Evolution of entanglement entropy for three different translation-invariant initial states . . . 36
2.12 Bipartite graph for $\hat{H}_1$ and $L = N_\mathrm{p} = 4$ . . . 38

3.1 Schematic representation of the model . . . 44
3.2 Energy bands of the effective Hamiltonians . . . 45
3.3 Anomalous drift . . . 49
3.4 Evolution of the filling factor . . . 50
3.5 Effects of interactions . . . 51
3.6 Evolution of the band populations and dependence of the exponential decay coefficients on the interaction strength . . . 52
3.7 Real-space density distribution in the noninteracting case . . . 53
3.8 Real-space density distribution in the interacting case . . . 54
3.9 Atomic cloud width . . . 54

3.10 Comparison of anomalous drifts obtained with different Hamiltonians, evolution of the inverse participation ratio in momentum space and lowest band Chern number . . . 55
3.11 Lowest band Chern numbers for different values of staggered detuning . . . 57

4.1 Lattice geometry . . . 61
4.2 Energy and particle-entanglement spectrum . . . 63
4.3 Normalized total energy and particle-entanglement entropy . . . 66
4.4 Properties of the eigenstates of the stroboscopic time-evolution operator . . . 67
4.5 Expectation value of the effective Hamiltonian, particle-entanglement gap and overlap with the target state . . . 69
4.6 Low-lying part of the particle-entanglement spectra . . . 70
4.7 Evolution of the particle-entanglement gap . . . 71

A.1 Evolution of quantum fidelity and entanglement entropy for Hamiltonians $\hat{H}_1$, $\hat{H}_{1a}$ and $\hat{H}_{1b}$ . . . 78

C.1 Energy subbands of the effective Hamiltonian in momentum space . . . 85

E.1 Population in higher bands . . . 89

F.1 Kinetic and interaction energy per particle . . . 92
F.2 Momentum-space density distribution . . . 93

List of tables

2.1 Number of zero-energy states for the Hamiltonian $\hat{H}_1$ 37
2.2 Number of zero-energy states for the Hamiltonian $\hat{H}_2$ 37
2.3 Difference between the number of green and red configurations and the number of zero-energy states 39

3.1 Four different cases of the bosonic dynamics 48

4.1 Counting of modes in the particle-entanglement spectrum of the Laughlin state . 64

Chapter 1

Introduction

When atoms are cooled down to sufficiently low temperatures, their quantum statistics starts to play an important role and the differences between bosons and fermions become apparent. In the case of bosons, cooling leads to macroscopic occupation of a single quantum state – the Bose-Einstein condensate (BEC). More than 70 years after its first theoretical prediction in 1924, BEC was finally experimentally achieved in 1995, when the atoms were cooled down to 170 nK [1]. This was made possible by advances in laser and evaporative cooling techniques during the previous decades, as well as magnetic and optical trapping. These techniques were later also applied to fermionic atoms, molecules, and mixtures of different atomic species, successfully cooling down these systems to quantum degeneracy. During the last two decades since BEC was first attained, significant progress has been made in both theoretical and experimental research on quantum gases. There are many possible applications of ultracold quantum gases. They can be used for precision measurements, and can also serve as a platform for quantum computing and quantum simulations.

1.1 Quantum simulations

Quantum simulators were first envisioned by Feynman in 1982 [2, 3]. The idea was to create a clean and highly controllable quantum system that can be used to simulate another complex quantum system described by an equivalent Hamiltonian. The need for quantum computing and quantum simulations has arisen due to computational limits of classical computers. While it is theoretically possible to find the exact eigenvalues and eigenstates for any finite-dimensional interacting quantum many-body system, the Hilbert space dimensions of such systems grow exponentially with the system size, which quickly makes it impossible to store the necessary data in the memory of even the most advanced modern supercomputers. Exact numerical calculations are therefore limited to the smallest systems consisting only of tens of particles and

lattice sites, which sometimes makes it very hard to extrapolate the results to the thermodynamic limit. Feynman's proposal was to use a computer which operates on quantum-mechanical laws to solve quantum-mechanical problems. Unlike a classical computer, in this case the number of necessary computer elements – quantum bits – scales linearly with the size of the system of interest. Additionally, a quantum computer is probabilistic – there is no unique output for each input. Instead, such a computer returns several outputs with different probabilities, which is expected as it is actually performing a quantum measurement.

Quantum simulators are a similar yet distinct concept. Unlike universal quantum computers, which could in theory be programmed to execute any possible algorithm, but are still years or even decades away from practical applications [4], quantum simulators are designed for a specific task and are therefore easier to build. There is already a variety of their experimental realizations on different platforms, for example using neutral cold atoms [5, 6], trapped ions [7], superconducting circuits [8], photonic systems [9] or nitrogen-vacancy centers in diamond [10, 11]. Some of the phenomena simulated in this way are quantum magnetism [12], strange metal phase of high-temperature superconductors [13, 14], decay of a Higgs particle [15], black-hole radiation [16] and photosynthesis [17]. Quantum simulations have shown to be useful in a wide range of different research fields, including condensed-matter physics, high-energy physics, cosmology and quantum chemistry. They could also be applied to classical problems which require large computing power. While universal quantum computers are very prone to computation errors, as each particle needs to be set to a precisely defined quantum state, this is not the case for quantum simulators where the resulting quantity is typically an average over the whole system and thus less sensitive to the exact state of an individual particle.

In particular, ultracold atoms in optical lattices provide a perfect platform for quantum simulations of various condensed-matter phenomena [5, 18]. Here, the optical lattice plays the role of the crystal lattice in solid-state systems, while the atoms play the role of the electrons. Optical lattice is a spatially periodic potential created by interference of two counter-propagating laser beams. Schematic representations of two-dimensional and three-dimensional optical lattices are shown in Fig. 1.1. Cold atoms can be trapped inside the lattice by the optical dipole force. Various optical-lattice geometries can be realized depending on the intensity and relative angles between interfering laser beams. The strength of interactions between the atoms can be tuned using Feshbach resonances. The possibility to precisely adjust all microscopic parameters of the system can be used to create exotic phases of matter that are not observed in nature, or to experimentally probe quantities that are otherwise not accessible in condensed-matter systems.

Two seminal condensed-matter models which were realized with ultracold atoms are the Bose-Hubbard and the Fermi-Hubbard model. The experimental setup is similar in both cases; a dilute atomic gas, typically consisting of alkali atoms (Li, Na, K, Rb, Cs), is placed inside a magneto-optical trap, cooled down to low temperatures and exposed to an optical lattice po-

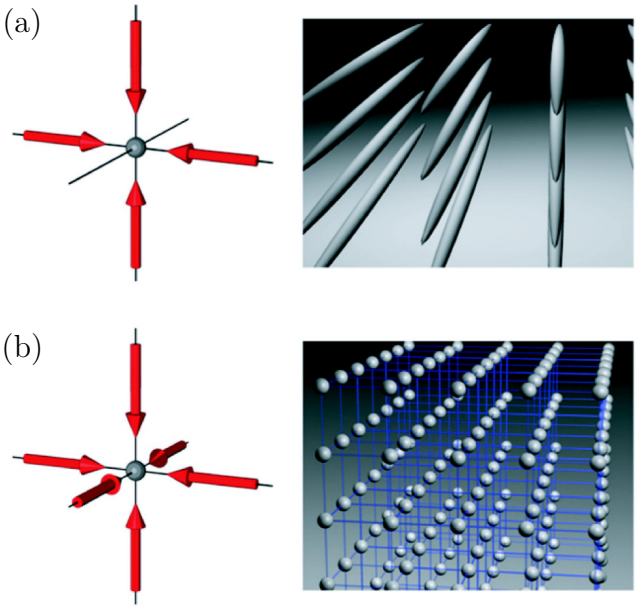

Figure 1.1: Schematic of a two-dimensional (a) and three-dimensional (b) square optical lattice. Adapted from Ref. [5].

tential. The exact model which is realized, Bose- or Fermi-Hubbard, depends on the bosonic or fermionic nature of the atomic species which is used. Bosonic atoms are used more often as they are easier to cool down to quantum degeneracy, given that their ground state is a Bose-Einstein condensate. Early experiments have studied quantum phase transitions and characterized different phases of matter in these two models. Another topic that was experimentally explored with these models is their nonequilibrium dynamics. In recent experiments, Bose-Hubbard and Fermi-Hubbard models serve as a foundation for the realization of other generalized and more complex models.

1.2 Bose-Hubbard model

Interacting spinless bosons in a periodical potential are described by the Bose-Hubbard Hamiltonian [19]. This model has only two parameters; hopping amplitude J which determines the probability for a particle to tunnel to a neighbouring site, and the strength of interactions U between two particles on the same site which can be either repulsive ($U > 0$) or attractive ($U < 0$). The Bose-Hubbard Hamiltonian can be written as

$$\hat{H}_{\mathrm{BH}} = -J \sum_{\langle l,m \rangle} \left(\hat{a}_l^\dagger \hat{a}_m + \text{H. c.} \right) + \frac{U}{2} \sum_l \hat{n}_l \left(\hat{n}_l - 1 \right), \tag{1.1}$$

where $\hat{a}_l^\dagger$ and $\hat{a}_l$ are creation and annihilation operators that create and annihilate a particle at the lattice site with index l, $\hat{n}_l = \hat{a}_l^\dagger \hat{a}_l$ is the particle number operator, and the label $\langle l, m \rangle$ stands for nearest neighbors. This model was derived using the single-band tight-binding ap-

proximation [5]. The Hamilatonian shown here is given by a general expression for an arbitrary number of dimensions. The equation for a specific number of dimensions can be written in a similar manner, with potentially different hopping amplitudes in different directions. The Bose-Hubbard Hamiltonian has a global $U(1)$ gauge symmetry and all the symmetries of the underlying lattice. As the occupancy of a single lattice site is not limited for bosonic particles, the Hilbert space dimension grows with the system size as

$$\dim\mathcal{H} = \binom{N+L-1}{N}, \tag{1.2}$$

where N is the number of particles and L is the number of lattice sites.

Although the Bose-Hubbard Hamiltonian [19] was first formulated for solid state systems as generalization of the (Fermi-)Hubbard model [20], the closest experimental realization of this model is provided by ultracold bosonic atoms in an optical lattice. The necessary conditions for the approximation to be valid are that the atoms are cooled down to a low enough temperature, so that only the lowest energy band is significantly occupied, and that the lattice is deep enough, thus making the Wannier functions sufficiently localized at each lattice site. As the atoms interact by short-range Van der Waals forces and there are no long-range Coulomb interactions between neutral atoms, the onsite interaction term is sufficient to describe the interactions in this system. Long-range dipolar interactions can be avoided by choosing an atomic species without a dipolar moment.

The phase diagram of the Bose-Hubbard model consists of the superfluid phase and the Mott insulator phase, depending on the ratio J/U and the filling factor $\nu = N/L$ [19]. In the superfliuid phase where the hopping term is dominant over the interaction term, the particles are completely delocalized across all lattice sites. The ground state in this phase is a BEC and can be described by a single Bloch wavefunction. It is characterized by long-range phase coherence. This state can be described by the Gross-Pitaevskii equation – a nonlinear Schrödinger-like equation. In contrast, the interaction term is dominant in the Mott insulator phase and in the ground state an integer number of particles is localized at each lattice site. This is a strongly-correlated quantum many-body state. In the limit $U \to 0$, it is a product of local Fock states at each site. Unlike the superfluid state, the Mott insulator state is incompressible, as particle number fluctuations are energetically very costly. There is no more phase coherence in the Mott insulating phase. Instead, there are long-range particle number correlations.

The phase transition between these two phases has been experimentally observed in an ultracold quantum gas [21]. In this experiment, the ratio J/U was varied by increasing the lattice potential depth, which resulted in decreased hopping amplitude J and increased onsite interaction strength U. After setting the desired ratio, the confining potential was turned off and the atomic cloud was left to expand freely in the optical lattice potential. The phase coherence between different lattice sites was visible in the resulting interference pattern. The

absence of interference maxima marked the onset of the Mott insulating phase. A schematic of the two states and the corresponding interference patterns are given in Fig. 1.2. Experiments like this one and their excellent agreement with theoretical predictions have confirmed that the Bose-Hubbard model is indeed realized with cold atoms in optical lattices.

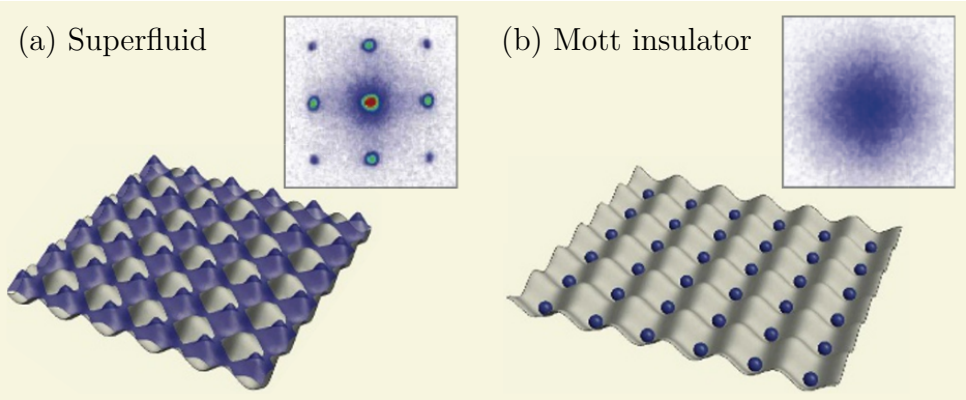

Figure 1.2: Schematic of a superfluid state (a) and a Mott insulator state (b) in an optical lattice and corresponding interference patterns after expansion. Adapted from Ref. [21].

There are several generalizations of this model which include additional potentials, long-range density-density or dipolar interactions, next-nearest-neighbour and other hopping terms, interaction- or density-induced hopping terms, particles with spin, as well as the Bose-Fermi-Hubbard which describes a mixture of bosonic and fermionic particles. The Bose-Hubbard Hamiltonian will be the starting model for all the studies in this thesis. We will be interested in systems with density-dependent hopping terms and systems with additional time-dependent potentials – the so-called driven systems.

1.3 Nonequilibrium dynamics

While the properties of quantum systems in equilibrium are generally well understood, nonequilibrium dynamics of such systems is still an active field of research. A system can be taken out of equilibrium by changing its Hamiltonian, either by a sudden quench or by continuously ramping one or more parameters. Systems in contact with a thermal reservoir are generally expected to thermalize, but it is not clear whether a general isolated quantum system should ever reach thermal equilibrium. Ultracold atoms provide an excellent experimental platform for the study of quantum many-body physics out of equilibrium, as they are both precisely tunable and well isolated from their environment [22]. In such experiments, the system is typically first prepared in the ground state $|\psi_0\rangle$ of some initial Hamiltonian $\hat{H}_0$ and then evolved under a different Hamiltonian $\hat{H}$, which may or may not be time-dependent.

The main question is through which mechanism and under which conditions isolated quantum systems initially out of equilibrium evolve towards a state in thermal equilibrium. This

question has been studied in a variety of experiments on quantum gases [23–29]. Complete thermalization has been observed in some of these experiments [24, 28]. The final thermalized state is independent of the initial state – all memory is lost during the process of thermalization. However, this loss of information is somewhat surprising because of the fact that the time-evolution operator $\hat{U}(t) = \mathrm{e}^{-i\hat{H}t}$ is unitary and therefore preserves the system in a pure quantum state. A potential answer is provided by the eigenstate thermalization hypothesis (ETH) [30–33]. ETH states that thermalization happens already at the eigenstate level and that this becomes visible in the expectation values of certain observables during time evolution, due to dephasing between eigenstates which constitute the initial state. In other words, even though the system stays in a pure quantum state indefinitely, the results of measurements will appear thermalized after long enough time.

Let the initial state be a superposition of eigenstates of the Hamiltonian $\hat{H}$ from an energy range $E_{\mathrm{min}} \leq E \leq E_{\mathrm{max}}$. If ETH is obeyed for a certain observable $\hat{\mathcal{O}}$, its diagonal matrix elements in the basis of $\hat{H}$, $\mathcal{O}_{ii} = \langle i|\hat{\mathcal{O}}|i\rangle$, will be approximately a smooth function of energy $\mathcal{O}_{ii}(E)$ over the energy range of interest. ETH then predicts that the expectation value of the observable $\hat{\mathcal{O}}$ after thermalization will be equal to the value predicted by the microcanonical ensemble over the same energy range. A single eigenstate is sufficient to predict the thermal expectation value, as all the eigenstates from the energy range in question would lead to the same prediction. ETH typically holds for few-body observables, both local and nonlocal, which are the ones usually measured in experiments. Although ETH has not been analytically proven for a general interacting quantum system, it was shown to be valid in a number of numerical studies [33]. Analytical proofs exist for several specific cases.

However, there are several types of systems which do not obey ETH. Some of them completely avoid thermalization. Two well known examples are integrable systems [34] and systems which exhibit many-body localization [35]. Integrable systems typically have a large number of conserved quantities which constrain their evolution and prevent them from eventually thermalizing. Many-body localization (MBL) requires random disorder in the system and is characterized by the emergence of local integrals of motion. These local integrals of motion preserve the information about the initial state. MBL was shown to be robust with respect to perturbations. Signatures of MBL have been observed in multiple experiments [36–39].

An useful diagnostic of thermalization is the bipartite entanglement entropy [40, 41], a quantity which measures the degree of entanglement between two complementary subsystems labeled A and B:

$$S_{\mathrm{A}} = -\mathrm{Tr}\left(\rho_{\mathrm{A}} \ln \rho_{\mathrm{A}}\right). \tag{1.3}$$

The entanglement entropy is defined for a certain pure state $|\psi\rangle$. In the preceding equation, $\rho_{\mathrm{A}} = \mathrm{Tr}_{\mathrm{B}}|\psi\rangle\langle\psi|$ is the reduced density matrix of the subsystem A. In contrast to thermalizing systems where the entanglement entropy of highly excited eigenstates typically scales as the

volume of the subsystem A, in the MBL phase it obeys the so-called "area law" – it is proportional to the area of the boundary between the subsystems [35, 41, 42]. Additionally, during the nonequilibrium dynamics the entanglement entropy grows logarithmically with time, instead of the usual linear or power-law growth [43–45].

Another type of systems with unusually slow thermalization has emerged in recent years – quantum many-body scarred systems. It was shown that these systems are neither integrable nor many-body localized. This phenomenon was first observed experimentally in a quantum simulator with an array of Rydberg atoms [46]. While the system exhibited the expected thermalizing behavior for most initial states, preparing it in certain initial states surprisingly resulted in persistent density oscillations – the system kept returning to its initial state. Theoretical explanation for such behavior has followed soon after the experimental results [47, 48]. It was shown that the states with unusual dynamics are superpositions of atypical eigenstates dubbed "qunatum many-body scars". These eigenstates have significantly smaller entanglement entropies than the other eigenstates at the same energy scale. Their name was inspired by the phenomenon of quantum scars in noninteracting systems, where some eigenstates of a quantum system have enhanced probability density in vicinity of unstable periodic orbits of the corresponding classical system [49]. In the case of quantum many-body scars, the eigenstates are concentrated in certain regions of the Hilbert space instead of real space. Such atypical eigenstates have been subsequently found in a variety of different systems [50–67]. It is however still not completely clear what are the necessary conditions for their existence. A particular realization of quantum many-body scars in a one-dimensional model of bosons with correlated hopping will be the topic of the first part of this thesis.

Systems which slowly thermalize or do not thermalize at all could have several practical applications. Most importantly, they could be useful for quantum computing, where it is of crucial importance to preserve the system in a particular quantum state. Another application would be to extend the available timescales in experiments on exotic quantum phases which are currently hindered by rapid thermalization.

1.4 Synthetic magnetic fields

Strong magnetic fields are required for many phenomena in condensed matter physics, such as integer and fractional quantum Hall effects. The Harper-Hofstadter model [68] is a two-dimensional model which describes a charged particle in a periodic potential and perpendicular magnetic field. Its Hamiltonian can be written as

$$\hat{H}_{\mathrm{HH}} = -J \sum_{l,m} \left(\mathrm{e}^{-2i\pi m\alpha} \hat{a}^{\dagger}_{l+1,m} \hat{a}_{l,m} + \hat{a}^{\dagger}_{l,m+1} \hat{a}_{l,m} + \mathrm{H.\ c.} \right), \tag{1.4}$$

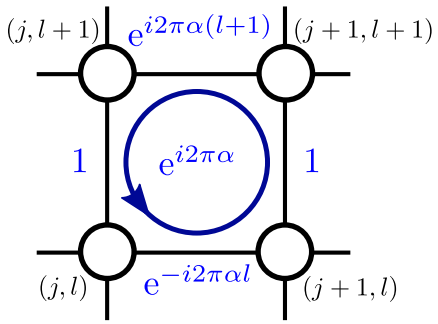

Figure 1.3: Schematic representation of the Harper-Hofstadter model.

where the parameter α is the magnetic flux through one plaquette in the units of flux quanta h/q. The effects of magnetic field are encoded in the position-dependent complex hopping coefficients $e^{-2i\pi m\alpha}$. A particle hopping in counterclockwise direction along the smallest closed loop acquires a phase $2\pi\alpha$, as shown in Fig. 1.3, in analogy to a charged particle in magnetic field which would acquire the Aharonov-Bohm phase. The energy spectrum of the Harper-Hofstadter model has an interesting fractal structure, as can be seen in Fig. 1.4. The number of energy bands depends on α; when α is a rational number the number of bands is equal to its denominator. For example, there are three energy bands for $\alpha = 1/3$, see Fig. 1.4(a), as well as for $\alpha = 2/3$. The plot of energy versus α shown in Fig. 1.4(b) is called the "Hofstadter butterfly".

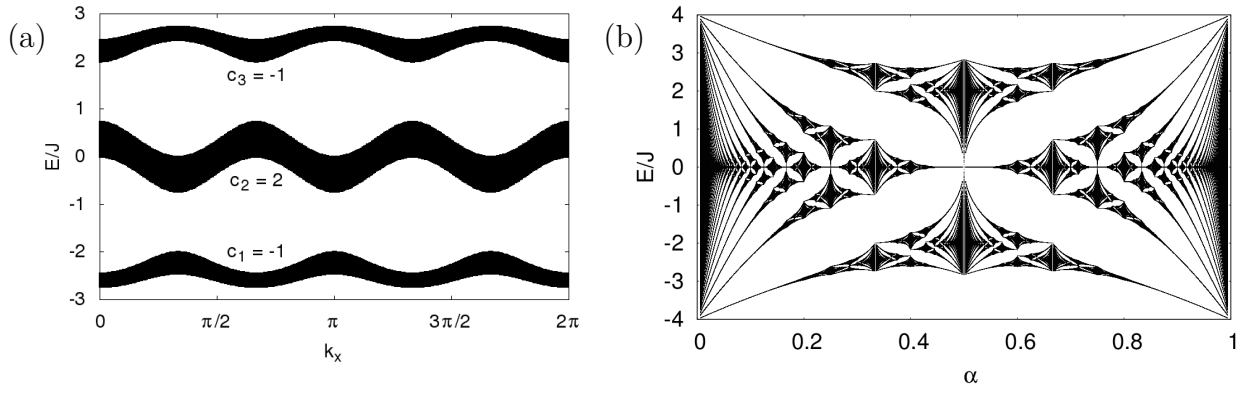

Figure 1.4: (a) Energy spectrum for $\alpha = 1/3$. (b) "Hofstadter butterfly" [68] – energy spectrum of the Harper-Hofstadter model.

In the seminal TKNN paper [69] it was shown that the quantization of the Hall conductivity observed in the integer Hall effects can be directly related to the topological index of the microscopic model (1.4) – the Chern number. The Chern number is defined for a single energy band and is always an integer. It is also a topological invariant, which means that it is insensitive to local deformations and disorder, and changes only when the global topological properties of the system change, i.e. when the band gap closes. The Chern numbers for the three energy bands of the Harper-Hofstadter model with $\alpha = 1/3$ are shown in Fig. 1.4(a). Topological concepts in physics have become an increasingly important field of research in the last few

decades. In 2015, the deflection of an atomic cloud in an optical lattice with synthetic magnetic field as a response to external force was used to experimentally measure the Chern number in a non-electronic system for the first time [70].

The Chern number is closely related to the Berry curvature and Berry phase [71]. It is defined as the integral of the Berry curvature [72] over the first Brillouin zone divided by 2π,

$$c_n = \frac{1}{2\pi} \int_{\mathrm{FBZ}} \mathbf{\Omega}_n(\mathbf{k}) \cdot d\mathbf{S}, \tag{1.5}$$

where n denotes the band number and the Berry curvature is $\mathbf{\Omega}_n(\mathbf{k}) = i\nabla_{\mathbf{k}} \times \langle u_n(\mathbf{k}) | \nabla_{\mathbf{k}} | u_n(\mathbf{k}) \rangle$, expressed in terms of eigenstates $|u_n(\mathbf{k})\rangle$. The Berry phase is a geometric phase that a particle acquires when it makes a closed loop in some parameter space and can be thought of as the analogue of the Aharonov-Bohm phase, while the Berry curvature is then analogous to the magnetic field.

If one wants to simulate systems with magnetic fields using cold atoms, the problem arises from the fact that atoms are charge-neutral and therefore do not feel the Lorentz force. These effects have to be included in some artificial way, by engineering the so-called synthetic magnetic fields. One of the first ideas was to take advantage of the similarity between the Lorentz force and the Coriolis force. This was experimentally realized in 2000 using rotating quantum gases [73], where the appearance of quantized vortices was observed, which is a property of superfluids and superconductors in magnetic field. However, this experimental realization poses several difficulties. Maximal rotation velocity achievable in the experiment is technically limited and it is difficult to realize a stable rotating optical lattice. All of this has made it impossible to obtain strong synthetic magnetic fields required for quantum Hall effects using rotational approach. In 2009, after years of efforts, synthetic magnetic potentials for neutral atoms were implemented by exploiting atomic coupling to a suitable configuration of external lasers [74, 75]. These techniques were further extended to optical lattices, leading to the realization of strong, synthetic, magnetic fields. As a result, important condensed-matter models – the Harper-Hofstadter (1.4) and the Haldane model [76] – are nowadays available in cold-atom setups [77–80]. The key property of these models is their non-trivial topological content.

1.5 Floquet engineering

One way to enrich the set of models which can be realized using cold atoms in optical lattices is by adding time-periodic perturbations to the system. Such systems are called driven systems. This can be done either by lattice shaking – periodic modulation of the lattice position, or through laser-assisted tunneling, which results in a periodic modulation of the lattice potential. Both methods have been used in present-day cold-atom realizations of important topological models [77–79], where they were necessary in order to engineer synthetic magnetic fields. A

schematic representation of the experimental setup [77] which realized the famous Harper-Hofstadter model [68] given by Eq. (1.4) can be seen in Fig. 1.5. In this thesis we will mostly consider laser-assisted tunneling. The resulting time-dependent Hamiltonian can in that case be written as

$$\hat{H}(t) = \hat{H}_0 + \hat{V}(t), \tag{1.6}$$

where $\hat{H}_0$ is typically the underlying Bose-Hubbard Hamiltonian $\hat{H}_{\mathrm{BH}}$ and $\hat{V}(t)$ is a time-periodic modulation of the lattice potential with frequency ω and amplitude κ

$$\hat{V}(t) = \sum_i \hat{n}_i V_i(t). \tag{1.7}$$

Here i is the lattice site index and $\hat{n}_i$ is the particle number operator for that lattice site.

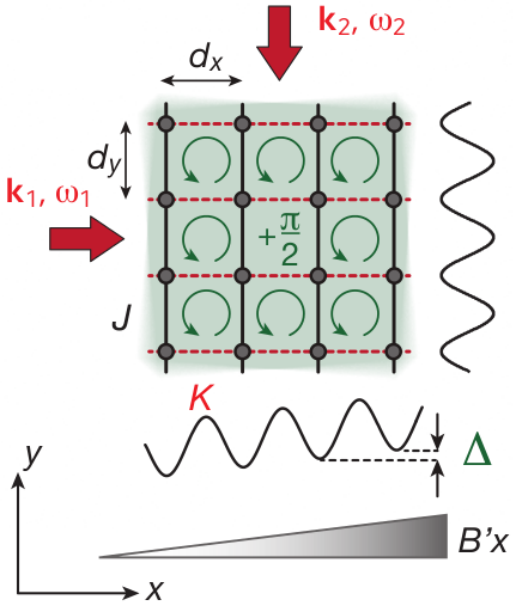

Figure 1.5: Schematic of the experimental setup which implements the Harper-Hofstadter model using ultracold atoms in an optical lattice. Synthetic magnetic field is realized through Floquet engineering. Hopping along the x-axis is first inhibited by a magnetic field gradient B' which generates an offset Δ between neighboring sites. The hopping is then restored using two additional pairs of laser beams with wave vectors $\mathbf{k}_1$, $\mathbf{k}_2$ and frequencies ω_1, ω_2. Laser-assisted tunneling adds a complex phase to the hopping coefficients. The bare hopping amplitude is denoted by J and the complex hopping amplitude by K. This setup mimics the complex phase acquired by a charged particle moving in a magnetic field. In this model, a particle hopping in counterclockwise direction around a single plaquette acquires a phase $\pi/2$, which makes it equivalent to the Harper-Hofstadter model with $\alpha = 1/4$. Adapted from Ref. [77].

Using Floquet theory [81], a periodically driven system can be related to a time-independent effective Hamiltonian. A properly chosen periodic modulation can result in an effective Hamiltonian which corresponds to a relevant condensed-matter system. The mapping is known as Floquet engineering and its important features in the context of optical lattices are discussed in

Refs. [82–88]. The basis of this mapping is Floquet's theorem [89], which is applicable to time-periodic Hamiltonians, analogously to the more famous Bloch's theorem for systems periodic in space. Ultracold quantum gases provide an optimal platform for Floquet engineering, as these systems are usually isolated from their environment, which inhibits dissipative processes, and the highly-controllable parameters of the system can be easily periodically modulated.

Analogously to the Bloch wave states in spatially periodic systems, Floquet states can be written as

$$|\psi_n(t)\rangle = \mathrm{e}^{-i\epsilon_n t}|u_n(t)\rangle, \tag{1.8}$$

where ϵ_n are the quasienergies and $|u_n(t)\rangle = |u_n(t+T)\rangle$ are the time-periodic Floquet modes which have the same period $T = 2\pi/\omega$ as the Hamiltonian $\hat{H}(t)$. As in the rest of this thesis, here we work in the units where $\hbar = 1$. Quasienergies ϵ_n are only defined up to integer multiples of the driving frequency ω, similarly to the quasimomenta which are only defined inside the first Brillouin zone. The Floquet states are the eigenstates of the evolution operator over one driving period $\hat{U}(T, 0)$. When a system governed by a time-periodic Hamiltonian is observed stroboscopically – at times that are integer multiples of the period, it behaves as if it was governed by some time-independent effective Hamiltonian. The dynamics during one period – micromotion – is described by another periodic operator, the so-called kick operator that has the same periodicity as the original time-dependent Hamiltonian. The time-evolution operator corresponding to the Hamiltonian (1.6) can be represented as

$$\hat{U}(t, t_0) = \mathrm{e}^{-i\hat{K}(t)}\mathrm{e}^{-i(t-t_0)\hat{H}_{\mathrm{eff}}}\mathrm{e}^{i\hat{K}(t_0)}, \tag{1.9}$$

where $\hat{H}_{\mathrm{eff}}$ is the full time-independent effective Hamiltonian that describes slow motion and $\hat{K}(t)$ is the time-periodic kick-operator that describes micromotion [82, 83].

The effective Hamiltonian corresponding to a certain time-dependent Hamiltonian always exists, but in the general case it cannot be analytically calculated. However, there are several approximation schemes that allow computation of the leading terms of the effective Hamiltonian and the kick-operator. In cases where the driving frequency ω is large enough compared to the matrix elements of the Hamiltonian, two most often used approximations are the high-frequency expansion [82, 83, 90] and the Magnus expansion [91–93], which is in terms of the driving period $T = 2\pi/\omega$. The advantage of the former method over the latter is that the effective Hamiltonian does not depend on the initial driving phase. For this reason, we will only use the high-frequency expansion in this work. A general time-periodic modulating potential can be written in the form

$$\hat{V}(t) = \sum_{j=1}^{\infty}\left(\hat{V}^{(j)}\mathrm{e}^{ij\omega t} + \hat{V}^{(-j)}\mathrm{e}^{-ij\omega t}\right). \tag{1.10}$$

In the high-frequency expansion, the first few terms of the effective Hamilatonian corresponding

to the time-dependent Hamilatonian (1.6) are then [82]

$$\begin{aligned}\hat{H}_{\text{eff}} &= \hat{H}_0 + \frac{1}{\omega}\sum_{j=1}^{\infty}\frac{1}{j}\left[\hat{V}^{(j)},\hat{V}^{(-j)}\right] + \frac{1}{2\omega^2}\sum_{j=1}^{\infty}\frac{1}{j^2}\left(\left[\left[\hat{V}^{(j)},\hat{H}_0\right],\hat{V}^{(-j)}\right] + \text{H.c.}\right) \\ &+\frac{1}{3\omega^2}\sum_{j,l=1}^{\infty}\frac{1}{jl}\left(\left[\hat{V}^{(j)},\left[\hat{V}^{(l)},\hat{V}^{(-j-l)}\right]\right] - \left[\hat{V}^{(j)},\left[\hat{V}^{(-l)},\hat{V}^{(l-j)}\right]\right] + \text{H.c.}\right) \\ &+\mathcal{O}\left(\frac{1}{\omega^3}\right). \end{aligned} \tag{1.11}$$

This is a general equation that can be applied to a variety of different setups.

Floquet engineering provides a powerful tool for modern cold-atom experiments. However, the interactions between atoms can never be completely avoided and the combination of interactions and driving leads to unwanted heating. Thermalization to infinite temperature in the long-time and thermodynamic limit is practically unavoidable in such systems [94, 95]. Nevertheless, it might still be possible to find some parameter regime where thermalization is slow enough, for example if the system stays in the prethermalized state [96–98] on experimentally relevant timescales. This would allow experimental measurements in driven systems to be performed before full thermalization occurs.

1.6 This thesis

Throughout this thesis, we will use numerical simulations to study several interesting models which can be realized using ultracold bosonic atoms in optical lattices. In particular, we will be interested in systems which exhibit unusual nonergodic dynamics and systems with nontrivial topological properties. Both of these topics represent very active fields of research which have rapidly developed in recent years.

In Chapter 2 we will present a realization of quantum many-body scars in a bosonic model with density-dependent hopping. Since the first experimental observation in a Rydberg atom quantum simulator [46] and the subsequent theoretical explanation using the PXP model [47, 48], quantum many-body scars have been shown to exist in a variety of different systems [50–67]. However, most of the previous realizations have relied on the presence of "hard" kinetic constraints which restrict the available Hilbert space. For example, in the original PXP model this constraint arises from the fact that two neighbouring atoms cannot be simultaneously excited into Rydberg states due to an infinite energy penalty. Another question that was raised in the literature is proximity of quantum-scarred models to integrability, as adding certain perturbations to the PXP model can make it integrable. The main goal of Chapter 2 will be to show that quantum many-body scars can exist in manifestly nonintegrable systems with "soft" constraints only. To this end we will compare several similar models with different types of constraints. We will also formulate an analytically tractable approximation which

can explain and qualitatively predict revivals of quantum fidelity in the model which exhibits quantum many-body scars. An advantage of this model is that it could be easily realized in an optical lattice under a suitable Floquet scheme, thus providing a new experimental platform for quantum many-body scars. This would also allow future probes of this phenomenon to go beyond one-dimensional systems.

The main objective of the second part of this doctoral dissertation will be to study the interplay of topological features and interactions by investigating the dynamics of bosons in driven optical lattices. The approximations necessary for the computation of the effective Hamiltonian in a Floquet engineering scheme are mostly applied to noninteracting systems in the high-frequency limit, even though interactions usually cannot be realistically neglected and the interplay of driving and interactions can heat up the system to a featureless, infinite-temperature regime according to general considerations [94, 95]. One of the main open questions is whether it is possible to find some parameter regimes where the system is in the so-called prethermalized state [96–98] on intermediate timescales and can be described by some model of interest.

In Chapter 3 we will examine the effects of weak on-site interactions in relation to the recent Chern number measurement [70]. We take into account a realistic driving scheme and experimental parameters. Although the interactions are generally thought to complicate the experimental procedure, we will show that weak repulsive interactions can be beneficial for the measurement in at least two ways. Firstly, the interactions make the probability distribution in momentum space more homogeneous, which is important because the Chern number captures the contributions of Berry curvature from the whole Brillouin zone. Secondly and somewhat surprisingly, the interactions can cancel-out some unwanted higher-order therms which are a result of the driving protocol but are not related to the topological model of interest.

In Chapter 4 we will study a similar system as in Chapter 3, but now focusing on strong interactions. We will investigate the possibility of realizing a strongly correlated phase – fractional quantum Hall state – in driven systems on experimentally relevant timescales. Two main ingredients for the realization of fractional quantum Hall states, strong interactions and strong synthetic magnetic fields, are already available in present-day cold-atom experiments. However, even after years of experimental progress and numerous theoretical proposals, these states have still not been achieved, mainly due to problems related to heating caused by driving in the strongly interacting regime. Experimental realization of fractional quantum Hall states in cold-atom setups would be of particular interest due to their anyonic excitations, which could be of use for topological quantum computing [99]. Here we identify an optimal regime of microscopical parameters for the preparation of these highly sought-after states.

Finally, we will summarize all the results from this doctoral dissertation in Chapter 5. Additional derivations and technical details are provided in Appendices A-G.

Chapter 2

Quantum scars of bosons with correlated hopping

Semiclassical studies of chaotic stadium billiards have revealed the existence of remarkable non-chaotic eigenfuctions called "quantum scars" [49]. Scarred eigenfunctions display anomalous enhancement in regions of the billiard that are traversed by one of the periodic orbits in the classical limit when $\hbar \to 0$. It was shown that quantum scars lead to striking experimental signatures in a variety of systems, including microwave cavities [100], quantum dots [101], and semiconductor quantum wells [102].

A recent experiment on a quantum simulator [46], and subsequent theoretical work [47, 103], have shown that quantum many-body scars can occur in strongly interacting quantum systems. The experiment used a one-dimensional Rydberg atom platform in the regime of the Rydberg blockade [46, 104, 105], where nearest-neighbour excitations of the atoms were energetically prohibited. The experiment observed persistent many-body revivals of local observables after a "global quench" [106] from a certain initial state. In contrast, when the experiment was repeated for other initial configurations, drawn from the same type of "infinite" temperature ensemble, the system displayed fast equilibration and no revivals. These observations pointed to a different kind of out-of-equilibrium behavior compared to previous studies of quantum thermalization in various experimental platforms [23, 28, 36, 38, 107].

In both single-particle and many-body quantum scars, the dynamics from certain initial states leads to periodic revivals of the wave function. In the former case, this happens when the particle is prepared in a Gaussian wave packet initialized along a periodic orbit [49], while in the latter case the revivals can be interpreted as a nearly-free precession of a large emergent SU(2) spin degree of freedom [108, 109]. Another similarity between single- and many-body quantum scars is the existence of non-ergodic eigenstates. In the single-particle case, such eigenstates are easily identified by their non-uniform probability density that sharply concentrates along classical periodic orbits. In the many-body case, non-ergodic eigenstates are broadly

defined as those that violate Eigenstate Thermalization Hypothesis (ETH) [30, 31]. Scarred eigenstates violate the ETH in a number of ways: for example, they appear at evenly spaced energies throughout the spectrum [47, 48, 60], they have anomalous expectation values of local observables compared to other eigenstates at the same energy density, and their entanglement entropy obeys a sub-volume law scaling [48].

In recent works, the existence of atypical eigenstates has been taken as a more general definition of quantum many-body scaring. For example, highly-excited eigenstates with low entanglement have previously been analytically constructed in the non-integrable AKLT model [50, 51]. A few of such exact eigenstates are now also available for the Rydberg atom chain model [52]. The collection of models that feature atypical eigenstates is rapidly expanding, including perturbations of the Rydberg atom chain [48, 53, 54], theories with confinement [55, 56, 110], Fermi-Hubbard model beyond one dimension [57, 111], driven systems [58], quantum spin systems [59, 61], fractional quantum Hall effect in a one-dimensional limit [62], and models with fracton-like dynamics [63–65]. In a related development, it was proposed that atypical eigenstates of one Hamiltonian can be "embedded" into the spectrum of another, thermalizing Hamiltonian [112], causing a violation of a "strong" version of the ETH [33, 41]. This approach allows to engineer scarred eigenstates in models of topological phases in arbitrary dimensions [66]. From a dynamical point of view, it has been shown that models with scarred dynamics can be systematically constructed by embedding periodic on-site unitary dynamics into a many-body system [67].

A feature shared by many scarred models is the presence of some form of a kinetic constraint. In the Rydberg atom chain, the constraint results from strong van der Waals forces, which project out the neighboring Rydberg excitations [113]. Such Hilbert spaces occur, for example, in models describing anyon excitations in topological phases of matter [114–118] and in lattice gauge theories [119–121], including the Rydberg atom system [122, 123]. Recent works on periodically driven optical lattices have started to explore such physics [124, 125]. On the other hand, kinetic constraints have been investigated as a possible pathway to many-body localization without disorder [35]. In classical systems, non-thermalizing behavior without disorder is well-known in the context of structural glasses [126–128]. The mechanism of this type of behavior is the excluded volume interactions that impose kinetic constraints on the dynamics [129, 130]. Similar type of physics has recently been explored in quantum systems where a "quasi many-body localized" behavior was proposed to occur in the absence of disorder [131–141].

In this Chapter we investigate the relation between kinetic constraints, slow dynamics and quantum many-body scars. In contrast to previous work, which focused on models of spins and fermions that are closely related in one dimension due to the Jordan-Wigner mapping, here we study one-dimensional models of bosons with density-assisted hoppings, which realize both "hard" and "soft" kinetic constraints, whilst being non-integrable. In Section 2.1 we

introduce the models and discuss properties of their Hamiltonians when viewed as adjacency matrices of graphs in the Fock space. In Section 2.2 we investigate thermalization properties of these models by studying their energy level statistics, entanglement entropy of eigenstates, and dynamics under global quench. Depending on the form of the hopping term, we demonstrate that the models encompass a rich phenomenology, including regimes of fast thermalization, the existence of periodic revivals and many-body scars, as well as the Hilbert space fragmentation that has been found in recent studies of fractonic models [63–65]. Unlike the experimentally realized Rydberg atom system, we find evidence of many-body scars in a bosonic model without a hard kinetic constraint, i.e., with a fully connected Hilbert space. In Section 2.3 we identify initial states that give rise to periodic many-body revivals in the quantum dynamics, and we introduce a "cluster approximation" that captures the scarred eigenstates that are responsible for periodic revivals. In Section 2.4 we discuss zero-energy eigenstates of our models and their algebraic structure. Finally, in Section 2.5 we present our conclusions and discuss possible experimental realizations of these models using ultracold atoms.

2.1 Models and their Hilbert spaces

A fundamental ingredient of kinetically constrained models is "correlated hopping": a particle can hop depending on the state of its neighbors. In this Chapter we consider a system of N_p bosons on a one-dimensional lattice with L sites. We consider models where the total filling factor, $\nu = N_\mathrm{p}/L$, is conserved, and we will mainly present results in the dense regime, $\nu = 1$. We have studied models with $\nu < 1$ and $\nu > 1$, but we found them to be either too constrained or not constrained enough, and therefore less interesting. We emphasize that the bosons in our study are not hard-core, i.e., the occupancy of any lattice site can take any value from 0 to N_p.

2.1.1 Models

We study three different models, defined by the Hamiltonians:

$$\hat{H}_1 = -J\sum_{j=1}^{L}\left(\hat{b}_j^\dagger\hat{b}_{j+1}\hat{n}_j + \hat{n}_{j-1}\hat{b}_j^\dagger\hat{b}_{j-1}\right), \tag{2.1}$$

$$\hat{H}_2 = -J\sum_{j=1}^{L}\left(\hat{n}_j\hat{b}_j^\dagger\hat{b}_{j+1} + \hat{b}_j^\dagger\hat{b}_{j-1}\hat{n}_{j-1}\right), \tag{2.2}$$

$$\hat{H}_3 = -J\sum_{j=1}^{L}\left(\hat{n}_{j+1}\hat{b}_j^\dagger\hat{b}_{j+1}\hat{n}_j + \hat{n}_{j-1}\hat{b}_j^\dagger\hat{b}_{j-1}\hat{n}_j\right). \tag{2.3}$$

All three models contain a free-boson hopping term, $\hat{b}_j^\dagger\hat{b}_{j+1}$, which is dressed in various ways by density operators, $\hat{n}_j = \hat{b}_j^\dagger\hat{b}_j$. We will show that the position of the density operator $\hat{n}_j$ completely changes the behavior of these models, ranging from fast thermalization to the breakup

of the Hamiltonian into disconnected, exactly solvable sectors. For example, note that $\hat{H}_1$ and $\hat{H}_2$ are related to each other via free boson hopping,

$$\hat{H}_2 = \hat{H}_1 - J\sum_j \left(\hat{b}_j^\dagger \hat{b}_{j+1} + \hat{b}_j^\dagger \hat{b}_{j-1}\right), \tag{2.4}$$

which can be easily proven using bosonic commutation relations. We will see below that this innocuous free-boson hopping leads to surprisingly different dynamical properties of the two models.

The motivation behind introducing three different models in Eqs. (2.1)-(2.3) can be summarized as follows. Hamiltonian $\hat{H}_1$ describes a model where a particle cannot hop to the left if that site is not already occupied by at least one particle, and cannot hop to the right if it is the only particle left on its initial site. This introduces constraints to the system. Conversely, there are no such constraints in the case of $\hat{H}_2$. Indeed, the hopping coefficients are only modified in intensity by the particle-number operator. Hamiltonian $\hat{H}_3$ introduces additional constraints compared to $\hat{H}_1$. The number of unoccupied sites and their positions remain constant under the action of this Hamiltonian. This leads to different connectivity of the Hilbert space in each of the models, as we explain in the next Section.

We consider periodic boundary conditions ($L+1 \equiv 1$) and set $\hbar = J = 1$. With periodic boundary conditions, all three Hamiltonians $\hat{H}_1$, $\hat{H}_2$ and $\hat{H}_3$ have translation symmetry, thus their eigenstates can be labelled by momentum quantum number, k, quantized in units of $2\pi/L$. In addition, $\hat{H}_3$ has inversion symmetry. We denote by $I = 0$ and $I = 1$ the sectors that are even and odd under inversion, respectively.

Without restrictions on the boson occupancy, the Hilbert space of $\hat{H}_1$, $\hat{H}_2$ and $\hat{H}_3$ grows very rapidly. For $L = N_\mathrm{p} = 12$, the Hilbert space size of the $k = 0$ sector is 112720 (the largest one we will consider for $\hat{H}_1$ and $\hat{H}_2$). As previously mentioned (see also the next Section), the Hilbert space of $\hat{H}_3$ splits into many disconnected components, thus it is possible to consider only one connected component at a time and disregard the unoccupied sites whose positions do not change. This is more relevant when looking at properties such as thermalization, than fixing the filling factor. However, the boundary conditions are in that case no longer periodic, and the system does not have translation symmetry. Considering only a system with the size $L/2$, filling factor $\nu = 2$, open boundary conditions and minimal number of particles per site equal to 1 is completely equivalent to considering the largest component of the full system which has the size L, filling factor $\nu = 1$, periodic boundary conditions and no restrictions on the occupancies. The Hilbert space size of the symmetric invariant sector of the largest connected component of $L = N_\mathrm{p} = 22$ is 176484 and this is the largest sector that we will consider for $\hat{H}_3$.

2.1.2 Graph structure and bipartite lattice

Since we will be interested in the dynamical properties, it is convenient to first build some intuition about the structure of the Hamiltonians of the three models in Eqs. (2.1)-(2.3). A Hamiltonian can be viewed as the adjancency matrix of a graph whose vertices are Fock states of bosons, $|n_1, n_2, \ldots, n_L\rangle$. If the Hamiltonian induces a transition between two Fock states, the corresponding vertices of the graph are connected by a link. The graphs that show how the configuration space is connected have very different structure for the three Hamiltonians $\hat{H}_1$, $\hat{H}_2$ and $\hat{H}_3$, as can be observed in Fig. 2.1.

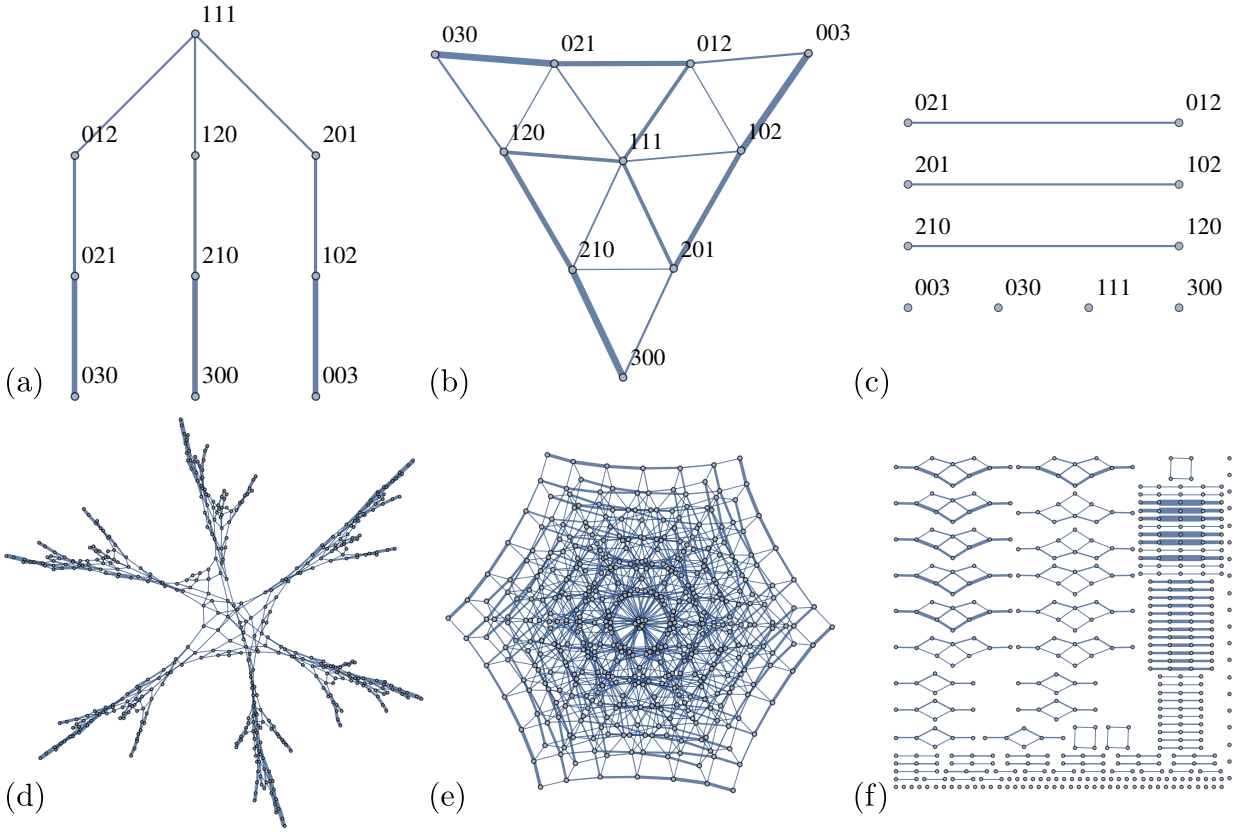

Figure 2.1: Connectivity of the Hilbert space. Adjacency graph for (a) $\hat{H}_1$, (b) $\hat{H}_2$, (c) $\hat{H}_3$, all for $L = N_\mathrm{p} = 3$. (d), (e) and (f): same as (a), (b) and (c) but for $L = N_\mathrm{p} = 6$. To avoid clutter, we do not label the vertices in (d), (e) and (f). All graphs are weighted, i.e., the line thickness is proportional to the magnitude of the corresponding hopping coefficient. Several different clusters of configurations are visible in the case of $\hat{H}_1$. The clusters start to form already for $L = 3$ (for example, the configurations 012–021–003 in (a)) and become more prominent for $L = 6$ (d). In the case of $\hat{H}_2$, almost all configurations are well-connected to the rest of the graph. The graphs for $\hat{H}_3$ show that the Hilbert space is highly reducible: its graph splits into many disconnected components.

The entire graph of $\hat{H}_2$ is well-connected and it has the same structure as the graph of the standard Bose-Hubbard model: the particle-number operators in $\hat{H}_2$ do not introduce any constraints, but only affect the magnitude of the hopping coefficients. In contrast, the $\hat{H}_1$ graph shows several clusters of configurations that are weakly connected to the rest of the

graph. "Weakly connected" means that there is a small number of connections leading outside the cluster and that their respective hopping coefficients are smaller in magnitude than those of the surrounding connections within the cluster. A state that is initially located inside a cluster is therefore more likely to stay inside during an initial stage of the time evolution, which increases the probability of revivals and slows down the growth of entanglement entropy. We will provide a more quantitative description and examples that illustrate this in Section 2.3. Finally, the graph of $\hat{H}_3$, due to even stronger constraints, is actually disconnected, which is an example of Hilbert space fragmentation that was previously shown to cause non-ergodic behavior in fracton-like models [64, 65]. This predicts that thermalization and dynamics in the three models will be very different, which we will confirm in the following Section. However, we note that the number of connections and the topology of the graph is not the only relevant factor for the dynamics. The magnitude of the hopping coefficients between different configurations is also important, see Appendix A.

We note that the relation between $\hat{H}_1$ and $\hat{H}_3$ is reminiscent of the relation between the quantum East model [142] and the "PXP" model describing the atoms in the Rydberg blockade regime [47, 48, 113]. Like $\hat{H}_3$, the PXP model is doubly constrained and inversion symmetric, while $\hat{H}_1$ and the quantum East model are asymmetric versions of those two models with only a single constraint. The graph of the quantum East model is similar to that of $\hat{H}_1$, in that it contains bottlenecks which slow down the growth of entanglement entropy [142].

The graph of $\hat{H}_1$ is bipartite, i.e. all the basis configurations can be divided into two disjoint sets, and the action of the Hamiltonian connects configurations in one set only to the configurations in the other and vice-versa (the Hamiltonian is off-diagonal). One way to sort configurations into these two sets is by parity of the quantity

$$\Delta_a = \frac{|n_{\text{even}} - n_{\text{odd}} + C|}{2}, \tag{2.5}$$

where $C = 0$ if L is even and $C = 1$ if L is odd. We define n_{even} and n_{odd} as the total numbers of particles at even and odd sites, respectively,

$$n_{\text{even}} = \sum_{l=1}^{L_1} n_{2l}, \;\; n_{\text{odd}} = \sum_{l=1}^{L_2} n_{2l-1}, \tag{2.6}$$

where $L_1 = L_2 = L/2$ if L is even, and $L_1 = (L-1)/2$, $L_2 = (L+1)/2$ if L is odd. If only nearest neighbor hoppings are allowed and if no two odd sites are coupled (if the system has open boundary conditions for any L or periodic boundary conditions for L-even), each hopping either increases n_{even} by one and decreases n_{odd} by one, or vice-versa. This means that each hopping can change Δ_a only by ± 1.

Another way to sort configurations into two sets is by parity of the distance from the

configuration $|111...111\rangle$, which we define as

$$d_a = \min_n\{\langle 111...111|\hat{H}_1^n|a\rangle \neq 0\}. \tag{2.7}$$

In this case, the two sets are the configurations with even and with odd distances d_a. One hopping can change d_a only by ± 1 or 0. Changes by other values are not possible by definition if the Hamiltonian is Hermitian (all hoppings are reversible). Both d_a and Δ_a have the same parity, thus d_a must always change after one hopping in even system sizes or in systems with open boundary conditions. As a consequence, d_a cannot change by 0 if Δ_a can only change by ± 1.

We have shown above that the $\hat{H}_1$ model is bipartite for open boundary conditions irrespective of the system size L parity or for periodic boundary conditions when L is even. Now we prove that this property of $\hat{H}_1$ holds true when L is odd and filling factor $\nu = 1$. Due to the constraints imposed by $\hat{H}_1$, a particle cannot hop to an empty site to its left. At the filling factor $\nu = 1$, all configurations except 111...111 contain at least one empty site. These configurations can be connected to 111...111 by hoppings only to the right, which is also the shortest possible path d_a, defined in Eq. (2.7). The empty sites can be filled only with particles that come from the site on their left, as hopping from the other side is forbidden. This implies that at least for one pair of adjacent sites (an empty site and the filled one on its right) there will be no particles hopping between them on the path to 111...111. We can then redefine the numbering of sites to start from the filled site in this pair. This is equivalent to setting the right (filled) site as the first and the left (empty) site as the last site in the chain and imposing open boundary conditions. In this way, no two odd sites will be coupled and the argument that the absolute difference between the numbers of particles on even and odd sites can only change by ± 1 will still be valid.

Unlike $\hat{H}_1$, $\hat{H}_2$ in the same geometry is not bipartite. The reason for this is that there are no constraints in the case of $\hat{H}_2$, so the shortest path to 111...111 can include hoppings both to the right and to the left, which means that it is not always possible to choose the numbering in such a way that no two odd sites are coupled. Because of the open boundary conditions, the Hamiltonian $\hat{H}_3$ in its largest connected component is also bipartite for all system sizes.

The graphs of bipartite systems do not contain any loops of odd dimension (triangles, pentagons, heptagons and so on). Moreover, the energy spectra of bipartite systems are symmetric around zero. Their Hamiltonians anticommute with the operator $(-1)^{\Delta_a}$. The presence of such an operator in a bipartite lattice leads to exact zero-energy states in the spectrum [143, 144]. It can be shown that the exponentially growing number of zero modes of $\hat{H}_1$ is related to the difference between the numbers of elements in the two sets of its bipartite graph, as explained in Section 2.4. Additionally, the algebraic structure of zero-energy eigenstates can be explained by the structure of the graph – such eigenstates can be constructed as superpositions of config-

urations from only one of the sets. Similar properties are found for $\hat{H}_2$ for even L, as its graph is also bipartite in that case. The properties of the zero-energy manifold are discussed in more detail in Section 2.4.

2.2 Dynamics and entanglement properties

We now investigate the phenomenology of the models introduced in Eqs. (2.1)-(2.3). We use exact diagonalization to obtain the complete set of energy eigenvalues and eigenvectors, from which we evaluate the level statistics and the distribution of entanglement entropies for the three models. Furthermore, we probe dynamical properties of the models by studying a global quench, simulated via Krylov iteration.

2.2.1 Level statistics and entanglement entropy

The energy level statistics is a standard test for thermalization of models that cannot be solved exactly. A convenient way to probe the level statistics is to examine the probability distribution $P(r)$ [145] of ratios between consecutive energy gaps $s_n = E_{n+1} - E_n$,

$$r = \frac{\min(s_n, s_{n+1})}{\max(s_n, s_{n+1})}. \tag{2.8}$$

The advantage of studying $P(r)$, instead of $P(s_n)$, is that there is no need to perform the spectrum unfolding procedure – see Ref. [94]. For standard random matrix theory ensembles, both $P(r)$ and the mean $\langle r \rangle$ are well-known [146]. When computing the same quantities in a microscopic physical model, it is crucial to resolve all the symmetries of the model.

The probability distribution $P(r)$ of the ratios of two consecutive energy gaps is shown in Figs. 2.2(a), (b) and (c) for the three Hamiltonians $\hat{H}_1$, $\hat{H}_2$ and $\hat{H}_3$ respectively, and two momentum or inversion sectors. In all three cases, the energy levels repel, i.e., the distribution tends to zero as $r \to 0$. For $\hat{H}_2$, the distribution is particularly close to the Wigner-Dyson (non-integrable) line. For $\hat{H}_1$, the distribution is also consistent with Wigner-Dyson when we restrict to the middle 1/3 of the spectrum (and after removing special states with $E = 0$). We exclude the edges of the spectrum because they contain degeneracies which are not symmetry-related. However, such states do not appear to have a major effect on the level statistics distribution, which is still closer to the Wigner-Dyson than the Poisson distribution even if they are included. The level statistics of $\hat{H}_3$ within the largest connected component of the Hilbert space is shown in Fig. 2.2(c) and is also consistent with the Wigner-Dyson distribution without restricting the spectrum. However, we will demonstrate below that the dynamics in some smaller connected components of $\hat{H}_3$ can be exactly solved.

As a complementary diagnostic of thermalization, we next compute the entanglement en-

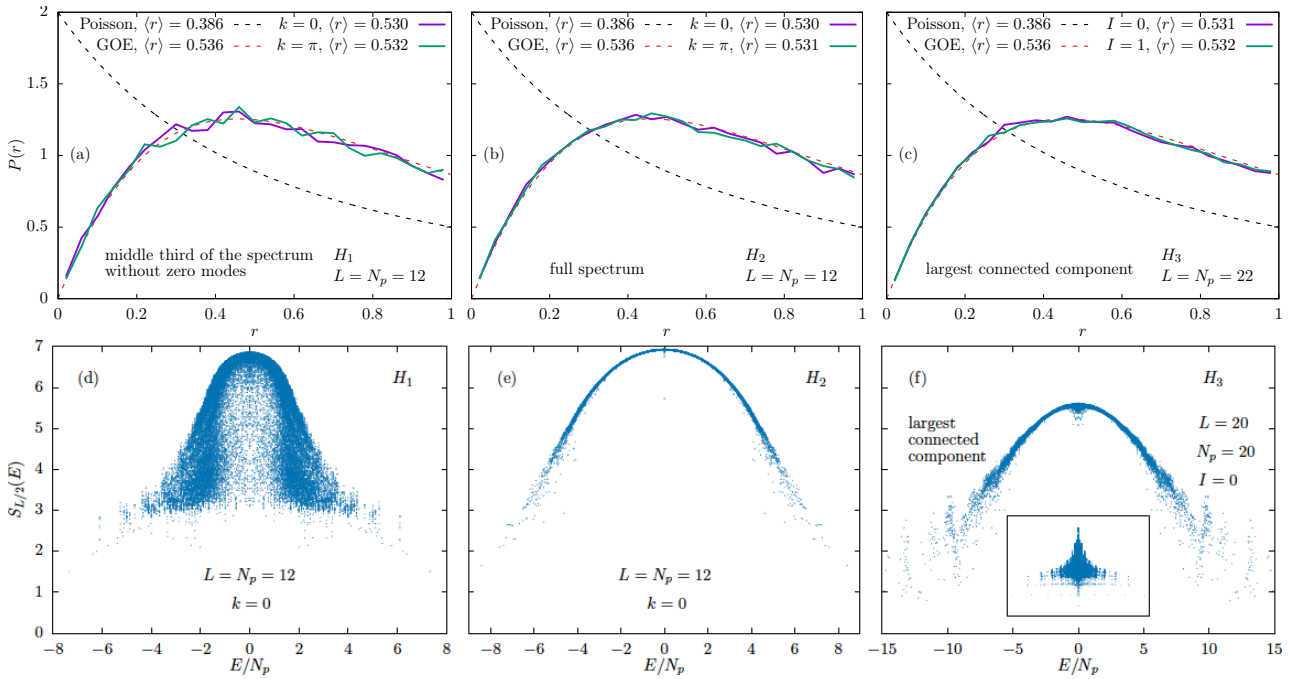

Figure 2.2: Level statistics and entanglement. (a), (b) and (c): Probability distribution of the ratios of two consecutive energy gaps. (a) $\hat{H}_1$ (middle third of the spectrum without $E = 0$ states, $L = N_\mathrm{p} = 12$), (b) $\hat{H}_2$ (full spectrum, $L = N_\mathrm{p} = 12$) and (c) $\hat{H}_3$ (largest connected component of $L = N_\mathrm{p} = 22$). The black dashed line shows the Poisson distribution, which corresponds to the integrable case, while the red dashed line is the distribution of the Gaussian orthogonal ensemble, which corresponds to the thermalizing case. (d), (e) and (f): Entanglement entropies $S_{L/2}$ of all eigenstates plotted as a function of the eigenstate energy per particle, E/N_p. (d) $\hat{H}_1$ ($L = N_\mathrm{p} = 12$, $L_\mathrm{A} = 6$, $k = 0$), (e) $\hat{H}_2$ (same) and (f) $\hat{H}_3$ in the largest connected component of $L = N_\mathrm{p} = 20$, $L_\mathrm{A} = 10$, $I = 0$. The inset shows all connected components for $L = N_\mathrm{p} = 12$, $L_\mathrm{A} = 6$, $k = 0$.

tropy of all eigenstates. We divide the lattice into two sublattices, A and B, of lengths L_A and $L_\mathrm{B} = L - L_\mathrm{A}$. For a given pure state $|\psi\rangle$, the entanglement entropy is defined as

$$S_\mathrm{A} = -\mathrm{Tr}_\mathrm{A}(\rho_\mathrm{A} \ln \rho_\mathrm{A}), \tag{2.9}$$

where $\rho_\mathrm{A} = \mathrm{Tr}_\mathrm{B}|\psi\rangle\langle\psi|$ is the reduced density matrix of the subsystem A. The scatter plots, showing entanglement entropy of all eigenstates $|E_n\rangle$ as a function of their energy E_n, are displayed in Figs. 2.2(d), (e) and (f). Here we take into account the translation symmetry of the system and work in the momentum sector $k = 0$ for $\hat{H}_1$ and $\hat{H}_2$, and consider only the largest connected component and the inversion sector $I = 0$ for $\hat{H}_3$. The results for other sectors are qualitatively similar.

Entanglement entropy distribution in Figs. 2.2(d) and (e) reveals a striking difference between the Hamiltonians $\hat{H}_1$ and $\hat{H}_2$, even though they only differ by a free-boson hopping term, Eq. (2.4). The model $\hat{H}_1$ is constrained, which leads to a large spread of the entropy distribution and many low-entropy eigenstates including in the bulk of the spectrum. From this perspective, $\hat{H}_1$ is reminiscent of PXP model [48, 53]. By contrast, $\hat{H}_2$ has no such constraints

and in this case the entanglement entropy is approximately a smooth function of the eigenstate energy. The Hamiltonian $\hat{H}_3$ is doubly constrained, and this is reflected in its entanglement distribution, which also shows a large spread and several disconnected bands, reminiscent of an integrable system like the XY model [147].

2.2.2 Global quenches

The constraints in the models in Eqs. (2.1), (2.2) and (2.3) have significant effects on the dynamics governed by these Hamiltonians. We probe the dynamics by performing a global quench on the system. We assume the system is isolated and prepared in one of the Fock states, $|\psi_0\rangle$, at time $t = 0$. We restrict to $|\psi_0\rangle$ being product states which are not necessarily translation-invariant, as such states are easier to prepare in experiment. However, our results remain qualitatively the same if we consider translation-invariant $|\psi_0\rangle$. After preparing the system in the state $|\psi_0\rangle$, which is not an eigenstate of the Hamiltonian, the system is let to evolve under unitary dynamics,

$$|\psi(t)\rangle = \exp\left(-\frac{i}{\hbar}\hat{H}t\right)|\psi_0\rangle. \tag{2.10}$$

where $\hat{H}$ is one of the Hamiltonians of interest. From the time-evolved state, we evaluate the quantum fidelity,

$$F(t) = |\langle\psi_0|\psi(t)\rangle|^2, \tag{2.11}$$

i.e., the probability for the wave function to return to the initial state. In a general many-body system, fidelity is expected to decay as $F(t) \sim \exp(-L(Jt)^2)$. It thus becomes exponentially suppressed in the system size for any fixed time t^*, i.e., $F(t^*) \sim \exp(-cL)$, where c is a constant. In scarred models, such as the Rydberg atom chain, fidelity at the first revival peak occurring at a time T still decays exponentially, but exponentially slower, i.e., $F(T) \sim \exp(-c'L)$, with $c' \ll c$. In Ref. [48], for a finite system with $L \lesssim 32$ atoms, the fidelity at the first revival can be as high as $\sim 70\%$, and several additional peaks at times nT are also clearly visible.

We first consider the Hamiltonian $\hat{H}_1$. Several configurations exhibit periodic revivals of the fidelity $F(t)$, which can in some cases be higher than 90%. Most of these configurations involve a very dense cluster of bosons such as $|...0N10...\rangle$. In contrast, a completely uniform configuration $|...111...\rangle$ thermalizes very quickly. Here we focus on periodically-reviving configurations with density being as uniform as possible. One family of such reviving configurations involves n unit cells made of 3 lattice sites:

$$|210210\ldots210\rangle \equiv |(210)^n\rangle. \tag{2.12}$$

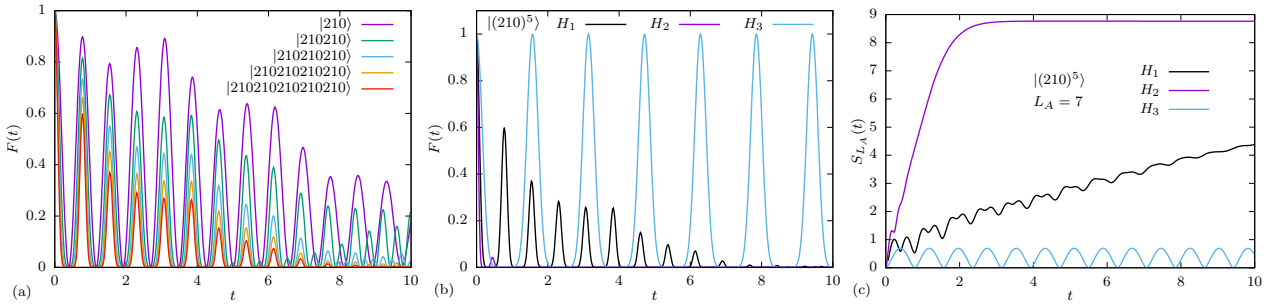

Figure 2.3: Dynamics of quantum fidelity and entanglement entropy for initial configurations in Eq. (2.12). (a) Time evolution of fidelity $F(t)$ in Eq. (2.11) for system sizes $L = 3n$. The evolution is governed by the Hamiltonian $\hat{H}_1$, different colors represent different system sizes L. (b) Fidelity evolution $F(t)$ for the Hamiltonians $\hat{H}_1$, $\hat{H}_2$ and $\hat{H}_3$ and system size $L = 15$. (c) Entanglement entropy evolution $S_{L_A}(t)$ for the same cases as in (b).

Time evolution of the fidelity for the initial state $|(210)^n\rangle$ for different system sizes $L = 3n$ is shown in Fig. 2.3(a). The initial state is assumed to be the product state, e.g., $|\psi_0\rangle = |210\rangle$ for $L = 3$. The frequency of the revivals in Fig. 2.3 is approximately the same for all system sizes. We emphasize that similar results are obtained for a translation-symmetric initial state, e.g., $|\psi_0\rangle = \frac{1}{\sqrt{3}}(|210\rangle + |021\rangle + |102\rangle)$. Both cases converge in the large system limit, and the differences are only significant for $L = 3$ when the revival frequency of the initial state with transition symmetry differs from the frequencies of other system sizes.

In Fig. 2.3(b) we compare the fidelity for the initial state in Eq. (2.12) when it is evolved by all three Hamiltonians in Eqs. (2.1)-(2.3). The initial state is fixed to be $|(210)^5\rangle$. We observe that the dynamics with $\hat{H}_3$ has very prominent revivals; in fact as we will later show, these revivals are perfect and their period is approximately twice the revival period for $\hat{H}_1$. In contrast, for $\hat{H}_2$ the fidelity quickly drops to zero without any subsequent revivals.

Finally, in Fig. 2.3(c) we plot the time evolution of entanglement entropy. As expected from the fast decay of the fidelity, the entropy for $\hat{H}_2$ rapidly saturates to its maximal value. Moreover, as expected from the perfect revivals in $\hat{H}_3$, the entropy in that case oscillates around a constant value close to zero. For $\hat{H}_1$, we observe a relatively slow growth of entropy, with oscillations superposed on top of that growth, again similar to PXP model [47]. For the initial state that is not translation-invariant, it is important how we cut the system, e.g., $|...210|210...\rangle$ versus $|...2102|10...\rangle$. In the first case, the entanglement entropy remains zero for $\hat{H}_3$ because no particle can hop from one subsystem to the other, while in the second case the entropy oscillates around a constant value, which is the case in Fig. 2.3(c).

In Fig. 2.4 we show the $\hat{H}_1$ evolution of two local observables, density correlations between two adjacent sites $\langle \hat{n}_1 \hat{n}_2(t) \rangle$ and density on the first site $\langle \hat{n}_1(t) \rangle$, starting from the initial state $|(210)^n\rangle$. Unlike fidelity and entanglement entropy, these observables can be easily measured in experiment. Both observables robustly oscillate with approximately the same frequency as the fidelity. The heights of the first few revival peaks are approximately converged for the system

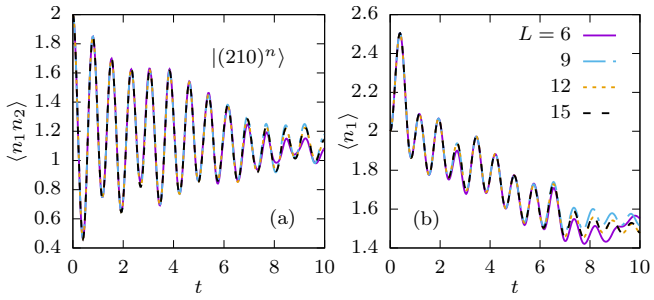

Figure 2.4: Evolution of local observables for the Hamiltonian $\hat{H}_1$. (a) Correlations between adjacent sites $\langle \hat{n}_1 \hat{n}_2(t) \rangle$ for different system sizes and the initial state $|(210)^n\rangle$. (b) Density on one site $\langle \hat{n}_1(t) \rangle$.

sizes ranging from $L = 6$ to $L = 15$, which suggests that revivals in such local observables can be observed in the thermodynamic limit. In the following Section, we will show that the oscillations observed in the dynamics from $|(210)^n\rangle$ state in Eq. (2.12) and their frequency can be explained using a tractable model that involves only a small subset of all configurations in the Hilbert space, thus providing a realization of quantum scars in a correlated bosonic system. Our starting point will be the model $\hat{H}_3$, whose graph explicitly separates into disconnected subsets which makes the toy model exact, hence we can analytically calculate the revival frequency. Based on these results, we then introduce an approximation scheme that describes the dynamics from the same initial state under the $\hat{H}_1$ Hamiltonian.

2.3 Quantum scars in $\hat{H}_1$ and $\hat{H}_3$ models

The quench dynamics of fidelity and entanglement entropy in Fig. 2.3 suggest that $\hat{H}_1$ and $\hat{H}_3$ models are candidate hosts for many-body scarred eigenstates that can be probed by initializing the system in product states $|(210)^n\rangle$. We now analyze the structure of these states using our approach called "cluster approximation".

2.3.1 Perfect revivals in the $\hat{H}_3$ model

The dynamics of $\hat{H}_3$ within the sector containing the state $|(210)^n\rangle$ can be solved exactly. We start with a warmup calculation for $\hat{H}_3$ acting on $L = 3$ sites. The connected subspace of 210 contains only two configurations, 120 and 210. The Hamiltonian reduced to this subspace is

$$\hat{H}_3' = -\begin{pmatrix} 0 & 2 \\ 2 & 0 \end{pmatrix}, \tag{2.13}$$

where the basis vectors are

$$\begin{pmatrix} 1 \\ 0 \end{pmatrix} = |210\rangle, \quad \begin{pmatrix} 0 \\ 1 \end{pmatrix} = |120\rangle. \tag{2.14}$$

The eigenvalues of $\hat{H}_3^{'}$ are $E_1 = -2$ and $E_2 = 2$. The initial state $|\psi_1(t=0)\rangle = |210\rangle$ evolves as

$$|\psi_1(t)\rangle = \cos(2t)|210\rangle - i\sin(2t)|120\rangle, \tag{2.15}$$

and the state $|\psi_2(t=0)\rangle = |120\rangle$ evolves as

$$|\psi_2(t)\rangle = -i\sin(2t)|210\rangle + \cos(2t)|120\rangle. \tag{2.16}$$

Previous results can be straightforwardly generalized to larger systems. Let the length of the system be $L = 3n$ for simplicity. The connected component of the state $|(210)^n\rangle$ consists only of combinations of patterns 210 and 120, which means that triplets of sites evolve independently, and dynamically the system behaves as a collection of independent two level systems (spins-1/2). From Eq. (2.15), the initial state $|\psi_n(t=0)\rangle = |(210)^n\rangle$ evolves as

$$|\psi_{L=3n}(t)\rangle = \cos^n(2t)|(210)^n\rangle + (-i)^n\sin^n(2t)|(120)^n\rangle + ... \tag{2.17}$$

where "..." denotes contributions of the basis configurations other than $|(210)^n\rangle$ or $|(120)^n\rangle$. The fidelity is

$$F_{L=3n}(t) = |\langle\psi_n(0)|\psi_n(t)\rangle|^2 = |\cos 2t|^{2n}. \tag{2.18}$$

It follows that the revivals are perfect, with a period $T_3 = \pi/2$. This result is also valid for the translation-invariant initial state $|(210)^n\rangle_{\mathrm{T}}$,

$$|(210)^n\rangle_{\mathrm{T}} \equiv \frac{1}{\sqrt{3}}\left(|(210)^n\rangle + |(021)^n\rangle + |(102)^n\rangle\right), \tag{2.19}$$

as the connected subspaces of 210, 021 and 102 do not overlap and therefore evolve independently.

However, an initial state that is both translation symmetric and inversion symmetric has different dynamics. The inverse of the configuration $|(210)^n\rangle$ is the configuration $|(012)^n\rangle$, which is a translation of the state $|(120)^n\rangle$ that belongs to the connected subspace of $|(210)^n\rangle$. The initial state

$$|\psi_n^{\mathrm{inv}}(t=0)\rangle = \frac{1}{\sqrt{2}}|(210)^n\rangle_{\mathrm{T}} + \frac{1}{\sqrt{2}}|(120)^n\rangle_{\mathrm{T}} \tag{2.20}$$

evolves as

$$|\psi_n^{\mathrm{inv}}(t)\rangle = \left(\cos^n 2t + (-i)^n\sin^n 2t\right)|\psi_n^{\mathrm{inv}}(t=0)\rangle + ... \tag{2.21}$$

and the fidelity is

$$F_n^{\text{inv}}(t) = |\langle\psi_n^{\text{inv}}(0)|\psi_n^{\text{inv}}(t)\rangle|^2 = |\cos^n 2t + (-i)^n \sin^n 2t|^2. \tag{2.22}$$

The frequency of the revivals is now doubled, so the period is $T_3^{\text{inv}} = \pi/4$.

2.3.2 Cluster approximations for the $\hat{H}_1$ model

In contrast to the free dynamics in $\hat{H}_3$, the $\hat{H}_1$ model exhibits decaying revivals and does not admit an exact description. In order to approximate the quench dynamics and scarred eigenstates in $\hat{H}_1$, we project the Hamiltonian to smaller subspaces of the full Hilbert space. These subspaces contain clusters of states which are poorly connected to the rest of the Hilbert space and thereby cause dynamical bottlenecks. The clusters can be progressively expanded to yield an increasingly accurate description of the dynamics from a given initial state.

Here we introduce a scheme for approximating the dynamics from initial states $(210)^n$ in the $\hat{H}_1$ model. As can be observed in Fig. 2.3, the revival periods are approximately the same for different system sizes. We first focus on the non-trivial case $L = 6$. Fig. 2.5 shows part of the graph that contains the initial state, $|210210\rangle$. Configurations labelled inside the ellipses denote representatives of an orbit of translation symmetry, i.e., the configurations are translation-invariant such as the one in Eq. (2.19).

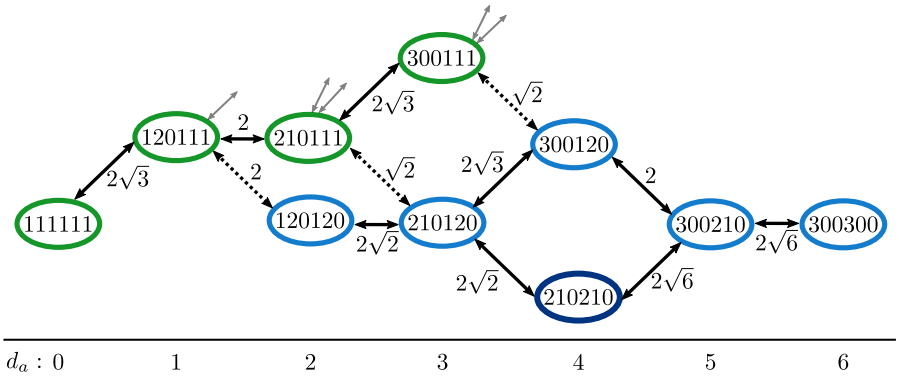

Figure 2.5: Minimal and extended clusters. Hamiltonian $\hat{H}_1$ and system size $L = N_{\text{p}} = 6$. Configurations labelled inside the ellipses are representatives of an orbit of translation symmetry. The minimal cluster is defined by the blue configurations, while green configurations represent the additional components of the extended cluster. Grey arrows connect to configurations outside the extended cluster. The numbers bellow the graph show the distance d_a from the configuration 111111 evaluated using Eq. (2.7).

The minimal subcluster of the graph is highlighted in blue color in Fig. 2.5. This cluster is indeed weakly connected to the rest of the configuration space, as it has only 3 connections that lead outside this cluster (dashed lines) and their hopping coefficients are slightly lower in magnitude than those inside the cluster, meaning that the probability is higher to stay inside the cluster than to leave. The hopping coefficients leading outside are not significantly smaller

than the coefficients staying inside, but in combination with the relatively small number of connections this has significant effects on the dynamics. This effect is even more pronounced when the difference in magnitudes is further increased by squaring the particle number operators, as shown in Appendix A.

The minimal cluster from Fig. 2.5 contains all the states given by tensor products of 210, 120 and 300 configurations. The set of configurations belonging to this cluster could have been chosen differently, but this particular choice has at least two advantages. Firstly, inside this cluster, the evolution of the configuration $|210210\rangle$ can be thought of as two subsystems 210 evolving separately. The evolution of all such configurations at different system sizes can be reduced to the evolution of $L = 3$ subsystems 210, similar to the case of $\hat{H}_3$ in the connected subspace of $(210)^n$. Secondly, this definition allows easy generalization to different system sizes $L = 3n$ with initial states $(210)^n$. The dimension of the reduced Hilbert space grows with the system size as $\dim\mathcal{H}^{\mathrm{c}} = 3^n$. We would like to emphasize that the cluster was not chosen arbitrarily. The calculations of the probability density distribution starting from the initial configuration $|210210\rangle$ and evolving with $\hat{H}_1$ have shown that the probability density stays high in this region of the Hilbert space as long as the revivals in fidelity are visible. The configurations important for the dynamics were then identified by analyzing the structure of the graph around the initial configuration.

As an example, consider system size $L = 3$. The reduced Hilbert space of the cluster $\mathcal{H}^{\mathrm{c}}$ is spanned by the (non-translation-invariant) configurations

$$\begin{pmatrix}1\\0\\0\end{pmatrix} = |300\rangle, \quad \begin{pmatrix}0\\1\\0\end{pmatrix} = |210\rangle, \quad \begin{pmatrix}0\\0\\1\end{pmatrix} = |120\rangle. \tag{2.23}$$

The Hamiltonian reduced to this subspace is

$$\hat{H}_1^{\mathrm{c}} = -\begin{pmatrix}0 & 2\sqrt{3} & 0\\ 2\sqrt{3} & 0 & 2\\ 0 & 2 & 0\end{pmatrix}, \tag{2.24}$$

and its eigenvalues are $E_1 = -4$, $E_2 = 4$, $E_3 = 0$. The initial configuration $|210\rangle$ evolves according to

$$|\psi_1^{\mathrm{c}}(t)\rangle = -\frac{i}{2}\sin(4t)\left(\sqrt{3}|300\rangle + |120\rangle\right) + \cos(4t)|210\rangle. \tag{2.25}$$

By generalizing this result to larger systems, it is easy to prove that the time-evolved state

within the cluster is given by

$$|\psi_n^c(t)\rangle = \cos^n(4t)|(210)^n\rangle + \ldots, \tag{2.26}$$

where the dots denote other configurations, and the fidelity is

$$F_n^c(t) = |\langle\psi_n^c(0)|\psi_n^c(t)\rangle|^2 = |\cos(4t)|^{2n}. \tag{2.27}$$

As in the case of $\hat{H}_3$, this result is also valid for the translation-invariant initial state. We see that the period of revivals is $T_1 = \pi/4$, which is the same as for $\hat{H}_3$ with a translation and inversion symmetric initial state.

The minimal clusters can be expanded by adding several neighboring configurations. For similar reasons as in the case of minimal clusters, the extended clusters are defined as sets of all states which can be obtained using tensor products of the configurations 210, 120, 300 and 111. In the case of $L = 6$, the enlarged cluster can be observed in Fig. 2.5. It contains the minimal cluster studied previously, but it also includes additional configurations shown in green ellipses. Again, the approximation could be improved by including more configurations, but this particular choice is well suited for analytical treatment (see Appendix B) and, as shown above, it gives a good prediction for the first revival peak height.

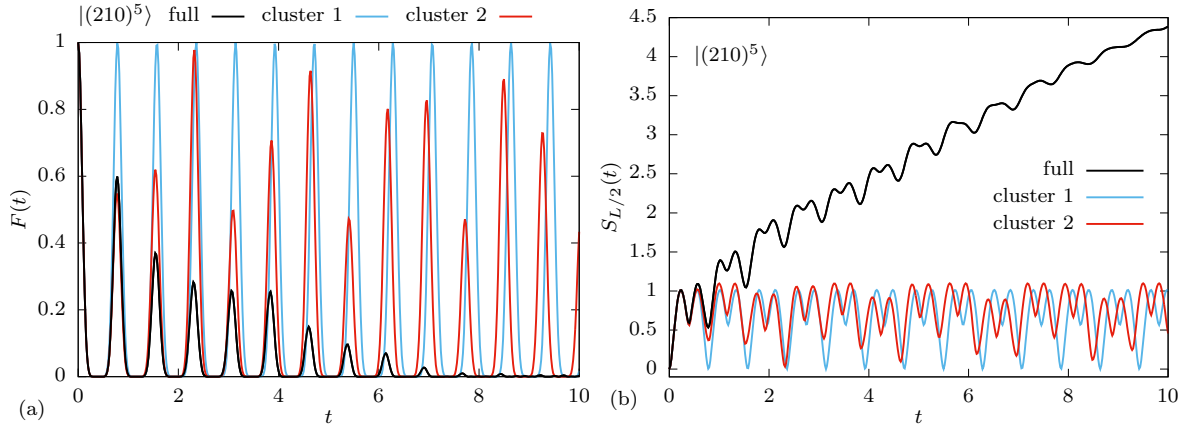

Figure 2.6: Comparison of the full dynamics against the minimal cluster (1) and extended cluster (2) approximation schemes. We consider the system size $L = 15$ with the initial state $|(210)^5\rangle$. (a) Time evolution of the fidelity. The frequency of revivals is approximately the same in both cases, but the results for the extended cluster show better agreement with the results for the full Hilbert space. (b) Time evolution of the entanglement entropy.

The result of the cluster approximation is compared against the exact result for system size $L = 15$ in Fig. 2.6. The frequency of the fidelity revival, shown by the blue line in Fig. 2.6(a), is accurately reproduced in this approximation, however the approximation does not capture the reduction in the magnitude of $F(t)$. Similarly, the dynamics of entanglement entropy, blue line in Fig. 2.6(b), is only captured at very short times. In particular, we observe that the maximum entanglement within the cluster remains bounded even at long times $t \sim 10$, while

the exact entropy continues to increase and reaches values that are several times larger.

To obtain a more accurate approximation, we can expand the minimal cluster with several neighboring configurations on the graph. We define the extended cluster as a set of all states which can be obtained using tensor products of the configurations 210, 120, 300 and 111. The enlarged cluster clearly contains the minimal cluster studied above, but it also includes additional configurations, resulting in a much better prediction for the first revival peak height, while still allowing for analytical treatment. The dimension of the extended cluster grows as $\dim\mathcal{H}^{\tilde{c}} = 4^{L/3}$, and is thus exponentially larger than the minimal cluster approximation. Nevertheless, the extended cluster dimension is still exponentially smaller compared to the full Hilbert space, and within this approximation it is possible to numerically simulate the dynamics of larger systems, $L \lesssim 30$ – see Fig. 2.7(a). The revivals are no longer perfect, while their frequency is independent of the system size and closer to the frequency of revivals for the full Hilbert space compared to to the minimal cluster approximation in Fig. 2.6. The overlap between the eigenstates of the Hamiltonian $\hat{H}_1$ reduced to both the minimal and extended cluster and the state $|(210)^8\rangle$ is given in Fig. 2.7(b). The eigenstates that correspond to the minimal cluster approximately survive in the extended cluster, where they form a band with the highest overlap.

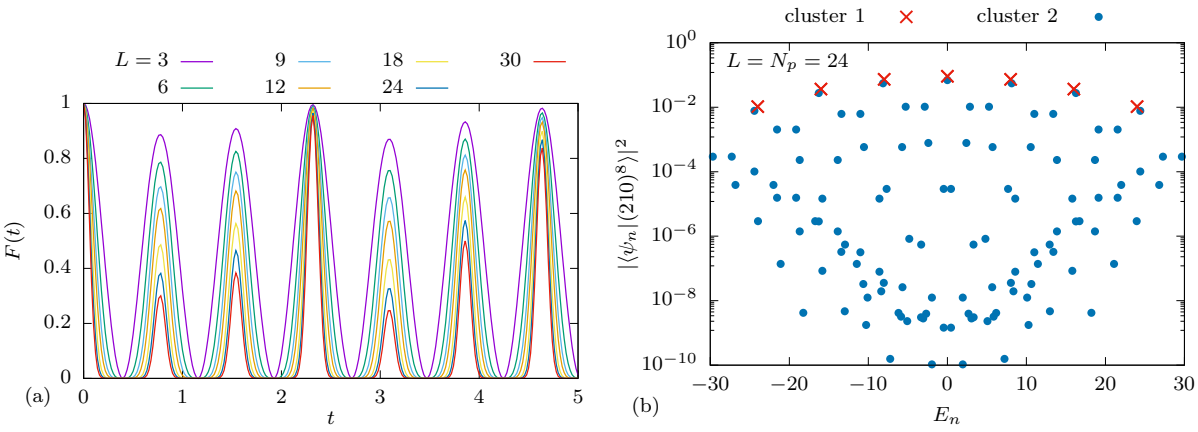

Figure 2.7: Cluster approximations. (a) Fidelity $F(t)$, for the Hamiltonian $\hat{H}_1$ and initial states $|(210)^n\rangle$, in the extended cluster approximation for various system sizes. (b) Eigenstate overlap with the initial state $|(210)^8\rangle$ plotted on a log scale, for both cluster approximations. In the case of degenerate eigenstates the sum of their overlaps is shown.

For the initial product state $(210)^n$, it is possible to analytically obtain the fidelity within the improved approximation for arbitrary system size. Similar to the previous methods, it can be shown (see Appendix B)

$$F^{\tilde{c}}_{L=3n}(t) \quad = \quad 4^n|b^2\cos(\alpha t) + d^2\cos(\beta t)|^{2n}, \tag{2.28}$$

where $\alpha = \sqrt{9+\sqrt{57}} \approx 4.06815$, $\beta = \sqrt{9-\sqrt{57}} \approx 1.20423$, $b \approx 0.694113$ and $d \approx 0.134933$. Eq. (2.28) is in excellent agreement with the numerical results in Fig. 2.7(a). It was also found

to be a very good approximation for the translation-invariant initial state when $L \geq 9$ (data not shown).

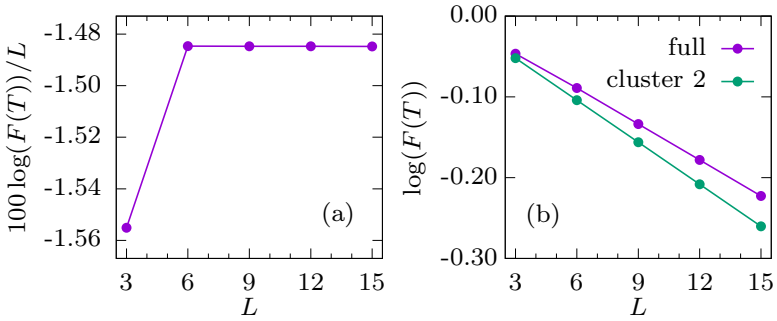

Figure 2.8: First peak height. (a) Logarithm (base 10) of the first revival peak divided by the system size, $\log(F(T))/L$, seems to saturate at a finite value in the thermodynamic limit. (b) Comparison of the logarithm of the first revival peak height for the full dynamics and the improved cluster approximation. The approximation serves as a lower bound.

Fig. 2.8(a) shows that the logarithm of the fidelity per site, $\log(F(T))/L$, at the first peak, saturates at a finite value for large L. In the improved cluster approximation, the first peak height decays as $\mathrm{e}^{-0.04L}$, as shown in Appendix B. For a completely random state, the fidelity would be $F \sim 1/\dim\mathcal{H}$. In the case $\nu = 1$ and large L, the Hilbert space dimension grows with the system size as

$$\dim\mathcal{H} = \binom{2L-1}{L} \approx \binom{2L}{L} \approx \frac{4^L}{\sqrt{\pi L}}. \tag{2.29}$$

This back-of-the-envelope estimate suggests the fidelity of a random state is $F \sim \mathrm{e}^{-1.39L}$, which decays considerably faster than the first peak height in Fig. 2.8. The improved cluster approximation correctly reproduces the short-time dynamics, including the first revival peak, and sets a lower bound for the first peak height – see Figs. 2.6 and 2.8(b).

The evolution of the entanglement entropy for the extended cluster approximation is shown in Fig. 2.6(b). Inside the cluster, entropy remains approximately constant with periodic oscillations that have the same frequency as the wave function revivals. Any further growth of the entanglement entropy can be attributed to the spreading of the wave-function outside the cluster. To illustrate the "leakage" of the wave function outside the cluster, in Fig. 2.9 we compute the time evolution of the overlap with a cluster, i.e., the probability to remain inside a cluster at time t,

$$\mathcal{O}_{\text{Cluster}} = \sum_{a \in \text{Cluster}} |\langle a|\psi(t)\rangle|^2. \tag{2.30}$$

We consider several initial configurations that lie inside or outside the cluster. The configurations initially inside the cluster mostly stay there, and the configuration $|(210)^4\rangle$ that has the highest revivals also has the highest overlap. Similarly, configurations initially outside the cluster continue to have negligible overlaps. The overlap starting from the configuration $|(210)^4\rangle$

approximately predicts the revival peak heights for the full dynamics.

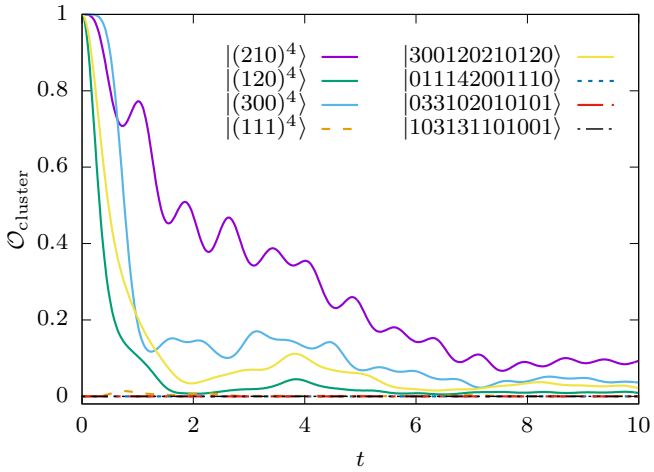

Figure 2.9: Evolution of the probability to remain inside the minimal cluster. $\mathcal{O}_{\text{Cluster}}$, as defined in Eq. (2.30). Initial configurations are indicated in the legend. Solid lines: configurations initially inside the cluster. Dashed lines: configurations initially outside the cluster (all except $|(111)^4\rangle$ are randomly chosen). Similar results are obtained for the extended cluster (not shown). System size $L = 12$.

We now summarize the relation between $\hat{H}_3$ and $\hat{H}_1$ from the point of view of the cluster approximation. For the initial state $|(210)^n\rangle$, the two models yield similar dynamics, compare Eqs. (2.18) and Eq. (2.28). The only difference is that the revival frequency is doubled in the latter case, which can be easily explained by the symmetry of the initial state and that of the Hamiltonian. Hamiltonian $\hat{H}_3$ is inversion-symmetric. If the initial state is also chosen to be inversion-symmetric, the frequency of the revivals doubles. The period is then $T_3^{\text{inv}} = \pi/4$, which is equal to the period of revivals T_1 of $\hat{H}_1$ in the cluster approximation. This was proven analytically in Section 2.3.1, see Eq. (2.22). For comparison, the revival period for the full Hilbert space is approximately 0.77, which is slightly less than $\pi/4 \approx 0.79$. The Hamiltonian $\hat{H}_1$ is not inversion-symmetric, so the frequency does not double for an inversion-symmetric initial state, but the revivals are lower in that case. This shows that it is important for the symmetry of the initial state to match the symmetry of the Hamiltonian.

Finally, the eigenstates of $\hat{H}_1$, projected to the subspace of the minimal cluster approximation, form several degenerate bands whose eigenenergies are equally spaced in integer multiples of 4. Interestingly, some of these eigenstates approximately survive in the full $\hat{H}_1$ model, and they are precisely the eigenstates that have the highest overlap with the configurations $|(210)^n\rangle$, see Fig. 2.10(a). In small system sizes, such as $L = 6$, the surviving eigenstates are also the lowest entropy eigenstates in the middle of the spectrum, which is reminiscent of quantum scars in the PXP model [48]. In larger systems, e.g., $L = 12$, the surviving eigenstates are slightly lower in entropy than their neighbors, but are far from being the lowest entropy eigenstates, as can be seen in Fig. 2.10. The lowest entropy eigenstates have high overlaps with other configurations, such as $|(3100)^3\rangle$, as shown in Figs. 2.10(b) and 2.10(c). In the case of $|(210)^n\rangle$, the

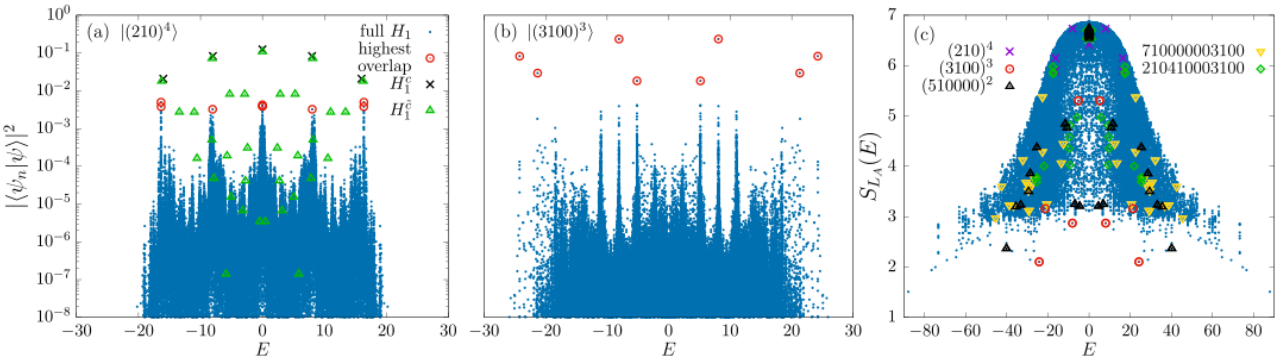

Figure 2.10: Non-ergodic eigenstates. (a) Overlap of the configuration $|(210)^4\rangle$ with all the eigenstates of $\hat{H}_1$, $\hat{H}_1^c$ and $\hat{H}_1^{\bar{c}}$ versus the eigenstate energy for sector $k = 0$ and system size $L = N_p = 12$. (b) Same for $|(3100)^3\rangle$. (c) Entanglement entropy, eigenstates which have the highest overlap with some product states are marked in different colors.

eigenstates surviving in the full system belong to every other band of eigenstates in the cluster approximation and the number of the surviving eigenstates is $n + 1$. For even system sizes this counting includes a zero-energy eigenstate. In Section 2.3.3 we discuss in more details the generalization of the cluster approximations to the states of the form $|(N10...0)^n\rangle$, which were also found to have robust revivals and high overlaps with some low-entropy eigenstates.

2.3.3 Generalization to other clusters

Building on the previous observation that some of the low-entropy eigenstates have large weight on $|(3100)^3\rangle$ product state, we have investigated periodic revivals from such a larger class of initial states. We find that robust revivals are associated with initial product states of the form

$$|((N-1)1\underbrace{0...0}_{N-2})^n\rangle, \tag{2.31}$$

where N is the length of the unit cell ($L = Nn$). For example, some of these configurations are $|(3100)^n\rangle$, $|(41000)^n\rangle$ and $|(510000)^n\rangle$. Combinations of those patterns such as $|310041000\rangle$ also exhibit similar properties, but we will restrict ourselves to the simpler former cases.

We can construct a generalization of the cluster approximation for configurations of the form in Eq. (2.31). As in the case of $|(210)^n\rangle$, the dynamics inside one unit cell explains the dynamics of the full system. The generalized clusters can be chosen in such a way that their Hilbert spaces are spanned by N configurations

$$|i\rangle = |((N+1-i)(i-1)\underbrace{0...0}_{N-2})^n\rangle, \tag{2.32}$$

where i takes values $1, 2, \ldots N$. If we consider only one unit cell ($n = 1$), the graph that connects these configurations has a linear structure without any loops, i.e., each configuration $|i\rangle$ is solely connected to the configurations $|i \pm 1\rangle$, except the two configurations at the edges,

$|1\rangle$ and $|N\rangle$, which are only connected to $|2\rangle$ and $|N-1\rangle$, respectively.

The projection of the Hamiltonian $\hat{H}_1$ to this cluster, which we denote by $\hat{H}_1^{\mathrm{c}}$, has a very simple structure: it has the form of a tight-binding chain with the only nonzero matrix elements on the upper and lower diagonals:

$$H^{\mathrm{c}}_{1;i,i+1} = H^{\mathrm{c}}_{1;i+1,i} = (N-i)\sqrt{i(N+1-i)}. \tag{2.33}$$

The dynamics within a single unit cell under $\hat{H}_1^{\mathrm{c}}$ corresponds to density fluctuations between the first and the second site. Following the same procedure as previously, we can now diagonalize $\hat{H}_1^{\mathrm{c}}$ and compute the fidelity time series for the initial configuration $|(N-1)10...0\rangle$. This result can be directly generalized to configurations of the form $|((N-1)10...0)^n\rangle$. The derivation is valid for both translation-invariant and non-translation-invariant initial configurations, as the cluster in Eq. (2.32) is disconnected from its translated copies. We stress that this disconnection, namely the absence of a hopping term between $|1(N-1)0...0\rangle$ and $|0N0...0\rangle$, is a consequence of the constraints imposed by $\hat{H}_1$ and it would not hold for $\hat{H}_2$. In this way, we have calculated the time evolution of the fidelity starting from the configurations $|(3100)^n\rangle$ (for $n = 1, 2, 3, 4$), $|(41000)^n\rangle$ ($n = 1, 2, 3$) and $|(510000)^n\rangle$ ($n = 1, 2$), and compared it with the exact numerical results for the full $\hat{H}_1$. The cluster approximation captures both the revival frequency and the height of the first peak. Similar to the $|(210)^n\rangle$ case, the approximation can be improved by adding further configurations to the clusters. Moreover, if we want to consider translation-invariant initial states, we can follow the same recipe for $|(210)^n\rangle$ by summing translated patterns with the required phase factors given in terms of momenta in multiples of $2\pi/N$. We have checked that revivals appear in these momentum sectors, with roughly the same frequency.

We note that the configurations with larger units cells thermalize more quickly on shorter timescales, but slower at long times. Initially, the states starting from configurations with smaller N have lower entanglement entropies than those with larger N. The Hilbert spaces of large N unit cells are larger, so the entanglement entropy starting from these configurations rapidly grows to the maximal value for that unit cell. However, the only way for the wavefunction to spread through the entire Hilbert space is that a unit cell reaches a state close to 111...111, so that particles can hop to the other unit cells. This is less likely for large N, and therefore such configurations need long times to fully thermalize. As a result, smaller N entanglement entropies grow faster and after long enough time they overtake those for larger N. For example, in the case of $L = 12$ and translation-invariant initial states, $(210)^4$ overtakes $(3100)^3$ and $(510000)^2$ around $t \sim 2$, and $(3100)^3$ overtakes $(510000)^2$ around $t \sim 80$, as shown in Fig. 2.11.

Finally, we note that non-thermal behavior reminiscent of the one studied here was previously observed in an unconstrained Bose-Hubbard model, for example in the context of "arrested expansion" [148, 149] and quenches from superfluid to Mott insulator phase [150, 151]. In these

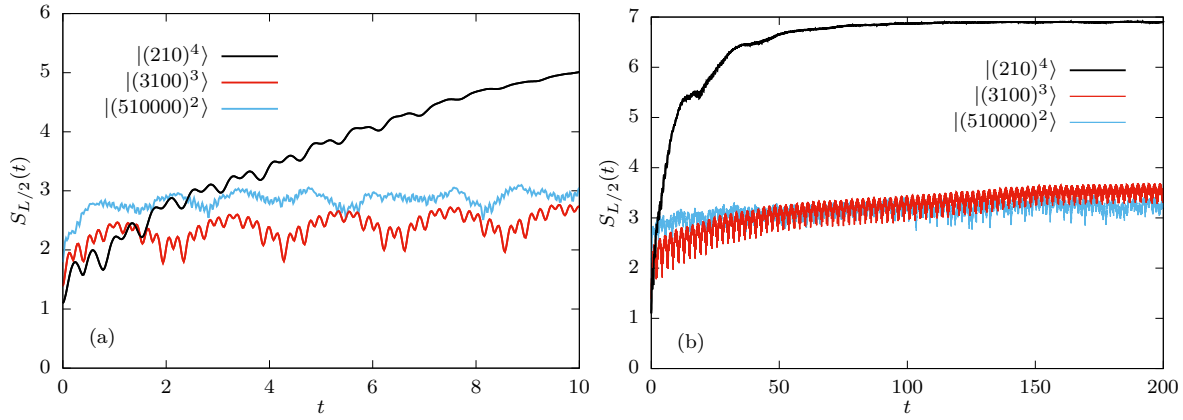

Figure 2.11: Time evolution of entanglement entropy for three different translation-invariant initial states which exhibit slow thermalization. (a) Short timescale. (b) Long timescale. System size $L = 12$. Configurations with larger unit cells (such as $|(510000)^2\rangle$), thermalize more quickly than those with smaller unit cells (such as $|(210)^4\rangle$) on shorter timescales, but slower at longer times.

cases, the main ingredient is the strong on-site interaction, which causes the energy spectrum to split into several bands. Due to the large energy differences between bands, the dynamics of an initial state from a particular band is at first limited only to the eigenstates that belong to the same band. Additionally, these energy bands are approximately equally spaced, which can lead to revivals in fidelity if several bands are populated. In contrast, our models do not feature on-site interaction, and the mechanism which slows down the spread of the wave function is correlated hopping, which suppresses connections between certain configurations and modifies the hopping amplitudes between others, thus creating bottlenecks that separate different clusters of states.

2.4 Zero modes

An interesting feature of $\hat{H}_1$ model is the large number of zero-energy states in the middle of its spectrum. The number of these zero modes, found by brute force diagonalization, is listed in Table 2.1 for different system sizes and momentum sectors. Similar property is found for $\hat{H}_2$ – see Table 2.2, with the notable difference that there are no zero modes when the number of sites L is odd.

The origin of the zero modes is the underlying bipartite structure of the Hamiltonian [143, 144]. As explained in Section 2.1.2, all the basis configurations of the $\hat{H}_1$ model can be separated into two disjoint classes, and the action of the Hamiltonian $\hat{H}_1$ only connects configurations in one class to the configurations in the other class, while $\hat{H}_1$ does not connect configurations within the same class. For example, a graph that shows how the configurations for $L = N_\mathrm{p} = 4$ are connected is displayed in Fig. 2.12. Here we will refer to the two classes as the "green" (even) and the "red" (odd) configurations. Each basis configuration can be uniquely assigned a

Table 2.1: The number of zero-energy states for the Hamiltonian $\hat{H}_1$ and different system sizes. The number of states is resolved per momentum sectors, denoted by their momentum indices i that parametrize the momenta $k_i = \frac{2\pi}{L} i$.

	$\frac{k_i L}{2\pi}$											
$L = N_\mathrm{p}$	0	1	2	3	4	5	6	7	8	9	10	total
2	0	1										1
3	0	1	1									2
4	2	0	1	0								3
5	2	1	1	1	1							6
6	2	3	0	4	0	3						12
7	2	3	3	3	3	3	3					20
8	10	0	8	0	9	0	8	0				35
9	8	8	8	7	8	8	7	8	8			70
10	4	25	2	25	2	26	2	25	2	25		138
11	22	23	23	23	23	23	23	23	23	23	23	252

Table 2.2: The number of zero-energy states for the Hamiltonian $\hat{H}_2$ and different system sizes. The columns are the same as in Table 2.1.

	$\frac{k_i L}{2\pi}$											
$L = N_\mathrm{p}$	0	1	2	3	4	5	6	7	8	9	10	total
2	0	1										1
3	0	0	0									0
4	2	0	1	0								3
5	0	0	0	0	0							0
6	0	3	0	4	0	3						10
7	0	0	0	0	0	0	0					0
8	10	0	8	0	9	0	8	0				35
9	0	0	0	0	0	0	0	0	0			0
10	0	25	0	26	0	26	0	26	0	25		128
11	0	0	0	0	0	0	0	0	0	0	0	0

green or a red label according to the parity of its distance d_a from the configuration $|111...111\rangle$, Eq. (2.7). If this number is even, the configuration is green, and if it is odd, the configuration is red.

This separation into two classes is a consequence of the constraints present in the Hamiltonian $\hat{H}_1$. Hamiltonians without such constraints, for example $\hat{H}_2$ or the standard Bose-Hubbard model, do not exhibit this bipartite structure for odd system sizes, see Section 2.1.2. for more details. In these cases, it is not possible to uniquely determine whether a particular configuration is green or red. The lack of bipartite structure is the reason for the absence of zero-energy eigenstates of $\hat{H}_2$ in odd dimensions, which was observed in Table 2.2. However, the configuration space of $\hat{H}_2$ is still bipartite in even dimensions, allowing for the existence of some zero modes in those cases.

Low-entropy zero-energy states can be constructed as superpositions of either only green or

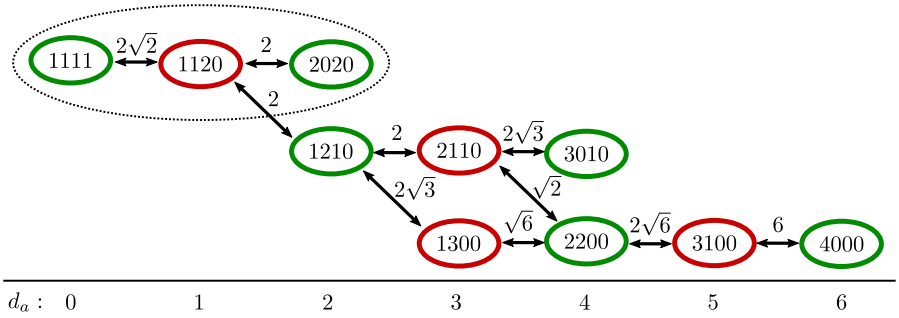

Figure 2.12: Bipartite graph for $\hat{H}_1$ and $L = N_\mathrm{p} = 4$. The two classes of configurations are shown in green (even) and red (odd) ellipses. The configurations are written in the translation-invariant basis. The arrows represent the action of the Hamiltonian $\hat{H}_1$ and the numbers above the arrows are the magnitudes of the corresponding hopping coefficients. The numbers bellow the graph show the distance d_a from the configuration 1111, as defined in Eq. (2.7).

only red configurations. For example, in the case of $L = N_\mathrm{p} = 4$, the simplest and therefore the lowest-entropy zero mode can be constructed using only two green product states (encircled by a dashed line in Fig. 2.12)

$$|\psi_0\rangle = \frac{1}{\sqrt{3}}|1111\rangle - \sqrt{\frac{2}{3}}|2020\rangle_\mathrm{T}, \tag{2.34}$$

where $|\ldots\rangle_T$ was defined in Eq. (2.19). There is another zero mode in this case, and it can be formed by adding more green configurations to the superposition. The number of zero-energy eigenstates is related to the difference between the numbers of green and red configurations [143], as we will now explain.

As the Hamiltonian $\hat{H}_1$ only connects green configurations to red configurations and red to green, we can rewrite it in the following way:

$$\hat{H}_1 = \sum_{i,j} c_{ij}|R_i\rangle\langle G_j| + \sum_{i,j} c_{ij}^\dagger|G_j\rangle\langle R_i|, \tag{2.35}$$

where $|R_i\rangle$ are the red product states and $|G_j\rangle$ are green. Its square, $\hat{H}_1^2$, connects green configurations to green and red to red, and it is therefore block diagonal. The blocks are $\hat{C}\hat{C}^\dagger$ and $\hat{C}^\dagger\hat{C}$, where $\hat{C}$ is a matrix with the elements c_{ij}. The dimensions of $\hat{C}$ are $r \times g$, where r is the number of red configurations and g of green. $\hat{C}$ and $\hat{C}^\dagger$ can be factorized using singular value decomposition. From this structure we can see that the energy spectrum is symmetric around zero and that the minimal number of zero-energy states is $|g - r|$. The zero-energy eigenvectors can also be obtained as the ground states of $\hat{H}_1^2$. Similar analysis and counting of the zero modes in PXP model was performed in Ref. [47, 152].

Table 2.3 shows the difference between the numbers of red and green states $g-r$ for different system sizes and the number of zero-energy states N_0 in those systems. The number of zero-energy states, found by exact diagonalization, in all cases satisfies the anticipated inequality

Table 2.3: The difference between the number of green and red configurations $g - r$ and the number of zero-energy states N_0 (determined by exact diagonalization) for different system sizes. Overall, the derived bound for the number of zero modes is found to be very tight in finite systems where it can be independently confirmed by explicit diagonalization ("NA" denotes cases where this was not possible).

	all sectors		$k = 0$	
$L = N_\mathrm{p}$	$g - r$	N_0	$g - r$	N_0
2	-1	1	0	0
3	-2	2	0	0
4	3	3	2	2
5	6	6	2	2
6	-10	12	0	2
7	-20	20	-2	2
8	35	35	10	10
9	70	70	8	8
10	-126	138	0	4
11	-252	252	-22	22
12	462	NA	80	80
13	924	NA	72	NA
14	-1716	NA	0	NA
15	-3432	NA	-228	NA
16	6435	NA	810	NA

$N_0 \geq |g - r|$. In fact, the bound is almost always saturated, $N_0 = |g - r|$, except when $L = N_\mathrm{p} = 4n + 2$, $n \in \mathbb{Z}$. Interestingly, the minimal number of zero modes $|g - r|$ for $L = N_\mathrm{p} = 4n$ is equal to the Hilbert space dimension for $L = N_\mathrm{p} = 2n$ (both total and for $k = 0$ sector only). This leads to the conclusion that the number of zero-energy states grows exponentially with the system size. It can also be noticed that the total difference $g - r$ for $L = N_\mathrm{p} = 2n + 1$ is always twice the difference for $L = N_\mathrm{p} = 2n$.

2.5 Conclusions

In this Chapter, we have introduced three models of bosons with "soft" kinetic constraints, i.e., density-dependent hopping. We have demonstrated that some of these models exhibit similar phenomenology to other realizations of quantum many-body scars, for example the Rydberg atom system [46]. We have studied quantum dynamics of these systems by performing global quenches from tensor-product initial states. We have shown that both the connectivity of the Hilbert space and the relative magnitude of the hopping coefficients have dramatic effects on the dynamics. For certain initial configurations, the constraints can lead to slow thermalization and revivals in the quantum fidelity. The revival frequency can be predicted by considering an exponentially reduced subset of the Hilbert space. For a family of initial configurations of the form $|(210)^n\rangle$, we have derived analytical expressions for the evolution of quantum fidelity

within this approximation, which accurately capture the revival frequency obtained from exact numerical data. One notable difference between scarred dynamics in the present bosonic models and the PXP model is that the revivals exist in the absence of a hard kinetic constraint, i.e., in the fully connected Hilbert space. Our cluster approximation also explains the structure of some low-entropy eigenstates in the middle of the many-body spectrum. In addition, we have calculated the evolution of two local observables which are experimentally measurable, density correlations between two neighboring sites and density on a single site, and both of them show robust oscillations over a range of system sizes. We have also shown that the introduced models contain additional special properties, like the exponentially large zero-energy degeneracy which is related to the bipartite structure of the model.

We now comment on the possible experimental realizations of the models we studied. The implementation of a correlated hopping term ($\hat{n}_k \hat{b}_i^\dagger \hat{b}_j$) in optical lattices has attracted lot of attention due to a possible onset of quantum phases related to high-Tc superconductivity [153]. An early theoretical proposal exploits asymmetric interactions between the two atomic states in the presence of a state-dependent optical lattice [153]. As a result, the obtained effective model corresponds to the inversion-symmetric form of $\hat{H}_1$. In addition, the same term has been found to feature as a higher-order correction of the standard Bose-Hubbard model [154–157]. Although in this case the term typically represents a modification of the regular hopping term of the order of several percent, its contribution was directly measured [158, 159]. More recently, the set of quantum models accessible in cold-atom experiments has been enriched through the technique of Floquet engineering [86]. As a notable example, a suitable driving scheme can renormalize or fully suppress the bare tunneling rate [160]. On top of that, by modulating local interactions an effective model with the density-dependent tunneling term has been engineered [161]. For the models considered in this Chapter the most promising is a more recent driving scheme exploiting a double modulation of a local potential and on-site interactions [162]. Related sophisticated driving schemes have already enabled a realization of dynamical gauge fields [124, 125, 163] where both the amplitude and the phase of the effective tunneling are density-dependent. Although these experimental proposals explain how to realize some of the correlated hopping terms present in our models using ultracold atoms in optical lattices, finding a scheme that exactly realizes our models requires further study. We emphasize that other models which would exhibit non-ergodic dynamics and scarred eigenstates as a result of the same mechanism that was explained in this work could be built, for example a linear combination of $\hat{H}_1$ and $\hat{H}_2$.

During the completion of this work, we became aware of Ref. [164] which identified non-thermal eigenstates and slow dynamics in the quantum East model. Moreover, a recent study [165] proposed a Floquet scheme for a bosonic model with density-assisted hopping, finding signatures of quantum many-body scars.

Chapter 3

Dynamics of weakly interacting bosons in optical lattices with flux

As already discussed in Section 1.4, a big challenge in the field of ultracold atoms was realization of synthetic magnetic fields, due to the fact that charge-neutral atoms do not feel the Lorentz force. Magnetic field is a key ingredient in various condensed-matter models with nontrivial topological content, such as the the Harper-Hofstadter [68] and the Haldane model [76]. In recent years, the implementation of artificial gauge potentials for neutral atoms [74, 75] has finally enabled the realization of these important models using ultracold atoms in optical lattices [77–80].

Cold-atom realizations of topological models exploit periodic driving, either through laser-assisted tunneling [77, 78] or by lattice shaking [79]. Using Floquet theory [81, 89], a periodically driven system can be related to the time-independent effective Hamiltonian that describes a condensed-matter system of interest. The mapping is known as Floquet engineering and its important features in the context of optical lattices are discussed in Section 1.5 and Refs. [82–88, 166]. Because of important differences of cold-atom setups and their condensed-matter counterparts, new quench protocols for probing topological features were proposed [167–171]. Following up on these studies, a novel experimental protocol was developed which allowed for the first-ever measurement of the Chern number (1.5) in a nonelectronic system by investigating the anomalous deflection of an atomic cloud as a response to external force [70]. The Chern number is a topological invariant which was directly related to the quantization of the Hall conductivity in the integer Hall effect [69].

While Floquet engineering is a highly flexible and powerful technique, it poses several concerns. One of the main open questions is related to the interplay of driving and interactions which causes heating and can quickly lead the system to a featureless, infinite-temperature regime [94, 96]. In particular, it is shown that an initial Bose-Einstein condensate in a periodically driven optical lattice may become unstable due to two-body collisions [172] or through

the mechanism of parametric resonance [96, 173–179]. The preparation protocol, stability and a lifetime of strongly correlated phases, expected in the regime of strong interactions under driving is a highly debated topic at the moment [96, 180, 181].

In order to further explore the role of weak atomic interactions in probing topological features, here we consider the dynamics of weakly interacting incoherent bosons in a driven optical lattice exposed to an external force. The setup that we consider includes all basic ingredients for the Chern-number measurement [70, 168] – the Chern number of the topological band can be extracted from the center-of-mass motion of atomic cloud in the direction transverse to the applied force. We assume an ideal initial state where the lowest topological band of the effective model is almost uniformly populated. The optimal loading sequence necessary to reach this state is considered in Refs. [182, 183]. Following the recent experimental study [70], we assume that atoms are suddenly released from the trap and exposed to a uniform force. We perform numerical simulations for the full time-dependent Hamiltonian and take into account the effects of weak repulsive interactions between atoms within the mean-field approximation. We make a comparison between the dynamics governed by the effective and time-dependent Hamiltonian and delineate the contribution of interactions to the center-of-mass response and to the overall cloud expansion dynamics. Our results show that interactions lead to the undesirable atomic transitions between topological bands [184], but we also find that a weak atomic repulsion can facilitate the Chern-number measurements in several ways.

This Chapter is organized as follows. In Section 3.1 we describe the model and introduce a method that we apply for the description of incoherent bosons. In Section 3.2 we address the dynamics of noninteracting incoherent bosons, and then in Section 3.3 we address the regime of weak repulsive interactions. Finally, we summarize our results in Section 3.4. Appendixes C to F provide further details.

3.1 Model and method

In this section, we first present the driven model introduced in Ref. [70], and then derive the corresponding effective model and discuss its basic characteristics. At the end, we explain our choice of the initial state and outline the method that we use to treat the dynamics of weakly interacting incoherent bosons.

3.1.1 Effective Floquet Hamiltonian

Interacting bosons in a two-dimensional optical lattice can be described by the Bose-Hubbard Hamiltonian

$$\begin{aligned}\hat{H}_{\mathrm{BH}} &= -J_x \sum_{l,m} \left(\hat{a}^\dagger_{l+1,m}\hat{a}_{l,m} + \hat{a}^\dagger_{l-1,m}\hat{a}_{l,m}\right) - J_y \sum_{l,m} \left(\hat{a}^\dagger_{l,m+1}\hat{a}_{l,m} + \hat{a}^\dagger_{l,m-1}\hat{a}_{l,m}\right) \\ &+ \frac{U}{2}\sum_{l,m} \hat{n}_{l,m}\left(\hat{n}_{l,m}-1\right), \end{aligned} \tag{3.1}$$

where $\hat{a}^\dagger_{l,m}$ and $\hat{a}_{l,m}$ are creation and annihilation operators that create and annihilate a particle at the lattice site $(l,m) = la\mathbf{e}_x + ma\mathbf{e}_y$ (a is the lattice constant), $\hat{n}_{l,m} = \hat{a}^\dagger_{l,m}\hat{a}_{l,m}$ is the number operator, J_x and J_y are the hopping amplitudes along $\mathbf{e}_x$ and $\mathbf{e}_y$, and U is the on-site interaction. In the derivation of the model (3.1) we use the single-band tight-binding approximation [5]. Although the experimental setup [70] is actually three dimensional, with an additional confinement in the third direction, our study is simplified to a two-dimensional lattice.

In order to engineer artificial gauge field in the experiment [70], hopping along $\mathbf{e}_x$ was at first inhibited by an additional staggered potential

$$\hat{W} = \frac{\Delta}{2}\sum_{l,m}(-1)^l \hat{n}_{l,m}, \tag{3.2}$$

and then restored using resonant laser light. For more details, see Fig. 1.5 in Chapter 1. The experimental setup can be described by a time-dependent Hamiltonian

$$\tilde{H}(t) = \hat{H}_{\mathrm{BH}} + \hat{V}(t) + \hat{W}, \tag{3.3}$$

where $\hat{V}(t)$ is a time-dependent modulation

$$\begin{aligned}\hat{V}(t) = \kappa \sum_{l,m} \hat{n}_{l,m}\Bigg[&\cos\left(\frac{l\pi}{2}-\frac{\pi}{4}\right)\cos\left(\omega t - \frac{m\pi}{2}+\phi_0\right) \\ &+\cos\left(\frac{l\pi}{2}+\frac{\pi}{4}\right)\cos\left(-\omega t - \frac{m\pi}{2}+\frac{\pi}{2}+\phi_0\right)\Bigg], \end{aligned} \tag{3.4}$$

κ is the driving amplitude, and $\omega = \Delta$ is the resonant driving frequency. We set the relative phase ϕ_0 between the optical-lattice potential and the running waves used for laser-assisted tunneling to $\phi_0 = \pi/4$.

Using Floquet theory, see Eq. (1.9), the time-evolution operator corresponding to the Hamiltonian (3.3) can be represented as

$$\hat{U}(t,t_0) = \mathrm{e}^{-i\hat{W}t}\mathrm{e}^{-i\hat{K}(t)}\mathrm{e}^{-i(t-t_0)\hat{H}_{\mathrm{eff}}}\mathrm{e}^{i\hat{K}(t_0)}\mathrm{e}^{i\hat{W}t_0}, \tag{3.5}$$

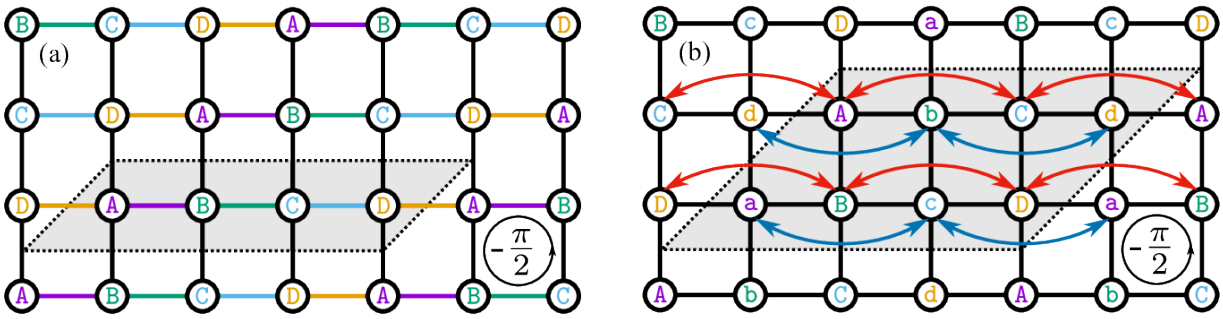

Figure 3.1: Schematic representation of the model. The unit cells are shaded. (a) Effective Hamiltonian without correction, $\hat{H}_{\text{eff},0}$ (3.6). Vertical links correspond to real hopping amplitudes (along $\mathbf{e}_y$ direction), while the horizontal links to the right of lattice sites labeled `A`, `B`, `C`, and `D` correspond to complex hopping amplitudes with phases $\frac{3\pi}{4}$, $\frac{\pi}{4}$, $-\frac{\pi}{4}$, and $-\frac{3\pi}{4}$, respectively (when hopping from left to right). (b) Effective Hamiltonian with correction, $\hat{H}_{\text{eff},1}$ (3.7). Red lines represent positive next-nearest-neighbor hopping amplitudes (connecting uppercase letters), while the blue lines represent negative next-nearest-neighbor hopping amplitudes (connecting lowercase letters). Nearest-neighbor hopping amplitudes are the same as in (a).

where $\hat{H}_{\text{eff}}$ is the full time-independent effective Hamiltonian that describes slow motion and $\hat{K}(t)$ is the time-periodic kick operator that describes micromotion [82, 83].

For the moment, in this subsection we first consider the noninteracting model $U = 0$. We also assume that the driving frequency ω is the highest energy scale, but that it is still low enough that the lowest-band approximation used in deriving Eq. (3.1) is still valid. In the leading order of the high-frequency expansion, the effective Hamiltonian $\hat{H}_{\text{eff}}$ is given by

$$\hat{H}_{\text{eff},0} = J'_x \sum_{l,m} \left[\mathrm{e}^{i\left((m-l-1)\pi/2-\pi/4\right)} \hat{a}^\dagger_{l+1,m} \hat{a}_{l,m} + \text{H.c.} \right] - J'_y \sum_{l,m} \left(\hat{a}^\dagger_{l,m+1} \hat{a}_{l,m} + \hat{a}^\dagger_{l,m-1} \hat{a}_{l,m} \right), \tag{3.6}$$

where the renormalized hopping amplitudes are $J'_x = \frac{J_x \kappa}{\sqrt{2}\omega} = J_y$ and $J'_y = J_y\left(1 - \frac{1}{2}\frac{\kappa^2}{\omega^2}\right)$. A schematic representation of this model is presented in Fig. 3.1(a). The unit cell is shaded and the full lattice is spanned by the vectors $\mathbf{R}_1 = (4, 0)$ and $\mathbf{R}_2 = (1, 1)$. Particle hopping around a plaquette in the counterclockwise direction acquires a complex phase $-\frac{\pi}{2}$ and the model is equivalent to the Harper-Hofstadter Hamiltonian [68] for the case $\alpha = 1/4$ [68]. The explicit form of the kick operator $\hat{K}(t)$ from Eq. (3.3) is given in Appendix C.

Following Refs. [82, 83], we find that additional corrections of the order J_x^2/ω contribute to the system's dynamics and we introduce another approximation for the effective Hamiltonian

$$\hat{H}_{\text{eff},1} = \hat{H}_{\text{eff},0} + \frac{J_x^2}{\omega} \sum_{l,m} (-1)^l \left(2\hat{a}^\dagger_{l,m} \hat{a}_{l,m} + \hat{a}^\dagger_{l+2,m} \hat{a}_{l,m} + \hat{a}^\dagger_{l-2,m} \hat{a}_{l,m} \right). \tag{3.7}$$

The derivation of Hamiltonian (3.7) is given in Appendix C and its schematic representation is given in Fig. 3.1(b). The J_x^2/ω correction introduces next-nearest-neighbor hopping along x direction with opposite signs for lattice sites with either even or odd x-coordinate l. This term

does not change the total complex phase per plaquette, but the unit cell is now doubled and thus the first Brillouin zone is halved. A similar term was engineered on purpose in order to implement the Haldane model [79].

In the next subsection we investigate properties of energy bands of both effective Hamiltonians, $\hat{H}_{\text{eff},0}$ and $\hat{H}_{\text{eff},1}$. We use the units where $\hbar = 1$ and $a = 1$. Unless otherwise stated, we set the parameters to the following values: lattice size 100×100 sites, hopping amplitudes $J'_x = J_y = 1 \equiv J$, and the driving amplitude $\kappa = 0.58\ \omega$. This value of the driving amplitude was chosen to be the same as in the experiment [70]. In order to set the renormalized hopping amplitude along $\mathbf{e}_x$ to $J'_x = 1$, the initial hopping amplitude has to be $J_x = \sqrt{2}\omega/\kappa = 2.44$, and the correction term is therefore proportional to $J_x^2/\omega = 5.95/\omega$, so it cannot be safely neglected unless the driving frequency is very high.

3.1.2 Band structure

Momentum-space representations of the effective Hamiltonians $\hat{H}_{\text{eff},0}$ and $\hat{H}_{\text{eff},1}$, denoted by $\hat{\mathcal{H}}_{\text{eff},0}(\mathbf{k})$ and $\hat{\mathcal{H}}_{\text{eff},1}(\mathbf{k})$, respectively, are derived in Appendix C. Band structures for the effective Hamiltonian $\hat{\mathcal{H}}_{\text{eff},0}$ without the J_x^2/ω correction, Eq. (C.20), as well as for the effective Hamiltonian $\hat{\mathcal{H}}_{\text{eff},1}$ including the correction term, Eq. (C.21), are shown in Fig. 3.2 for the two values of driving frequencies $\omega = 20$ and $\omega = 10$.

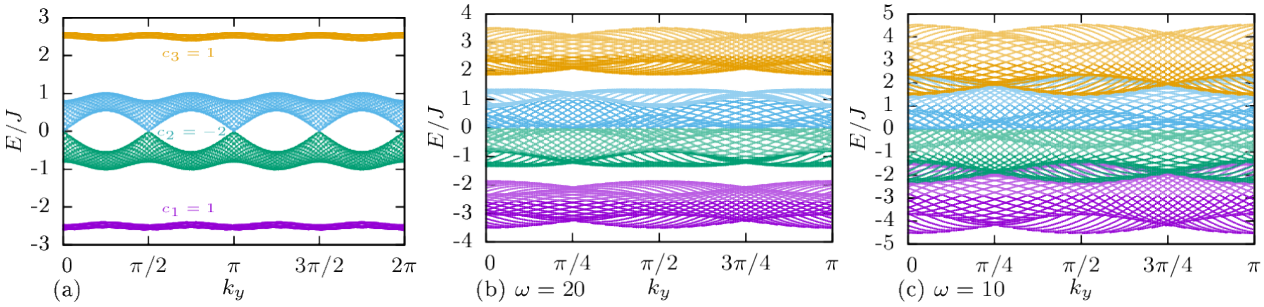

Figure 3.2: Energy bands of the effective Hamiltonians. (a) $\hat{\mathcal{H}}_{\text{eff},0}(\mathbf{k})$ Eq. (C.20), which is without the J_x^2/ω correction term. (b) $\hat{\mathcal{H}}_{\text{eff},1}(\mathbf{k})$ Eq. (C.21), which includes the correction term. Driving frequency $\omega = 20$; gaps are open. (c) Same as (b), but with $\omega = 10$. Gaps are closed.

The Hamiltonian $\hat{H}_{\text{eff},0}$ is the Harper-Hofstadter Hamiltonian (1.4) for the flux $\alpha = 1/4$. It has four energy bands, where the middle two bands touch at $E = 0$ and can therefore be regarded as a single band; see Fig. 3.2(a). The topological content of these bands is characterized by the topological index called the Chern number (1.5). The Chern numbers of the three well-separated bands are $c_1 = 1$, $c_2 = -2$, and $c_3 = 1$.

Because the correction from Eq. (3.7) includes next-nearest-neighbor hopping terms, the elementary cell in real space is doubled [see Fig. 3.1(b)] and, as a consequence, the first Brillouin zone for the Hamiltonian $\hat{\mathcal{H}}_{\text{eff},1}$ is reduced by a factor of 2 compared to $\hat{\mathcal{H}}_{\text{eff},0}$. There are now eight lattice sites in the unit cell and eight energy bands, but the number of gaps depends on the

driving frequency. The new bands touch in pairs, in such a way that there are always maximally three well-separated bands. When the driving frequency is high enough, the correction is small and the gaps between the three bands remain open; see Fig. 3.2(b). The original band structure of $\hat{\mathcal{H}}_{\text{eff},0}$ is recovered in the limit $\omega \to \infty$. The Berry curvature and the Chern number can be calculated using the efficient method presented in Ref. [185]. Our calculations confirm that the Chern numbers of $\hat{\mathcal{H}}_{\text{eff},1}$ are equal to those of $\hat{\mathcal{H}}_{\text{eff},0}$ ($c_1 = 1$, $c_2 = -2$, and $c_3 = 1$), as long as the gaps between the energy bands are open. The gaps close when the driving frequency is too low, see Fig. 3.2(c), and the Chern numbers of the subbands can no longer be properly defined.

3.1.3 Dynamics of incoherent bosons

We need to take into account a contribution of weak, repulsive interactions. Full numerical simulations of an interacting many-body problem are computationally demanding, so we need a reasonable, numerically tractable approximation. To this end we will use the classical field method [186], which belongs to a broader class of truncated Wigner approaches [187]. This method is similar to the approach used to treat incoherent light in instantaneous media [188, 189], known in optics as the modal theory.

The underlying idea of the method is to represent the initial state as an incoherent mixture of coherent states $|\psi\rangle$, $\hat{a}_{l,m}|\psi\rangle = \psi_{l,m}|\psi\rangle$ [186]. This is explained in more detail in Appendix D. In our study, we sample initial configurations of these coherent states with

$$|\psi(t=0)\rangle = \sum_{k=1}^{N_m} \mathrm{e}^{i\phi_k}|k\rangle, \tag{3.8}$$

where $\phi_k \in [0, 2\pi)$ are random phases and the states $|k\rangle$ correspond closely to the lowest-band eigenstates of $\hat{H}_{\text{eff}}$. Each of N_{samples} initial states is time evolved and physical variables can be extracted by averaging over an ensemble of different initial conditions.

The time evolution of each of these coherent states is governed by

$$i\frac{d\psi_{l,m}(t)}{dt} = \sum_{ij} H_{lm,ij}(t)\psi_{i,j}(t) - F\,m\,\psi_{l,m}(t) + U|\psi_{l,m}(t)|^2\psi_{l,m}(t), \tag{3.9}$$

where $H_{lm,ij}(t) = \langle l, m|\hat{H}(t)|i, j\rangle$ are matrix elements of $\hat{H}(t)$ from Eq. (3.3), F is the external force, and interactions U contribute with the last, nonlinear term. Formally, Eq. (3.9) takes the form of the Gross-Pitaevskii equation [1, 190, 191]. The performances and limitations of the method are discussed and reviewed in Ref. [192].

For comparison, we also consider the related time evolution governed by the effective Hamiltonian

$$i\frac{d\psi_{l,m}(t)}{dt} = \sum_{ij} h^{\text{eff}}_{lm,ij}\psi_{i,j}(t) - F\,m\,\psi_{l,m}(t) + U|\psi_{l,m}(t)|^2\psi_{l,m}(t), \tag{3.10}$$

where $h^{\text{eff}}_{lm,ij} = \langle l, m|\hat{h}^{\text{eff}}|i, j\rangle$, with $\hat{h}^{\text{eff}}$ being either $\hat{H}_{\text{eff},0}$ from Eq. (3.6), or $\hat{H}_{\text{eff},1}$ from Eq. (3.7). Equation (3.10) should be considered only as a tentative description of the system: the mapping between $\hat{H}(t)$ and $\hat{H}_{\text{eff}}$ is strictly valid only in the noninteracting regime and the interaction term may introduce complex, nonlocal, higher-order corrections [94]. However, we expect their contribution to be small in the limit $U \to 0$, and for time scales which are not too long [97, 98, 193, 194].

In the following we use $N_m = 300$ modes and accommodate $N_p = 300$ particles per mode, so in total in the simulations we have $N = N_m N_p = 90,000$ bosons. Typical densities in real space are up to 100 particles per site and we choose the values of U in the range $U \in [0, 0.05]$. Other parameters: $J'_x = J_y = 1$, $\kappa/\omega = 0.58$, $\omega = 10, 20$, and $F = 0.25J/a$. The correction terms are non-negligible in this frequency range. In practice, we first numerically diagonalize the Hamiltonian (D.2) from Appendix D and set our parameters in such a way that the lowest N_m modes have high overlap with the lowest band of the effective model. In the next step, we sample initial configurations (3.8). For each of $N_{\text{samples}} = 1,000$ sets of initial conditions we then time evolve Eq. (3.9) and extract quantities of interest by averaging over resulting trajectories. This value of N_{samples} is chosen to be high enough, so that the fluctuations are weak. We present and discuss results of our numerical simulations in the following sections.

3.2 Noninteracting case

We start by addressing the dynamics of noninteracting bosons. In this case we set $U = 0$ in Eq. (3.9) and numerically solve the single-particle Schrödinger equation without further approximations. Our aim is to numerically validate and compare the two approximations, Eqs. (3.6) and (3.7), for the effective Hamiltonian. To this purpose, we juxtapose results of the two approximative schemes with the numerically exact results obtained by considering the full time evolution governed by $\hat{H}(t)$. For clarity, the four different time evolutions that we consider in this section are summarized in Table 3.1. We calculate the center-of-mass position $x(t)$ and plot the results in Fig. 3.3. In this way we also find the regime of microscopic parameters where the Chern-number measurement can be optimally performed.

First, we consider the basic Harper-Hofstadter Hamiltonian (3.6) and select the occupied modes $|k\rangle$ of the initial state (D.1) as eigenstates of the model from Eq. (3.8) for $\hat{h}_{\text{eff}} = \hat{H}_{\text{eff},0}$. As explained in the previous section, at the initial moment $t_0 = 0$, the confinement is turned off and the force $\mathbf{F} = -F\mathbf{e}_y$ is turned on. As a consequence of the applied external force and the nonzero Chern number of the lowest band of the model (3.6), the particles exhibit an anomalous velocity in the direction perpendicular to the force [71]. In the ideal case, when the lowest band is fully populated, the theoretical prediction for the center-of-mass position in the

Table 3.1: Four different cases: the same effective Hamiltonian is always used for the initial state and band definitions, either with or without the correction. The evolution is governed either by the time-dependent Hamiltonian or by the same effective Hamiltonian as the one that was used for the initial state and calculation of band populations.

case	initial state	band populations	evolution
1	$\hat{H}_{\text{eff},1}$	$\hat{H}_{\text{eff},1}$	$\hat{H}_{\text{eff},1}$
2	$\hat{H}_{\text{eff},1}$	$\hat{H}_{\text{eff},1}$	$\hat{H}(t)$
3	$\hat{H}_{\text{eff},0}$	$\hat{H}_{\text{eff},0}$	$\hat{H}_{\text{eff},0}$
4	$\hat{H}_{\text{eff},0}$	$\hat{H}_{\text{eff},0}$	$\hat{H}(t)$

$\mathbf{e}_x$ direction is [70]

$$x(t) = x(t_0) + c_1 \frac{2Fa^2}{\pi\hbar} t, \tag{3.11}$$

where $c_1 = 1$ is the Chern number (1.5) of the lowest band. However, even in the ideal case, due to the sudden quench of the linear potential, a fraction of particles is transferred to the higher bands. To take this effect into account, the authors of Ref. [70] introduced a filling factor $\gamma(t)$

$$\gamma(t) = \eta_1(t) - \eta_2(t) + \eta_3(t), \tag{3.12}$$

where $\eta_i(t)$ are populations of different bands of Hamiltionian (3.6) from Eq. (D.4) in Appendix D and the plus and minus signs in Eq. (3.12) are defined according to the Chern numbers $c_1 = 1$, $c_2 = -2$, and $c_3 = 1$. The final theoretical prediction is then [70]

$$x(t) = x(t_0) + c_1 \frac{2Fa^2}{\pi\hbar} \int_0^t \gamma(t')dt'. \tag{3.13}$$

In Fig. 3.3(a) we consider the anomalous drift for a high value of the driving frequency $\omega = 20$, where we expect the expansion in $1/\omega$ to be reliable. We find an excellent agreement between the prediction (3.13) (dotted black line) and numerical calculation based on $\hat{H}_{\text{eff},0}$ (solid green line). However, some deviations between the full numerical results (dashed purple line) and the results of the approximation scheme (solid green line) are clearly visible. These deviations are even more pronounced for $\omega = 10$, Fig. 3.3(b).

Now we turn to the effective model (3.7). In this case we select the modes of the initial state as eigenstates of Eq. (3.8) for $\hat{h}_{\text{eff}} = \hat{H}_{\text{eff},1}$. Moreover, we also consider band populations (D.4) of the same model. In the case when $\omega = 20$, Fig. 3.3(c), the anomalous drift obtained using the effective Hamiltonian (3.7) (solid green line) closely follows the theoretical prediction (3.13). Moreover, from the same figure we can see that the effective Hamiltonian $\hat{H}_{\text{eff},1}$ reproduces the behavior of the time-dependent Hamiltonian very well. All three curves almost overlap for intermediate times ($5-40$ ms); see Fig. 3.3(c). We attribute the long-time (> 45 ms) deviations to the finite-size effects introduced by the next-nearest-neighbor hopping terms, which cause

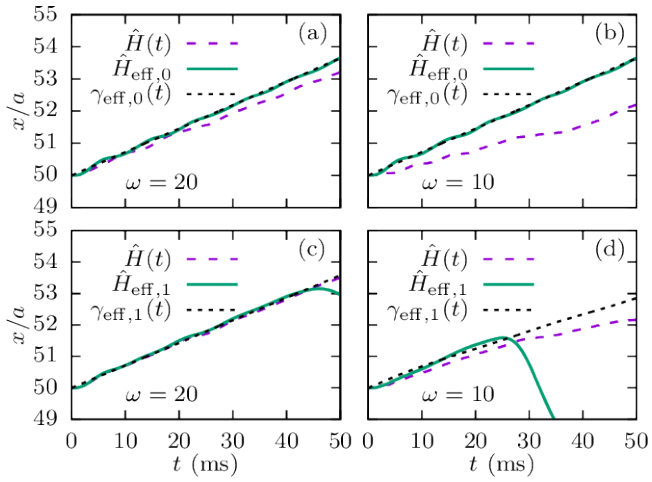

Figure 3.3: Anomalous drift $x(t)$. Dashed purple lines: numerical simulations using the time-dependent Hamiltonian $\hat{H}(t)$ (cases 2 and 4 from Table 3.1). Solid green lines: effective Hamiltonians $\hat{H}_{\mathrm{eff},1}$ (c) and (d) and $\hat{H}_{\mathrm{eff},0}$ (a) and (b) (cases 1 and 3). Dotted black lines: theoretical prediction (3.13) from $\gamma_{\mathrm{eff},1}(t)$ or $\gamma_{\mathrm{eff},0}(t)$. (a) Initial states and band populations obtained using the effective Hamiltonian $\hat{H}_{\mathrm{eff},0}$ without the correction (cases 3 and 4). Driving frequency $\omega = 20$. (b) $\omega = 10$. (c) Hamiltonian $\hat{H}_{\mathrm{eff},1}$ with the J_x^2/ω correction (cases 1 and 2). Driving frequency $\omega = 20$. (d) $\omega = 10$.

the atomic cloud to reach the edge of the lattice faster. This effect is explained in more detail in Section 3.3.2.

For a lower driving frequency $\omega = 10$, the effective and the time-dependent Hamiltonians do not agree so well anymore; see Fig. 3.3(d). The finite-size effects can be observed even earlier in this case (around 25 ms). This happens because the next-nearest-hopping terms are inversely proportional to the driving frequency. It is interesting to note that the prediction (3.13) is close to numerical data for short times even in this case when the gaps of the effective model are closed, see Fig. 3.2(c), and the Chern number of the lowest band is not well defined. In fact, it is surprising that the anomalous drift even exists in this case, as all subbands are now merged into a single band. We attribute this effect to our choice of the initial state. When the gaps are closed, it is hard to set the parameters in such a way that the lowest band is completely filled. The top of this band usually remains empty, and the particles thus do not "see" that the gap is closed.

Time evolution of the filling factor $\gamma(t)$ is plotted in Fig. 3.4 for four different cases from Table 3.1 – evolution using the effective Hamiltonian without correction $\hat{H}_{\mathrm{eff},0}$ [$\gamma_{\mathrm{eff},0}(t)$, case 3, dashed green line in Fig. 3.4(a)], the effective Hamiltonian with correction $\hat{H}_{\mathrm{eff},1}$ [$\gamma_{\mathrm{eff},1}(t)$, case 1, dashed green line in Fig. 3.4(b)], or the time-dependent Hamiltonian $\hat{H}(t)$ [$\gamma(t)$, cases 2 and 4, solid purple lines]. At the initial moment $\gamma(t_0 = 0) < 1$, because the initial state was multiplied by the operator $\mathrm{e}^{-i\hat{K}(0)}$. This introduces a shift between $\gamma(t)$ and $\gamma_{\mathrm{eff},1}(t)$. Apart from the shift, these two curves behave similarly, unlike the $\gamma_{\mathrm{eff},0}(t)$ curve that exhibits completely different behavior. Because of this, we use only $\gamma_{\mathrm{eff},1}(t)$ to estimate the value of the prediction (3.13).

We find that the values of $\gamma_{\mathrm{eff},1}(t)$ for $\omega = 20$ are high: ≥ 0.95; see Fig. 3.4. For this

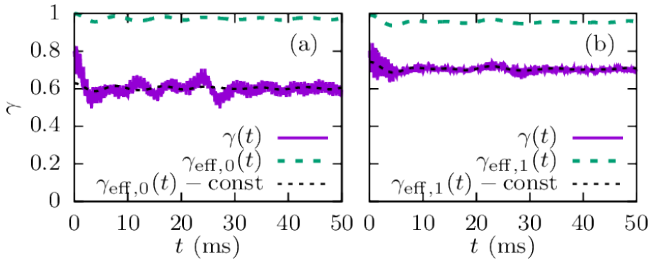

Figure 3.4: Time evolution of the filling factor $\gamma(t)$ for driving frequency $\omega = 20$. Solid purple lines: evolution governed by the time-dependent Hamiltonian $\hat{H}(t)$ (cases 2 and 4 from Table 3.1). Dashed green lines: evolution governed by the effective Hamiltonian $\hat{H}_{\mathrm{eff},1}$ or $\hat{H}_{\mathrm{eff},0}$ (cases 1 and 3). Dotted black lines: green lines shifted in order to compare them with purple lines. Shift is chosen so that the two lines approximately overlap. (a) Initial states and band populations obtained using the effective Hamiltonian $\hat{H}_{\mathrm{eff},0}$, which is without the J_x^2/ω correction term (cases 3 and 4). (b) Hamiltonian $\hat{H}_{\mathrm{eff},1}$ which is with the correction term (cases 1 and 2).

reason, up to 50 ms the center-of-mass position $x(t)$ exhibits roughly linear behavior with some additional oscillations. Interestingly, the anomalous drift $x(t)$ exhibits quadratic behavior on short time scales in all cases from Fig. 3.3. In Appendix E, we explain this feature using the time-dependent perturbation theory and Fermi's golden rule.

3.3 Interacting case

We now investigate the effects of weak repulsive interactions. We work in the high-frequency regime and set $\omega = 20$. As shown in Section 3.1.2, for $U = 0$ the effective Hamiltonian with correction, $\hat{H}_{\mathrm{eff},1}$, is in this case equivalent to the Harper-Hofstadter Hamiltonian with flux $\alpha = 1/4$. Moreover, the same approximative form of the full effective model accurately reproduces the behavior of the time-dependent Hamiltonian up to 50 ms and thus provides a good starting point for the study of weakly interacting particles. We first consider the anomalous drift of the center of mass of the atomic cloud and then we inspect the expansion dynamics more closely in terms of atomic density distributions in real and momentum space.

3.3.1 Anomalous drift and dynamics of band populations

To simulate the dynamics of many incoherent bosons, we use the classical field method presented in Section 3.1.3 and propagate Eq. (3.9) in time. We assume that at $t_0 = 0$ atoms are uniformly distributed over the lowest band of $\hat{H}_{\mathrm{eff},1}$. For this reason, the initial state is the same as the one that we use in the noninteracting regime. In this way, the dynamics is initiated by an effective triple quench: at $t_0 = 0$ the confining potential is turned off, atoms are exposed to the force $\mathbf{F} = -F\mathbf{e}_y$, and also the interactions between particles are introduced. The total number of particles is set to $N = 90,000$, which amounts to approximately 100 particles per lattice site in the central region of the atomic cloud. We consider only weak repulsion $U \leq 0.05$.

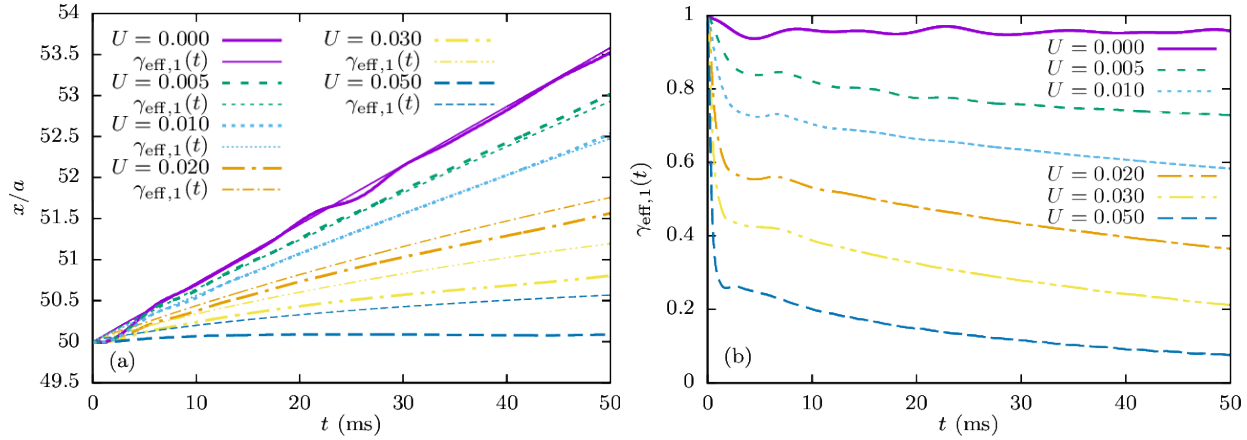

Figure 3.5: Effects of interactions. (a) Anomalous drift $x(t)$ for several different values of the interaction coefficient U. U is given in units where $J = 1$. Thick lines: numerical simulations using the time-dependent Hamiltonian $\hat{H}(t)$. Thin lines: theoretical prediction (3.13) from $\gamma_{\mathrm{eff},1}(t)$. (b) Corresponding $\gamma_{\mathrm{eff},1}(t) = \eta_1(t) - \eta_2(t) + \eta_3(t)$, obtained from simulations using the effective Hamiltonian $\hat{H}_{\mathrm{eff},1}$.

The anomalous drift $x(t)$ obtained using the full time-dependent Hamiltonian is shown in Fig. 3.5(a) for several different values of the interaction strength U. In comparison to the noninteracting regime, we find that the weak repulsive interactions inhibit the response of the center of mass to the external force. In particular, at $t = 50\,\mathrm{ms}$ the drift is reduced by about 15% for $U = 0.005$ and it is further lowered by an increase in U. Finally, at $U = 0.05$, the anomalous drift is barely discernible. Interestingly, for weak $U \in (0.001, 0.01)$ we find that the drift $x(t)$ in the range of $t \in (10, 50)\,\mathrm{ms}$ looks "more linear" as a function of time in comparison to the noninteracting result.

We now analyze the anomalous drift in terms of the filling factor $\gamma(t)$ and compare the results of Eq. (3.9) with the description based on Eq. (3.10). By solving Eq. (3.10) we obtain the filling factor $\gamma_{\mathrm{eff},1}(t)$ following Eq. (D.4) and present our results in Fig. 3.5(b). Whenever the results of Eq. (3.9) reasonably agree with the results obtained from Eq. (3.10), we are close to a steady-state regime with only small fluctuations in the total energy, as Eq. (3.10) preserves the total energy of the system. In this regime, during the expansion dynamics the interaction energy is converted into the kinetic energy and atoms are transferred to higher bands of the effective model. Consequently, the filling factor $\gamma_{\mathrm{eff},1}(t)$ is reduced. Typically, we find three different stages in the decrease of $\gamma_{\mathrm{eff},1}(t)$.

In an early stage, $t \leq t_1 = 5\,\mathrm{ms}$, a fast redistribution of particles over the bands of the effective model sets in due to the sudden quench of U. The factor $\gamma_{\mathrm{eff},1}(t)$ decays quadratically as a function of time down to $\gamma_{\mathrm{eff},1}(t_1) \approx 0.75$ for $U = 0.01$, and $\gamma_{\mathrm{eff},1}(t_1) \approx 0.25$ for $U = 0.05$. In this process the interaction energy of the system is quickly lowered as described in Appendix F. At later times $t > 5\,\mathrm{ms}$, we observe a linear decay of the filling factor $\gamma_{\mathrm{eff},1}(t)$ as a function of time, that finally turns into an exponential decay at even later times ($t > 10$ ms). Similar regimes are observed in other dynamical systems. For example, a decay rate of an initial state

suddenly coupled to a bath of additional degrees of freedom exhibits these three stages [195]. The initial quadratic decay is often denoted as "the Zeno regime." For longer propagation times, Fermi's golden rule predicts the linear decay. At even longer time scales, when the repopulation of the initial state is taken into account, the time-dependent perturbation theory yields the exponential regime, known under the name of the Wigner-Weisskopf theory [195].

We now investigate this last regime in more detail. For the population of the lowest band $\eta_1(t)$, an exponential decay function $f(t) = a + b\mathrm{e}^{-ct}$ provides high quality fits for $t \in (10, 50)$ ms; see Fig. 3.6(a) for an example. Similarly, the populations of two higher bands can also be fitted to exponential functions. The obtained exponential decay coefficients c for the lowest band population are plotted as a function of the interaction strength U in Fig. 3.6(b). The resulting dependence is approximately quadratic: $c(U) = \alpha_0 + \alpha_1\ U + \alpha_2\ U^2$. For small values of U, the exponents $c(U)$ obtained for the dynamics governed by $\hat{H}(t)$ and $\hat{H}_{\mathrm{eff},\,1}$ agree very well and exhibit linear behavior. At stronger interaction strengths $U \geq 0.03$, the approximation of Eq. (3.10) becomes less accurate as it omits the quadratic contribution in $c(U)$ found in the full time evolution. In addition, the values of the exponents c are affected by the force strength F and driving frequency ω.

As we now understand some basic features of $\gamma_{\mathrm{eff},1}(t)$, we make an explicit comparison between the numerical results for the anomalous drift and the expectation (3.13). The dashed lines in Fig. 3.5(a) correspond to the theoretical prediction (3.13) calculated from $\gamma_{\mathrm{eff},1}(t)$. For the intermediate interaction strengths $U \leq 0.01$, we find a very good agreement between the two. From this we conclude that the interaction-induced transitions of atoms to higher bands are the main cause of the reduced anomalous drift $x(t)$ as a function of U. When the interactions become strong enough ($U \sim 0.02$), the numerical results start to deviate from the theoretical prediction (3.13) with $\gamma_{\mathrm{eff},1}(t)$. In this regime, Eq. (3.10) does not provide a reliable description of the dynamics, as higher-order corrections need to be taken into account.

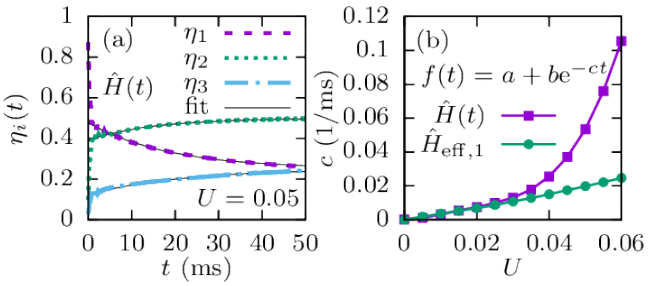

Figure 3.6: (a) Evolution of the band populations $\eta_i(t)$. Dashed lines: numerical results obtained using the time-dependent Hamiltonian $\hat{H}(t)$. Solid black lines: exponential fit using $f(t) = a + b\mathrm{e}^{-ct}$. The coefficient a was fixed to $a_1 = 0.25$, $a_2 = 0.50$ and $a_3 = 0.25$ for the first, second and third band respectively. (b) Dependence of the exponential decay coefficients for the lowest band population $\eta_1(t)$ on the interaction strength. U is given in units where $J = 1$.

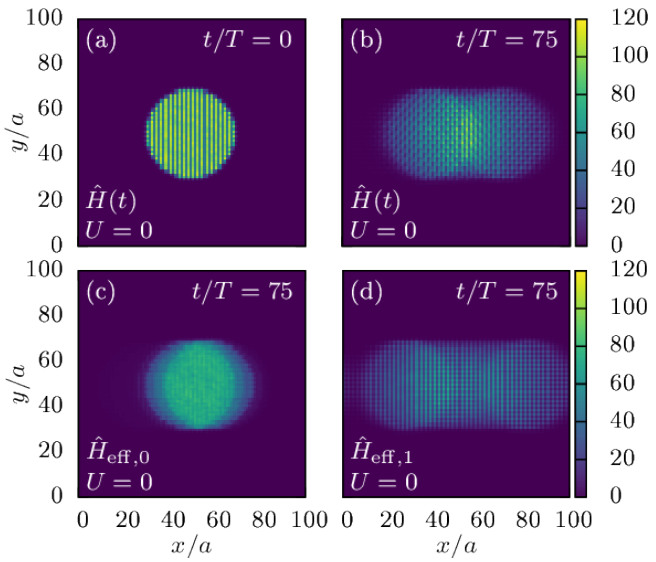

Figure 3.7: Real-space density distribution, noninteracting case $U = 0$. (a) Initial state. (b) After 50 ms (75 driving periods), evolution using the time-dependent Hamiltonian $\hat{H}(t)$. (c) Evolution using effective Hamiltonian without correction $\hat{H}_{\mathrm{eff},0}$. (d) Evolution using effective Hamiltonian with correction $\hat{H}_{\mathrm{eff},1}$.

3.3.2 Real and momentum-space dynamics

So far we have considered the averaged response of the whole atomic cloud. We now inspect the expansion dynamics in a spatially resolved manner. The real-space probability densities at the initial moment and after 50 ms (75 driving periods) are shown in Figs. 3.7 and 3.8, and the corresponding momentum-space probability densities in Appendix F.

At the initial moment, the atomic cloud is localized in the center of the lattice. By setting $r_0 = 20$ in the confining potential of Eq. (D.2) and populating the lowest-lying states, we fix the cloud radius to $r = 20$, Fig. 3.7(a). The cloud density is of the order of 100 atoms per lattice site and a weak density modulation is visible along x direction. After the confining potential is turned off, and the external force in the $-\mathbf{e}_y$ direction is turned on, the cloud starts to expand and move in the $+\mathbf{e}_x$ direction. As shown in the previous subsection, the band populations and therefore the anomalous drift are significantly altered by the interaction strength, and this is also the case with the expansion dynamics; see Figs. 3.7 and 3.8.

In the noninteracting case, Fig. 3.7(b), the atomic cloud nearly separates into two parts moving in opposite directions along x axes (while the center of mass still moves in the $+\mathbf{e}_x$ direction). By comparing Fig. 3.7(c) and Fig. 3.7(d), we conclude that this effect stems from the next-nearest-neighbor hopping along x present in the effective Hamiltonian (3.7), as it does not happen in the effective model without the correction term (3.6). This type of separation was already observed in Ref. [168], where the next-nearest-neighbor hopping terms were also present.

When the interactions between particles are included, this separation is not so prominent [Fig. 3.8(a), $U = 0.01$], and it almost completely disappears when the interactions are strong

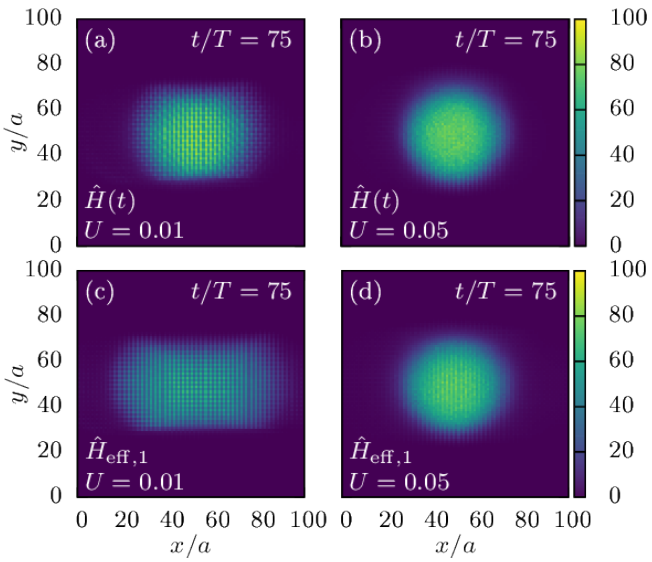

Figure 3.8: Real-space density distribution after 50 ms (75 driving periods), interacting case. U is given in units where $J = 1$. (a) Evolution using the time-dependent Hamiltonian $\hat{H}(t)$, $U = 0.01$. (b) Same with $U = 0.05$. (c) Evolution using the effective Hamiltonian $\hat{H}_{\text{eff},1}$, $U = 0.01$. (d) Same with $U = 0.05$.

enough [Fig. 3.8(b), $U = 0.05$]. This is also the case when the evolution is governed by the effective Hamiltonian $\hat{H}_{\text{eff},1}$; see Figs. 3.8(c) and 3.8(d). Atomic cloud widths $d_x = \sqrt{\langle x^2 \rangle - \langle x \rangle^2}$ during the expansion are plotted in Fig. 3.9. We observe a slow expansion of the cloud in y direction, Fig. 3.9(b), and much faster expansion along x direction, Fig. 3.9(a), which comes about as a consequence of the cloud separation. On top of this, we observe that the interactions enhance expansion along y. Surprisingly, the opposite is true for the dynamics along x. This counterintuitive effect is often labeled as self-trapping and its basic realization is known for the double-well potential [196, 197]. In brief, strong repulsive interactions can preserve the density imbalance between the two wells, as the system can not release an excess of the interaction energy. In our case, the situation is slightly more involved as the cloud splitting is inherent (induced by the corrections of the ideal effective Hamiltonian). Apart from this, due to the driving the total energy is not conserved. However, our numerical results indicate that the interaction energy is slowly released in the second expansion stage, Fig. F.1. Effectively, in this

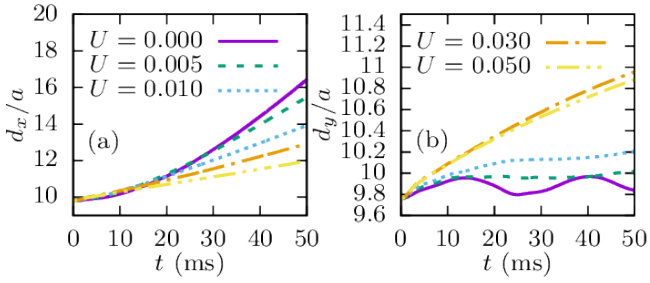

Figure 3.9: Atomic cloud width for different interaction strengths, evolution using the time-dependent Hamiltonian $\hat{H}(t)$. U is given in units where $J = 1$. (a) $d_x = \sqrt{\langle x^2 \rangle - \langle x \rangle^2}$. (b) $d_y = \sqrt{\langle y^2 \rangle - \langle y \rangle^2}$.

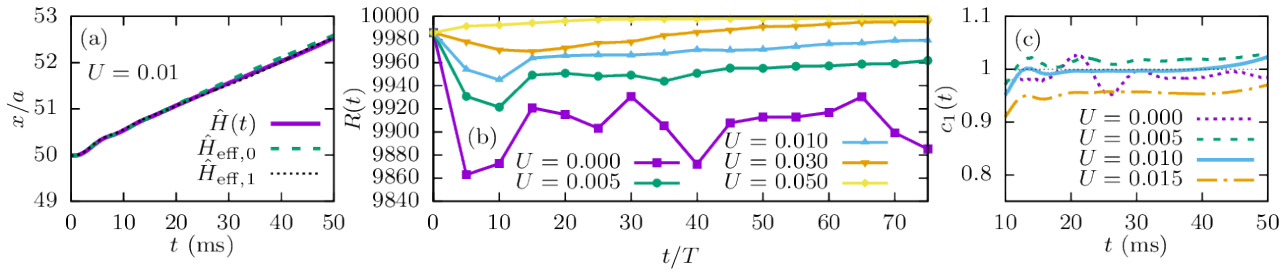

Figure 3.10: (a) Comparison of anomalous drifts obtained from evolution using the time-dependent Hamiltonian $\hat{H}(t)$ (solid purple line), effective Hamiltonian without correction $\hat{H}_{\text{eff},0}$ (dashed green line) and effective Hamiltonian with correction $\hat{H}_{\text{eff},1}$ (dotted black line). Intermediate interaction strength $U = 0.01$. U is given in units where $J = 1$. (b) Time evolution of the inverse participation ratio in momentum space for several different values of U. Evolution is performed using the time-dependent Hamiltonian $\hat{H}(t)$. When the interactions are strong enough, IPR approaches the maximal possible value (10,000 in this case), which is equal to the total number of states and corresponds to the completely delocalized state. U is given in units where $J = 1$. (c) Chern number of the lowest band obtained for different interaction strengths as the ratio of the theoretical prediction for the anomalous drift and numerical results: $c_1(t) = \left(\frac{2Fa^2}{\pi\hbar}\int_0^t \gamma_{\text{eff},1}(t')dt'\right) / \left(x(t) - x(t_0)\right)$.

way the interactions cancel out the contribution of the next-nearest-neighbor hopping and favor the measurement of the properties of the model (3.6). In Fig. 3.10(a) we show that deviations between different approximations based on $\hat{H}(t)$, $\hat{H}_{\text{eff, 1}}$, and $\hat{H}_{\text{eff, 0}}$ in the anomalous drift $x(t)$ nearly vanish at $U = 0.01$.

Another desirable effect might be that the interactions make the momentum-space probability density more homogeneous, see Appendix F, so that the real-space probability density becomes more localized. We can quantify momentum-space homogeneity using the inverse participation ratio $R(t) = \frac{1}{\sum_i P_i^2(t)}$, where $P_i(t) = |\psi_i(t)|^2$ is the probability that the state ψ_i is occupied at time t. Minimal value of the inverse participation ratio (IPR) is 1 and it corresponds to a completely localized state, while the maximal value is equal to the total number of states (in our case 10,000) and corresponds to the completely delocalized state, where the particles have the same probability of being at any quasimomentum $\mathbf{k}$. As stated before, the first Brillouin zone of the lowest band has to be as homogeneously populated as possible in order to properly measure the lowest band Chern number. From Fig. 3.10(b), we see that IPR increases in time when the interaction coefficient U is large enough, so we can conclude that the interactions are actually beneficial for measuring the Chern number, as they can "smooth-out" the momentum-space probability density. In Fig. 3.10(c) we give estimates for the Chern number that can be extracted from our numerical data for different values of U. We find the best estimate $c_1 \sim 0.99$ for the intermediate interaction strength $U \sim 0.01$.

3.3.3 Staggered detuning

Here we briefly consider the effects of staggered detuning that was introduced in the experimental study [70] during the loading and band mapping sequences. This detuning can be described by an additional term

$$\frac{\delta}{2}\sum_{l,m}\left[(-1)^l+(-1)^m\right]\hat{n}_{l,m} \tag{3.14}$$

in the Hamiltonians $\hat{H}(t)$ and $\hat{H}_{\mathrm{eff},1}$. We will ignore the higher-order [at most $\mathcal{O}\left(\frac{1}{\omega^2}\right)$] corrections that this term introduces to the effective Hamiltonian. Staggered detuning does not break the symmetry of the effective Hamiltonian $\hat{H}_{\mathrm{eff},1}$, but if δ is large enough, it can cause a topological phase transition and make all bands topologically trivial. By numerically calculating the Berry curvature and Chern numbers c_i', we find that this transition occurs at $\delta_c \approx 1.38\,J$; see Fig. 3.11. This value is lower than the one for the ordinary Harper-Hofstadter Hamiltonian for $\alpha = 1/4$, which is $\delta_c = 2\,J$ [70], due to the different hopping amplitudes J_x' and J_y', and due to the additional J_x^2/ω correction that we consider.

We now investigate how this topological transition can be probed through the dynamical protocol used in the experiment. We again numerically calculate the anomalous drift and the evolution of the filling factor, but now with staggered detuning (3.14) included in the Hamiltonian $\hat{H}_{\mathrm{initial}}$ (D.2) used to obtain the initial state, in the equations of motion (3.9) and (3.10), and in the definitions of the band populations $\eta_i(t)$ (D.4). Using these results, we repeat the procedure for the extraction of the lowest band Chern number from numerical data that was carried out in the previous section. The Chern number obtained by comparing the anomalous drift to the prediction calculated from the filling factor is then averaged over the time interval $t \in (20, 40)\,\mathrm{ms}$. This interval was chosen in order to avoid the initial quadratic regime and the finite-size effects at later times. The resulting lowest band Chern numbers for several different values of detuning δ in both the noninteracting case and the case of intermediate interaction strength $U = 0.01$ are presented in Fig 3.11.

We can see that the calculated value of the Chern number decreases from $c_1 = 1$ to $c_1 = 0$ with increasing detuning δ. The obtained value of the Chern number is lower than 1 even before the phase transition occurs. This is due to our choice of the initial state, which is not perfectly homogeneous in momentum space. Close to the phase transition, both the energy bands and the Berry curvature have pronounced peaks at the same regions of the first Brillouin zone, and these regions are initially less populated. Because of this, the Berry curvature at these regions contributes less to the anomalous drift, which lowers the measured Chern number. This effect is somewhat reduced by the interactions, as they smooth out the momentum-space probability density, and might also cancel out the detuning term. Similar interplay of interactions and staggering was observed in the fermionic Hofstadter-Hubbard model [198]. The obtained results are in line with experimental measurements [70].

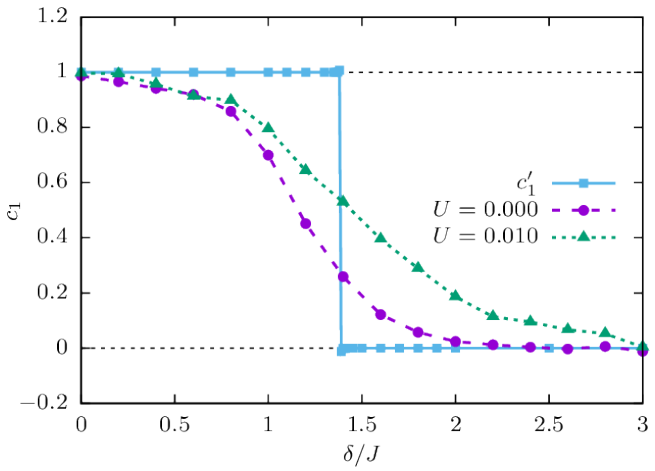

Figure 3.11: Lowest band Chern numbers extracted from numerical data for several different values of detuning δ. Purple circles: noninteracting case, $U = 0$. Green triangles: $U = 0.01$. Blue squares: Theoretical values of the lowest band Chern number c_1'. A topological phase transition is visible at $\delta_c \approx 1.38$. The lines between points are only a guide to the eye.

3.4 Conclusions

Motivated by the recent experimental results reporting the Chern numbers of topological bands in cold-atom setups, we studied numerically bosonic transport in a driven optical lattice. The considered driving scheme and the range of microscopic parameters were chosen to be close to those in a recent experimental study [70]. The driving frequency was set to be high enough in order to avoid strong energy absorption for the relevant time scales. Additionally, the system was restricted to a two-dimensional lattice, even though the actual experimental setup had continuous transverse degrees of freedom. This restriction stabilizes the system [172, 174, 184] and leads to lower heating rates than those in the experiment. It corresponds to the case of strongly confined third dimension.

We investigated bosonic dynamics for the full time-dependent Hamiltonian, the effective Floquet Hamiltonian, and included the effects of weak repulsive interactions between atoms using the mean-field approximation. In the noninteracting case, we found that the effective Hamiltonian and its band structure depend on the frequency of the drive ω through an additional J_x^2/ω correction term. The initial state was set as a mixture of incoherent bosons homogeneously populating the lowest band, but a possible direction of future research could be to simulate the full loading sequence of an initial Bose-Einstein condensate and to try to obtain the incoherent state through driving, as it was done in the experiment.

The main focus of this work is on the effects of weak interactions. For a weak atomic repulsion, atomic transitions to higher effective bands obtained in our simulations mainly occur due to a release of the initial interaction energy during the atomic-cloud expansion. Although the effect is undesirable, it can be properly taken into account in the extraction of the Chern number. At larger interaction strengths, the transitions are more pronounced as the system

absorbs energy from the drive. In this regime the good agreement between the full and effective description is lost and the measurement should become more complicated. In addition to causing redistribution of atoms over bands, our results show that weak interactions can also be beneficial in measuring the Chern number. Their desirable effect comes about due to smoothening the atomic distribution over the topological band and due to canceling out the contribution of some less relevant terms to the bosonic dynamics.

Chapter 4

Bosonic fractional quantum Hall states in driven optical lattices

Since early experiments with quantum gases, there has been a strong interest in the realization of fractional quantum Hall (FQH) states in these setups [199–213]. Despite numerous experimental achievements and a variety of theoretical proposals, FQH physics has still not been reached in cold-atom experiments. At first glance, both key requirements for the emergence of FQH states - atomic interactions and strong synthetic magnetic fields - are now experimentally available. However, there are several specific details in the implementation of strong synthetic magnetic fields for cold atoms that make the realization of FQH states still challenging.

The most advanced recent realizations of artificial gauge potentials exploit periodically driven optical lattices [70, 75, 77–80, 86, 87, 173, 214]. However, general arguments and numerical studies [94, 95, 215] suggest that the interplay of interactions and driving in a thermodynamically large system introduces heating, leading to a featureless infinite-temperature state in the long-time limit. Although this general result might sound discouraging, the heating process can be very slow in some driven systems for specific regime of microscopic parameters. There, the system can be described by a physically interesting "prethermal" Floquet state on experimentally relevant time-scales [96–98, 193, 194, 216, 217]. Moreover, the onset of thermalization in a finite-size interacting system may exhibit unexpected features, not found in the thermodynamic limit [218, 219]. Heating rates and resulting instabilities have been recently investigated both theoretically and experimentally for the driven Bose-Hubbard model in the weakly interacting regime [96, 174, 178, 179]. Moreover, experimental studies of the driven Fermi-Hubbard model in a honeycomb lattice have established a timescale of the order of 100 tunneling times for the regime where the effective-model description applies [124, 220].

In this Chapter, we consider small systems of several interacting bosonic atoms in a periodically driven optical lattice featuring synthetic magnetic flux. The focus of our study is on finding optimal microscopic parameters that would allow to prepare and probe the basic

bosonic Laughlin state in this setup. To this end, we employ exact numerical simulations of the driven Bose-Hubbard model [169] for small system sizes.

From one point of view, it is expected that a small driven system exhibits low heating rates for a driving frequency set above a finite bandwidth of an effective model [94]. However, driving a system with such a high frequency may lead to undesirable effects, such as coupling of the lowest band to higher bands of the underlying optical lattice, thus making the initial description based on the lowest-band Hubbard model inapplicable. These effects have been addressed in a recent study [88] where an optimal intermediate frequency window for Floquet engineering has been established.

In our study, we go a step further in the search for the optimal regime that might allow for the bosonic Laughlin states under driving. In particular, for a realistic, intermediate value of a driving frequency, the interaction term complicates the effective model by introducing several higher-order terms. Their effect on the topological states has been addressed only recently [221, 222] and it has been found that typically these terms work against the topological state. For this reason, the stability of the Laughlin state at intermediate driving frequency requires a separate study, that we perform here. Moreover, we numerically investigate an experimentally relevant preparation protocol for the Laughlin state in a driven system [183]. For a reference, we note that a simpler but closely related question concerning the static (undriven systems) has gained lot of attention [181, 202, 203, 211].

This Chapter is organized as follows: in Section 4.1 we introduce the model under study and briefly review key features of the particle-entanglement spectra that we will exploit in the identification of the Laughlin-like state. Then, in Section 4.2.1 we investigate general heating effects of interacting bosons exposed to the driving. By extending this approach, in Section 4.2.2 we construct the stroboscopic time-evolution operator and inspect its eigenstates in order to identify possible FQH states. Finally, in Section 4.3 we address the possibility of accessing these states in an experiment through a slow ramp of the driving term.

4.1 Model and method

In this section we first introduce the driven model and explain the basis of Floquet engineering. Then we summarize several key features of the particle-entanglement spectra that we use to characterize the bosonic Laughlin states.

4.1.1 Driven model

Properties of bosonic atoms in a deep optical lattice can be realistically described within the framework of the Bose-Hubbard model given by Eq. (1.1) [5]. We consider a basic driving scheme [169] that introduces a uniform, synthetic magnetic flux into a *square* optical lattice

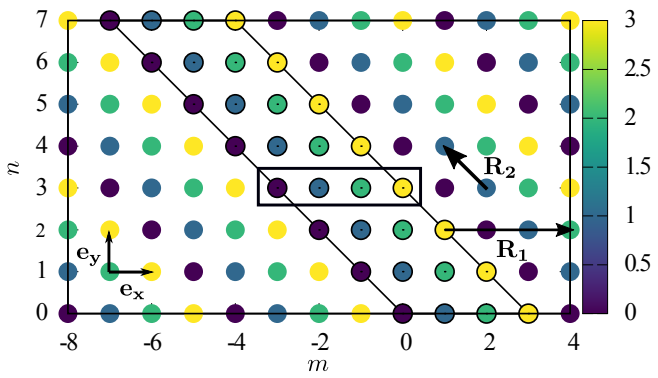

Figure 4.1: Lattice geometry used throughout this Chapter. The parallelogram gives the exemplary lattice size $(L_x, L_y) = (4, 8)$. The color scale is defined by $\mod(m+n, 4)$, in accordance with the driving term from Eq. (4.1). The vectors $\mathbf{R}_1 = 4\,\mathbf{e}_x, \mathbf{R}_2 = -\mathbf{e}_x + \mathbf{e}_y$ are used to implement periodic boundary conditions. The small rectangle gives the magnetic unit cell for the effective model in Eq. (4.2).

here spanned by the two vectors $\mathbf{e_x}$ and $\mathbf{e_y}$. The corresponding Hamiltonian is given by the driven Bose-Hubbard model

$$\begin{aligned}\hat{H}(t) &= -J_x \sum_{m,n} \left(\hat{a}^\dagger_{m+1,n}\hat{a}_{m,n} + \text{H. c.}\right) - J_y \sum_{m,n} \left(e^{i\omega t}\hat{a}^\dagger_{m,n+1}\hat{a}_{m,n} + \text{H. c.}\right) \\ &+ \frac{\kappa}{2}\sum_{m,n} \sin\left(\omega\, t - (m+n-1/2)\,\phi\right)\hat{n}_{m,n} + \frac{U}{2}\sum_{m,n}\hat{n}_{m,n}(\hat{n}_{m,n}-1), \end{aligned} \tag{4.1}$$

where operators $\hat{a}_{m,n}$ ($\hat{a}^\dagger_{m,n}$) annihilate (create) a boson at lattice position (m, n), and local density operators are $\hat{n}_{m,n} = \hat{a}^\dagger_{m,n}\hat{a}_{m,n}$. J_x and J_y are tunneling amplitudes and U is the on-site local repulsive interaction. We use the units where $\hbar = 1$ and the lattice constant $a = 1$. The driving scheme is defined by the driving frequency ω, the driving amplitude κ and by a phase ϕ. In the following we set $\phi = \pi/2$ and $\kappa/\omega = 0.5$. These values were recently used in an experimental realization of the Harper-Hofstadter model [70]. The derivation of this model is briefly reviewed in Appendix G. We assume periodic boundary conditions implemented using the vectors $\mathbf{R}_1 = 4\,\mathbf{e}_x, \mathbf{R}_2 = -\mathbf{e}_x + \mathbf{e}_y$, as presented in Fig. 4.1. This choice is compatible with the driving term and it allows us to exploit translational symmetry by working in the fixed quasimomentum basis.

Formally, by using the Floquet theory [81–83], it can be shown that the full time-evolution operator corresponding to this model is given by Eq. (1.9). The full-time evolution operator is periodic as well and consequently the (quasi)eigenenergies of the time-independent effective Hamiltonian $\hat{\mathcal{H}}_{\text{eff}}$ are defined up to modulo ω. Eq. (1.9) gives formal mapping of a periodically driven system to an effective model that captures the stroboscopic time evolution of the model. However, according to general analytical arguments and numerical insights, the corresponding effective model of a driven interacting many-body system in the thermodynamic limit exhibits nonphysical features [94, 95]. In particular, the system thermalizes and in the long-time limit its steady state is a featureless, infinite-temperature state, independent of the initial state.

Here we consider small samples of several bosonic atoms. Due to a finite spectrum bandwidth, we expect the high-frequency expansion to be relevant for a finite range of the driving frequency. Within these assumptions, the leading-order (in $1/\omega$) effective Hamiltonian is

$$\begin{aligned}\hat{H}_{\text{eff}} &= -J_x \sum_{m,n} \left(\hat{a}^\dagger_{m+1,n}\hat{a}_{m,n} + \text{H. c.}\right) - J'_y \sum_{m,n} \left(e^{i(m+n)\phi}\hat{a}^\dagger_{m,n+1}\hat{a}_{m,n} + \text{H. c.}\right) \\ &+ \frac{U}{2}\sum_{m,n} \hat{n}_{m,n}\left(\hat{n}_{m,n} - 1\right). \end{aligned} \tag{4.2}$$

The Hamiltonian (4.2) features complex hopping phases $e^{i(m+n)\phi}$ that result in a uniform synthetic magnetic flux ϕ per lattice plaquette. Due to the driving, the renormalized hopping amplitude along the y direction turns into

$$J'_y \equiv \frac{\kappa}{2\omega}\sin(\phi/2)\, J_y. \tag{4.3}$$

For the values $\phi = 2\pi\alpha$, where the flux density α is set to $\alpha = 1/4$, and $\kappa/\omega = 0.5$, the tunneling amplitude along y direction in the effective model is $J'_y \approx J_y \times 0.1768$.

In a certain regime of microscopic parameters, the ground state of the model defined in Eq. (4.2) is given by the lattice version of the Laughlin state [203, 205, 223–225]. The Laughlin state is stabilized for the filling factor $\nu = N_p/N_\phi = 1/2$, where $N_\phi = \alpha L_x \times L_y$ is the total number of fluxes (N_ϕ being an integer) and N_p is the number of bosons, and for a strong-enough repulsion U. Another important requirement for the Laughlin state is to avoid the strong hopping anisotropy and to keep $J_x \approx J'_y$, so we set $J_x = 0.2J_y$. We consider system sizes $N_p = 4, 5, 6$ and the respective lattices sizes $(L_x, L_y) = (4, 8), (4, 10)$, and $(4, 12)$, see Fig. 4.1, where we expect the ground state to correspond to the $\nu = 1/2$ Laughlin state. The Hilbert space sizes for $k_x = k_y = 0$ are $\dim \mathcal{H} = 6564, 108604$, and 1913364 respectively. For this choice of microscopic parameters, the model ground state of Eq. (4.2) is approximately twofold degenerate. The two ground-states are found in the sectors $k_x = 0, k_y = 0$ and $k_x = 0, k_y = \pi$. We denote them by $|\psi^{0,0}_{\text{LGH}}\rangle$ and $|\psi^{0,\pi}_{\text{LGH}}\rangle$.

As we are mainly interested in the driven regime, not only the ground state, but the full spectrum of the model from Eq. (4.2) plays a role. A rough argument is that the system does not absorb energy provided that the driving frequency ω is set above the bandwidth of the effective model. Several spectra of the model from Eq. (4.2) for $k_x = 0, k_y = 0$ are presented in Fig. 4.2(a). It can be seen that the ground-state energy is weakly affected by the value of $U \geq J_x$, while the top part of the spectrum with few states is found at $UN_p(N_p - 1)/2$. For higher values of U the spectrum splits into bands where the lowest band corresponds to the hard-core bosons and higher bands include double and higher occupancies.

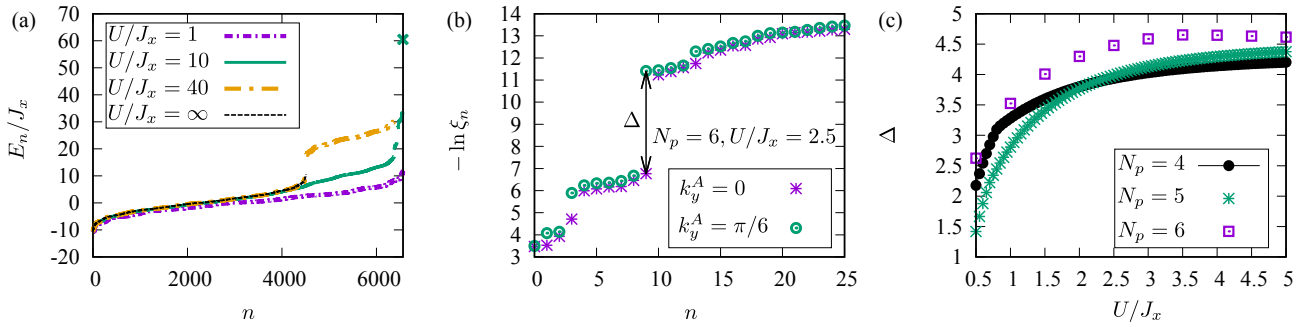

Figure 4.2: (a) The energy spectrum E_n of the model from Eq. (4.2) in the $k_x = 0, k_y = 0$ sector for $N_p = 4$ and different values of interaction $U/J_x = 1, 10, 40$ and $U/J_x = \infty$ (hard-core bosons). The top part of the spectrum is at $\approx (U/J_x)N_p\,(N_p - 1)\,/2$. (Not shown for $U/J_x = 40$.) For a high ratio U/J_x the spectrum splits into bands. The lowest band corresponds to hard-core bosons. (b) The low-lying part of the particle-entanglement spectrum $-\ln \xi_n$ of the ground-state incoherent superposition, Eq. (4.5), in the region A momentum sectors $k_y^A = 0$ and $k_y^A = \pi/6$, and for $N_p = 6, U/J_x = 2.5$. (c) The particle-entanglement gap Δ of the incoherent superposition Eq. (4.5) as a function of interaction strength U for $N_p = 4, 5, 6$.

4.1.2 Particle-entanglement spectra

There are several ways to characterize the ground states of the model from Eq. (4.2) as the Laughlin states. Usually, the starting point in this direction is the identification of the twofold degeneracy expected in the implemented torus geometry for $\nu = 1/2$. Another relevant quantity is the overlap of the numerically obtained state with the Laughlin analytical wave function in the torus geometry [205, 225]. More direct evidence can be obtained through the calculation of the relevant topological index (Chern number) or the quantized Hall conductance. An additional convincing approach, that we pursue here, is based on the analysis of the entanglement spectra of the relevant states.

In the following we will use the particle-entanglement spectrum (PES) [225, 226] to distinguish possible topologically nontrivial states. In order to obtain this type of entanglement spectrum, we partition N_p particles into two sets of N_A and $N_B = N_p - N_A$ particles. For a given mixed state ρ, we construct a reduced density matrix $\rho_A = \mathrm{tr}_B \rho$ by performing a partial trace over N_B particles. The resulting PES is given by $-\ln \xi_n$, where ξ_n are eigenvalues of ρ_A. The related particle-entanglement entropy is given by [227, 228]

$$S_A = -\mathrm{tr}\,(\rho_A \ln \rho_A)\,. \tag{4.4}$$

By partitioning particles, we keep the geometry of the system unchanged. For this reason, we will inspect the PES for the different momentum sectors k_y^A of the remaining N_A particles. An example of a PES is presented in Fig. 4.2(b). As proposed in Refs. [225, 226], we have considered the incoherent superposition of the almost twofold degenerate ground state of Eq. (4.2) as the

density matrix

$$\rho_{\mathrm{GS}} = \frac{1}{2}\left(|\psi^{0,0}_{\mathrm{LGH}}\rangle\langle\psi^{0,0}_{\mathrm{LGH}}| + |\psi^{0,\pi}_{\mathrm{LGH}}\rangle\langle\psi^{0,\pi}_{\mathrm{LGH}}|\right). \tag{4.5}$$

For simplicity, we only present the PES for the two momenta $k_y^A = 0$ and $k_y^A = \pi/6$. We observe a clear particle-entanglement gap Δ. In addition, the counting of low-lying modes below this gap (ten modes for $k_y^A = 0$ and nine modes for $k_y^A = \pi/6$, at $N_A = 3, N_p = 6$) corresponds to the Laughlin state [225, 226]. In this way the PES encodes topological features of the state ρ in the form of well defined number of excitations per momentum sector k_y^A [225, 226]. This type of analysis is useful as it can identify topological features even without model states, as done for the case of fractional Chern insulators [229, 230].

In the following we will consider specific particle partitions $N_A = 2, N_p = 4$; $N_A = 2, N_p = 5$; and $N_A = 3, N_p = 6$. For these cases the counting of excitations $\mathcal{N}_L(k_y^A)$ per momentum sector k_y^A is well established and given in Table 4.1. In Fig. 4.2(c) we show the particle-entanglement gap of the mixtures, Eq. (4.5), obtained at different values of U. Numerical results for the obtained PES indicate that a reasonably large gap is found starting at $U \sim 0.5J_x$ and the characteristic features of the Laughlin state persist with a further increase in U. We note that at lower values of the flux density, $\alpha < 1/4$, the Laughlin state can be found at even lower values of the repulsion U [205, 225].

Table 4.1: Counting of modes $\mathcal{N}_L\left(k_y^A\right)$ in the PES of the Laughlin state for several system sizes and particle partitions. The last column lists the $\mathcal{N}_L(k_y^A)$ values for each momentum sector $k_y^A = 2\pi i/L_y, i = 0, \ldots, L_y - 1$.

N_p	(L_x, L_y)	N_A	PES: $\mathcal{N}_L(k_y^A)$
4	$(4, 8)$	2	$3, 2, 3, 2, 3, 2, 3, 2$
5	$(4, 10)$	2	$4, 3, 4, 3, 4, 3, 4, 3, 4, 3$
6	$(4, 12)$	3	$10, 9, 9, 10, 9, 9, 10, 9, 9, 10, 9, 9$

By analyzing the effective model from Eq. (4.1), we have obtained a guidance for the regime of microscopic parameters and for the geometry of the small system that can give rise to Laughlin states. In the next sections our aim is to go beyond the effective model from Eq. (4.2) and to identify topological states supported by the full driven dynamics as captured by the model given in Eq. (4.1).

4.2 Driven dynamics

In this section we discuss the full driven dynamics as captured by the model given in Eq. (4.1).

4.2.1 Heating

First we address the onset of heating following the standard procedure discussed in Refs. [217, 231]. The initial state of the system is prepared using the ground state of the effective model

$$|\psi(t=0)\rangle = e^{-i\hat{K}(t=0)}|\psi^{0,0}_{\mathrm{LGH}}\rangle \tag{4.6}$$

and we monitor the stroboscopic time-evolution $t = N\,T$, $T \equiv 2\pi/\omega$ governed by the full driven model defined in Eq. (4.1). In our numerical simulations, we approximate the micromotion operator $\hat{K}(t=0)$ using the leading-order high-frequency expansion; see Eq. (G.12). The quantity of interest is the expectation value of the effective Hamiltonian: (4.2)

$$\langle \hat{H}_{\mathrm{eff}}(t=NT)\rangle_K = \langle\psi(t)|e^{-i\hat{K}(t=0)}\hat{H}_{\mathrm{eff}}e^{i\hat{K}(t=0)}|\psi(t)\rangle. \tag{4.7}$$

We expect this quantity to reasonably correspond to the ground-state energy of the effective model E_0 in the regime of very high frequency. On the other hand, for a "low" driving frequency we expect the system to quickly reach the infinite-temperature $\beta \to 0$ regime defined by

$$\lim_{\beta\to 0}\langle \hat{H}_{\mathrm{eff}}\rangle = \frac{1}{\dim\mathcal{H}}\mathrm{tr}\left(\hat{H}_{\mathrm{eff}}\right). \tag{4.8}$$

For this reason we monitor the normalized total energy

$$Q(t=NT) = \frac{\langle \hat{H}_{\mathrm{eff}}(t=NT)\rangle_K - E_0}{\lim_{\beta\to 0}\langle \hat{H}_{\mathrm{eff}}\rangle - E_0} \tag{4.9}$$

and we present it in Fig. 4.3(a), for $U/J_x = 10$. In agreement with the known results [231], we find that the thermalization is quick for both a "high" driving frequency $\omega/J_x \geq 20$ and for a "low" driving frequency $\omega/J_x \leq 10$. For the intermediate values of ω, the heating process is slow [231] and the total energy exhibits a slow exponential growth captured by $Q(t=NT) \approx 1 - b\exp(-c\,t), t \gg 1$. An example of this behavior is given for $\omega/J_x = 15$ in Fig. 4.3(a). The heating process can also be monitored through the particle-entanglement entropy S_A as a function of time. In Fig. 4.3(b) for $N_p = 5$ and low driving frequency we find that this quantity quickly saturates to its maximal value. Indeed, for a thermal state at infinite temperature, S_A is given by

$$S_A^{\max} \approx \ln\binom{L_x\,L_y + N^A - 1}{N^A}, \tag{4.10}$$

marked by the horizontal, dot-dashed line in Fig. 4.3(b). Except for the highest frequency considered ($\omega/J_x = 50$), we find that, in the process of heating, the particle-entanglement gap of the initial state quickly closes (not shown in the plots).

Here we briefly discuss finite-size effects by comparing numerical results for the normalized

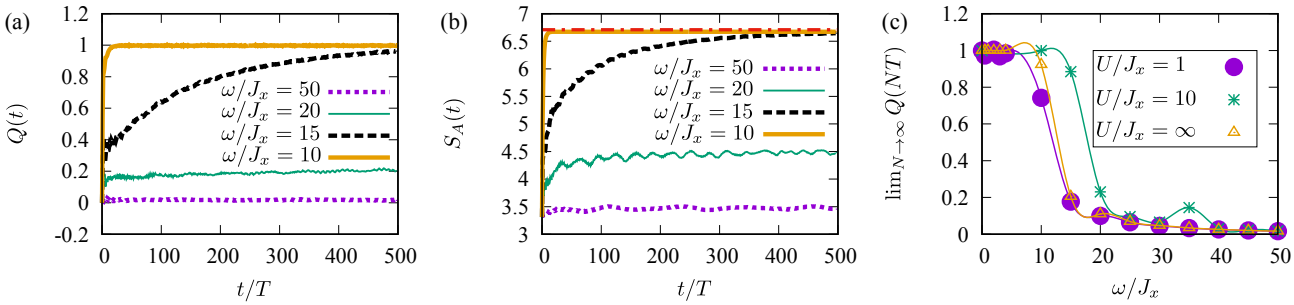

Figure 4.3: (a) The normalized total energy $Q(t = NT)$ from Eq. (4.9), and the (b) particle-entanglement entropy $S_A(t = NT)$, Eq. (4.4), during the time evolution governed by Eq. (4.1) for several driving frequencies $\omega/J_x = 50, 20, 15, 10$. Parameters: $N_p = 5, U/J_x = 10$. Note that the asymptotic value of S_A for $\omega/J_x = 10$ and $\omega/J_x = 15$ matches the one given in Eq. (4.10), as presented by the horizontal, dot-dashed line. (c) The long-time limit $\lim_{N\to\infty} Q(NT)$ for $N_p = 4$ and the on-site interactions $U/J_x = 1, 10$ and $U/J_x = \infty$ (hard-core bosons). The lines are only guides to the eye.

total energy for $N_p = 4$, $N_p = 5$, and $N_p = 6$. In line with the known results [94–96], the "high-frequency" regime with low heating rates moves toward higher ω as the system size increases. However, we find that the estimates obtained in this section ($\omega/J_x \geq 20$ for the high- and $\omega/J_x \leq 10$ for the low-frequency regime, for $U/J_x = 10$) apply to all the three sizes $N_p = 4, 5, 6$, at least for the time-scales that we consider. A comprehensive study of the leading finite-size effects in driven systems can be found in Refs. [94, 217, 231].

4.2.2 The stroboscopic time-evolution operator

In order to better understand the limitations of the effective model, here we time evolve all relevant basis states for a single driving period $T = 2\pi/\omega$ and construct the stroboscopic time-evolution operator

$$\hat{U}_F \equiv \hat{U}(t_0 + T, t_0 = 0) \tag{4.11}$$

such that $\hat{U}(NT+t_0) = \hat{U}_F^N$. In the next step, for a system size $N_p = 4$, $(L_x, L_y) = (4, 8)$ we fully diagonalize this operator and inspect its eigenstates $|n\rangle$. Following the described procedure, we obtain the long-time limit

$$\lim_{N\to\infty} \langle \hat{H}_{\text{eff}}(NT)\rangle_K = \sum_n |\langle n|\psi(t=0)\rangle|^2 \langle n|\hat{H}_{\text{eff}}|n\rangle_K \tag{4.12}$$

where we define

$$\langle n|\hat{H}_{\text{eff}}|n\rangle_K = \langle n|e^{-i\hat{K}(t=0)}\hat{H}_{\text{eff}}e^{i\hat{K}(t=0)}|n\rangle. \tag{4.13}$$

Results for $Q(t = NT)$ from Eq. (4.9) obtained in this way are summarized in Fig. 4.3(c), where we make a comparison between the long-time energies for the case of hard-core bosons ($U \to \infty$) and soft-core bosons (finite values of U). The obtained results indicate that heating rates of hard-core bosons are closer to the case of $U/J_x = 1$ in comparison to $U/J_x = 10$,

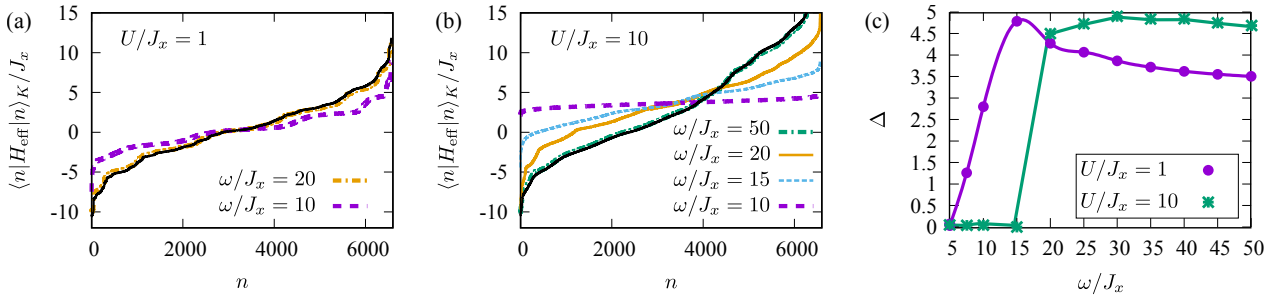

Figure 4.4: Properties of the eigenstates $|n\rangle$ of the stroboscopic time-evolution operator $\hat{U}_F$, Eq. (4.11), in the $k_x = 0, k_y = 0$ sector for $N_p = 4$. Expectation values $\langle n|\hat{H}_{\rm eff}|n\rangle_K$ defined in Eq. (4.13) for (a) $U/J_x = 1$, $\omega/J_x = 10, 20$ and (b) $U/J_x = 10$, $\omega/J_x = 10, 15, 20, 50$. The black solid lines mark eigenenergies of $\hat{H}_{\rm eff}$, Eq. (4.2). Note that in (b) we do not include few states from the top of the spectrum of $\hat{H}_{\rm eff}$, Eq. (4.2), for clarity. (c) The particle-entanglement gap Δ of the incoherent superposition ρ_F, Eq. (4.14), for $U/J_x = 1$ and $U/J_x = 10$, $N_p = 4$. The lines are only guides to the eye.

which is expected from the bandwidths shown in Fig. 4.2(a). Overall we observe that the "high-frequency regime" is wider for lower ratios U/J_x.

In Fig. 4.4, we make a comparison between the exact driven model captured by $\hat{U}_F$ and $\hat{H}_{\rm eff}$. In Figs. 4.4(a) and 4.4(b) we inspect the distribution of expectation values $\langle n|\hat{H}_{\rm eff}|n\rangle_K$. By comparing these values to the eigenenergies of the effective model, Eq. (4.2), we get an insight into the pertinence of the effective description [94, 95]. In particular, for an interacting system in the thermodynamic limit, the distribution is flat and the effective description is useless. We state again that we consider only small atomic samples. For this reason, it is expected that for high values of ω the full stroboscopic description nicely matches to the effective model values. Such an example is given in Fig. 4.4(a) for $U/J_x = 1$ and $\omega/J_x = 20$. As the value of ω gets lower the distribution becomes flatter, as can be seen in Fig. 4.4(b) for $U/J_x = 10$ by comparing results for $\omega/J_x = 50$ and $\omega/J_x = 10$.

The intermediate regime of frequencies, e. g., $\omega/J_x = 20$ for $U/J_x = 10$, is of the main experimental relevance [88]. We now investigate whether the driven stroboscopic dynamics supports some Laughlin-like states, by calculating the PES of the mixture

$$\rho_F = \frac{1}{2}\Big(|n_0(0,0)\rangle\langle n_0(0,0)| + |n_0(0,\pi)\rangle\langle n_0(0,\pi)|\Big) \tag{4.14}$$

where $|n_0(k_x, k_y)\rangle$ is the state from the k_x, k_y sector with the lowest expectation value $\langle n|\hat{H}_{\rm eff}|n\rangle_K$. The results are presented in Fig. 4.4(c). We find that the states with a well defined gap and the Laughlin-like PES can be found down to $\omega/J_x \geq 10$ for $U/J_x = 1$, and down to $\omega/J_x \geq 20$ for $U/J_x = 10$. Having established existence of these states for small samples of $N_p = 4$ particles, in the next section we discuss dynamical protocol which can be exploited to prepare these states.

4.3 Slow ramp

The question about an optimal adiabatic protocol that can be used to prepare the Laughlin state in a cold-atom setup has gained lot of attention [181, 202, 203, 211]. The situation becomes even more complex once the full driving process is taken into account. A general wisdom is that, by starting from a topologically trivial state, the topological index of a thermodynamically large system cannot be changed adiabatically. We consider a small atomic sample and follow the proposal of Ref. [211]. Our main contribution is that we extend this protocol to the case of the driven, interacting Bose-Hubbard model.

4.3.1 Model

Following results of Ref. [211], we consider a slow ramp of the tunneling amplitude along y direction, $J_y(t)$, as well as a slow ramp of the driving amplitude $\kappa(t)$. Namely, we start from a series of decoupled wires along the x direction and start coupling them. More precisely, initial states are selected as the ground states of $\hat{H}_{\rm ini}$:

$$\hat{H}_{\rm ini} = -J_x \sum_{m,n} \left(\hat{a}^\dagger_{m+1,n} \hat{a}_{m,n} + \text{H. c.} \right) + \frac{U}{2} \sum_{m,n} \hat{n}_{m,n} (\hat{n}_{m,n} - 1). \tag{4.15}$$

For the filling factors that we consider, the ground states of the $\hat{H}_{\rm ini}$ are simple noninteracting states with the ground state energy $E_{0,\rm ini} = -2J_x N_p$. Out of the several degenerate ground states, we select those where atoms occupy every second wire. There are two such states and we label them as $|\psi_+\rangle$ (even wires occupied) and $|\psi_-\rangle$ (odd wires occupied). These states have finite projections only onto the sectors $k_x = 0, k_y = 0$ and $k_x = 0, k_y = \pi$ of the driven model from Eq. (4.1). Therefore we may expect the two initial states $|\psi_\pm(t=0)\rangle$ to be transformed into the two Laughlin states during the ramp.

Having prepared the initial state, we slowly restore the tunneling amplitude along the y direction, $J_y(t)$, and slowly ramp up the driving amplitude $\kappa(t)$. The time-evolution is governed by

$$\begin{aligned} \hat{H}_{\rm sr}(t) &= -J_x \sum_{m,n} \left(\hat{a}^\dagger_{m+1,n} \hat{a}_{m,n} + \text{H. c.} \right) - J_y(t) \sum_{m,n} \left(e^{i\omega t} \hat{a}^\dagger_{m,n+1} \hat{a}_{m,n} + \text{H. c.} \right) \\ &+ \frac{\kappa(t)}{2} \sum_{m,n} \sin\left(\omega t - (m+n-1/2)\,\phi\right) \hat{n}_{m,n} + \frac{U}{2} \sum_{m,n} \hat{n}_{m,n} (\hat{n}_{m,n} - 1), \end{aligned} \tag{4.16}$$

where $J_y(t) = J_y \tanh(\eta\, t)$, $\kappa(t) = \kappa \tanh(\eta\, t)$, η being the ramping rate. In the long-time limit, we recover the original Hamiltonian from Eq. (4.1). During the ensuing time evolution we

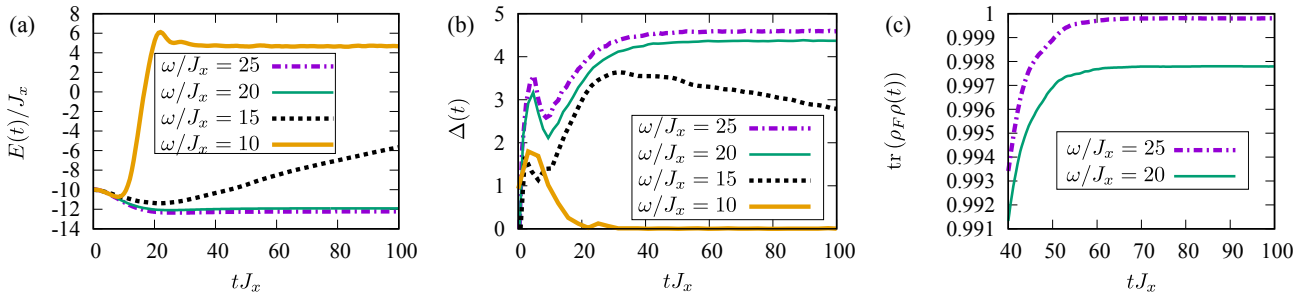

Figure 4.5: (a) The expectation value $E(t)$ defined in Eq. (4.18) and (b) the particle-entanglement gap $\Delta(t)$ of $\rho(t)$, Eq. (4.17), during the time evolution governed by Eq. (4.16) for several driving frequencies $\omega/J_x = 25,\ 20,\ 15,\ 10$. Parameters: $N_p = 5, U/J_x = 10, \eta/J_x = 0.05$. (c) The overlap $\mathrm{tr}\,(\rho(t)\rho_F)$ of the time evolved state with the target eigenstates of $\hat{U}_F$ for $\omega/J_x = 25,\ 20$. Parameters: $N_p = 4, U/J_x = 10, \eta/J_x = 0.05$.

construct the mixture

$$\rho(t) = \frac{1}{2}\Big(|\psi_+(t)\rangle\langle\psi_+(t)| + |\psi_-(t)\rangle\langle\psi_-(t)|\Big). \tag{4.17}$$

We monitor stroboscopically the energy expectation value

$$E(t) = \mathrm{tr}\left(\rho(t)\hat{H}_{\mathrm{eff}}\right) \tag{4.18}$$

and the PES of $\rho(t)$.

4.3.2 Results

In Fig. 4.5(a) we present the energy expectation value from Eq. (4.18) for $U/J_x = 10$ and several driving frequencies $\omega/J_x = 25,\ 20,\ 15,\ 10$. Our numerical results indicate that ramps with the rates up to $\eta/J_x \sim 0.1$ work reasonably well. Slower ramps give better results, but are less practical [211]. By construction, the initial state is a noninteracting state with particles delocalized along the x direction and therefore the initial energy is $E(t = 0) = -2\,N_p\,J_x$. During the ramp with the rate $\eta/J_x = 0.05$, for the regime of high driving frequencies, down to approximately $\omega/J_x = 20$, we find that the energy initially decreases and reaches an almost constant value at around $tJ_x \sim 20$. On the other hand, for $\omega/J_x = 15$, the system slowly heats up during the ramping process, and for $\omega/J_x = 10$ the system quickly reaches the infinite-temperature state.

One of our main results is summarized in Fig. 4.5(b), where we plot the particle-entanglement gap of $\rho(t)$, from Eq. (4.17), as a function of time. In the high-frequency regime $\omega/J_x \geq 20$, starting around $tJ_x \sim 20$ we find a persistent particle-entanglement gap, marking the onset of a topologically nontrivial state. It is even more interesting that, even for $\omega/J_x \sim 15$, the state seems to exhibit a finite gap on intermediate time-scales. This is not the case for $\omega/J_x \leq 10$, where the gap quickly vanishes. In Fig. 4.5(c), we present the value of the overlap $\mathrm{tr}\,(\rho(t)\rho_F)$,

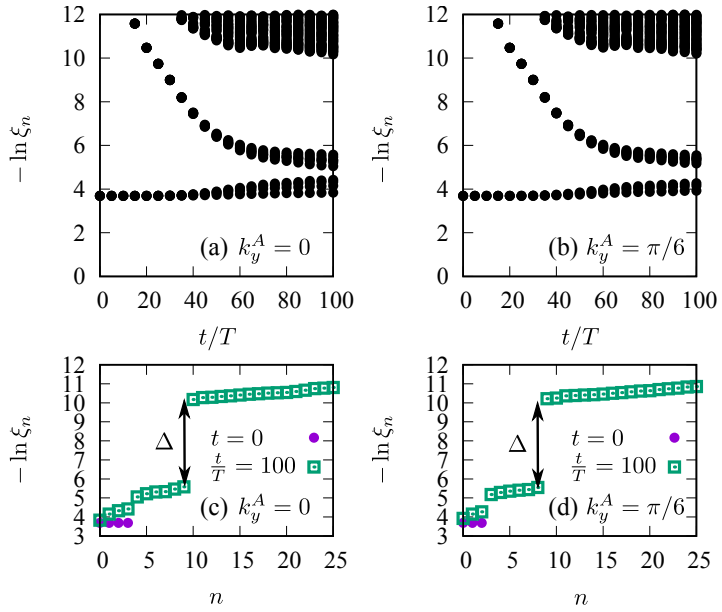

Figure 4.6: The low-lying part of the particle-entanglement spectra $-\ln \xi_n$ of $\rho(t)$, Eq. (4.17), during the time evolution governed by Eq. (4.16) in the (a) $k_y^A = 0$ and (b) $k_y^A = \pi/6$ momentum sectors. The low-lying part of the PES in the sectors (c) $k_y^A = 0$ and (d) $k_y^A = \pi/6$, at two instances of time $t = 0$ and $t/T = 100$. Parameters: $N_p = 6, U/J_x = 5, \omega/J_x = 15, \eta/J_x = 0.05$.

of the time-evolved mixed state with the relevant state from Eq. (4.14) for $N_p = 4$. Clearly, the slow ramp of the type given in Eq. (4.16) allows for the preparation of the relevant eigenstates of $\hat{U}_F$ with high fidelity (better than 1%).

In Figs. 4.6(a) and 4.6(b) we show the time evolution of the PES in the two momentum sectors $k_y^A = 0$ and $k_y^A = \pi/6$ for $N_p = 6$, $U/J_x = 5$, and $\eta/J_x = 0.05$. The PES of the initial state is easy to understand. As the $L_y/2$ wires are occupied by single atoms, the reduced density matrix is proportional to the identity matrix with the proportionality factor yielding $-\ln \xi_n = \ln\left(2\binom{Ly/2}{N_A}\right) \approx 3.69$. During the ramp we find that additional modes in PES are gaining weight and moving down in the spectrum. Finally, the state $\rho(t)$ reached around $t \approx 50T$ exhibits a well defined gap and the correct counting of the low-lying modes: there are ten low-lying modes for $k_y^A = 0$ and nine low-lying modes for $k_y^A = \pi/6$; see Figs. 4.6(c) and 4.6(d) and also Table 4.1.

In Fig. 4.7 we discuss a satisfactory range of ramping rates η for a given interaction strength U and a given driving frequency ω that we fix at $\omega/J_x = 15$. The obtained numerical results suggest that at weaker interaction strengths $U/J_x \leq 2$, slower ramping rates are needed. One way to explain this behavior is by using the effective model and arguing that the gap protecting the Laughlin state is smaller at weaker U. On the other hand, for stronger interaction strengths $U/J_x \geq 8$ the particle-entanglement gap closes at later stages as the heating process becomes dominant. Finally, in the intermediate range $U/J_x \sim 5$, faster ramps with $\eta/J_x = 0.1$ lead to the sought-after state $\rho(t)$ from Eq. (4.17), with persistent features in the PES up to $t = 500T$. These results indicate that, when optimizing the ramping protocol in an actual experiment,

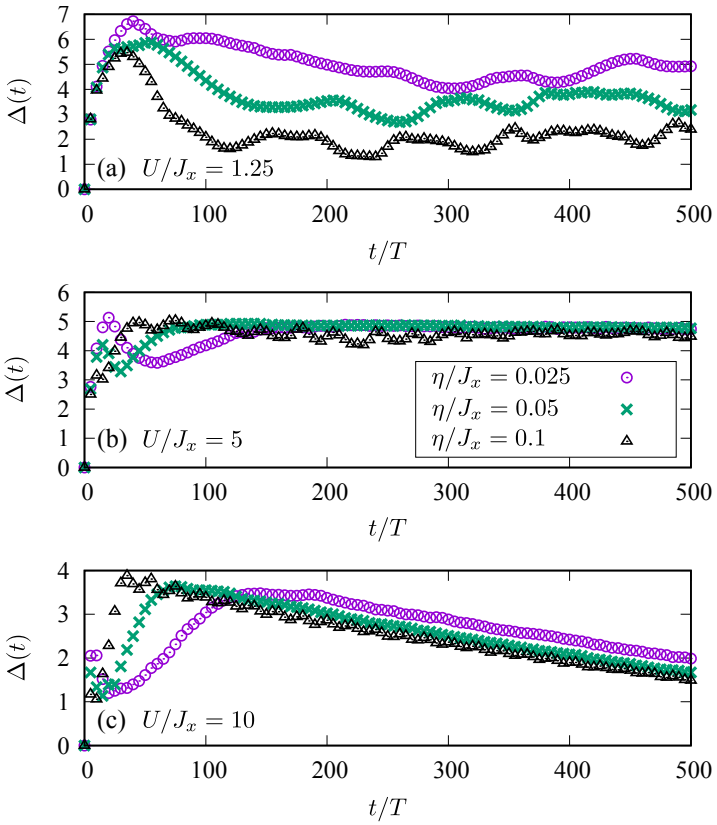

Figure 4.7: The particle-entanglement gap $\Delta(t)$ as a function of time during the time evolution governed by Eq. (4.16), for several interaction strengths (a) $U/J_x = 1.25$ (b) $U/J_x = 5$ and (c) $U/J_x = 10$, and several ramping rates $\eta/J_x = 0.025, 0.05, 0.1$. Other parameters: $N_p = 5, \omega/J_x = 15$.

there will be a tradeoff between the unfavorable heating and a faster ramping into the desired state, as both of these processes are promoted by interactions.

4.4 Conclusions

The technique of Floquet engineering has been successfully exploited for the implementation of synthetic magnetic fields in driven optical lattices. Following up on these achievements and on a long-standing pursuit for the FQH states in cold-atom setups, in this Chapter we have addressed possible realization of the bosonic Laughlin state in a small atomic sample in a periodically driven optical lattice. While a thermodynamically large interacting system generally heats up into an infinite-temperature state under driving, the heating process can be controlled to some extent in a few-particle system.

We have assumed a realistic driving protocol and finite on-site interactions, and we have identified the FQH state based on analysis of its particle-entanglement spectra. Results of our numerical simulations show that the stroboscopic dynamics of $N_p = 4, 5, 6$ particles supports the topological $\nu = 1/2$ Laughlin state down to $\omega/J_x = 20$ for $U/J_x = 10$, and down to $\omega/J_x = 15$ for $U/J_x = 1$, for the driving amplitude $\kappa/\omega = 0.5$. These results are in reasonable

agreement with the recent estimates of the optimal heating times [88] that take into account the contribution of the higher bands of the underlying optical lattice. In addition, we have investigated slow ramping of the driving term and found that it allows for the preparation of the Laughlin state on experimentally realistic time-scales of the order of $20\,\hbar/J_x$, where $\hbar/J_x$ is the tunneling time. Interestingly, we find that some topological features persist during an intermediate stage even in the regime where the system exhibits a slow transition into the infinite-temperature state (e. g., $\omega/J_x = 15$ for $U/J_x = 10$).

In the future, we plan to address the preparation scheme for the relevant correlated states in a driven honeycomb lattice, which exhibits lower heating rates in comparison to a cubic lattice according to the recent experiments [124, 220]. Another highly relevant question, that we have not tackled and that we postpone to future investigation, concerns suitable experimental probes of topological features. The recent progress in the field has led to the development of several detection protocols specially suited for the cold-atom systems [167, 168, 232–235]. For the type of systems considered in this Chapter, the most promising are results of the recent study [235] showing that fractional excitations can be probed even in small systems of several bosons.

Chapter 5

Conclusions

The study of ultracold quantum gases is an important topic in modern physics. The possibility of using ultracold atoms to build versatile quantum simulators is especially promising. These are highly-controllable macroscopic many-particle systems that obey the laws of quantum mechanics and can be used to simulate and study other complex quantum systems, such as those relevant for condensed-matter physics.

Quantum many-body scars have recently been introduced as new paradigm of weak ergodicity breaking in interacting quantum systems. This phenomenon has been first observed in the form of persistent oscillations in the quench dynamics probed in experiments on a Rydberg atom quantum simulator [46]. As a weak form of ergodicity breaking, many-body scars are believed to constitute a new universality class of systems that are distinct from other types of strong ergodicity breaking, such as in integrable models and many-body localized systems. Currently, major efforts are under way to understand the origins of quantum many-body scars. Similar properties have been found in other physical systems, including lattice gauge theories and topological phases of matter.

In Chapter 2 we proposed a realization of quantum many-body scars in a one-dimensional bosonic lattice with kinetically-constrained hopping. This model could be experimentally realized in ultracold atoms under a suitable Floquet engineering scheme. An important open question in this field was the necessity of hard kinetic constraints for the realization of scars. The standard "PXP" model of Rydberg atoms exhibits hard kinetic constraints, while some theoretical works on certain spin models suggested that constraints may not be necessary. Our bosonic models with density-dependent hopping provided a way to tunably control the kinetic constraints and study both limits on an equal footing. Using this approach we demonstrated that scars can occur in the absence of hard kinetic constraints. Another open problem was the relation between scars and integrability, following the observation that certain perturbations can enhance scarring while at the same time making the system non-ergodic. From this point

of view, our bosonic models are important because they demonstrate the presence of scars in a robustly non-integrable regime. Finally, our work points to an experimental platform that could realize quantum many-body scars and potentially allow new probes of this complex phenomenon. To this day there is only a single experiment on a system of Rydberg atoms, in contrast to the wealth of theoretical results. Given the large body of work on bosonic ultracold atoms and the variety of available experimental probes, such systems are the prime candidates for further experimental progress on many-body scars.

The effects of both strong local and long-range interactions have been studied in recent cold-atom experiments, as they can lead to rich phase diagrams. In order to observe topological phases of matter, the effects of magnetic field were also included in some recent experiments. Using periodic driving, synthetic magnetic fields have been experimentally realized in cold-atom systems, which has enabled the realization of seminal condensed-matter models such as the Harper-Hofstedter and Haldane model in cold-atom setups. However the interplay of driving and interactions introduces heating that may preclude the study of relevant topological states. A possibility of finding optimized parameter regimes with slow heating rates is still open and it was the main research topic in the second part of this thesis. These results could contribute to implementing new, even more advanced simulations, which could reveal new quantum phases.

The recent Chern-number measurement [70] was a milestone marking a realization of a topological band in a cold-atom setup. Motivated by the this experiment, in Chapter 3 we investigated the response of incoherent bosons to an external force in driven optical lattices featuring topological bands. The focus of this study was on the role of weak atomic interactions. Using numerical simulations based on a classical-field method, we found that interactions contribute to atomic transitions between different bands, thus complicating the experimental procedure in line with expectations. However, it was also shown that the weak atomic repulsion makes the Chern-number measurement easier in several ways. As this experimental approach is expected to become a routine tool in the near future, a first step in the preparation of more interesting topological phases, the so-far obtained results on the effects of weak interactions are of relevance for the future experiments.

Nowadays, cold-atom setups provide access to both strong synthetic magnetic fields and strong interactions. These ingredients are in principle enough to realize fractional Hall states and address their excitations. The complexity arises when using the driving protocol in the strongly interacting regime, due to heating. A solution for this problem would be to find some optimal parameter regime where the system stays in the prethermalized state for long enough time. At the moment, the possibility of finding fractional quantum Hall states in cold-atom setups is still open and the questions about how to prepare and manipulate these states using cold atoms prompt further theoretical studies. Our work on the stability and lifetime of bosonic fractional quantum Hall states presented in Chapter 4 should provide guidelines in this direction. In our study we took into account important experimental features, such as

a realistic driving scheme and finite on-site interactions. We used the particle-entanglement spectra in order to confirm that the state prepared in our driven model for a high enough driving frequency is indeed a bosonic Laughlin state. By performing numerical simulations, we identified an optimal regime of microscopic parameters for the preparation of these interesting strongly correlated states.

There are many possibilities to further extend the research presented in this thesis. Potential directions of future research are discussed at the ends of Chapters 2-4. It would be particularly exciting to explore whether it is possible to realize quantum many-body scars in topologically-nontrivial driven systems, as this would be a way to slow down the thermalization and increase the lifetimes of interesting topological states.

Appendix A

Relative magnitude of the hopping coefficients

Constraints are not the only factor that slows down the dynamics and leads to weakly-entangled eigenstates in spectrum of the Hamiltonian $\hat{H}_1$ (2.1) from Chapter 2. The relative magnitude of the hopping coefficients between different configurations mapped to each other under the action of the Hamiltonian also has important effects. In order to show this, we introduce two additional Hamiltonians

$$\hat{H}_{1a} = -J \sum_j \left(\hat{b}_j^\dagger \hat{b}_{j+1} \hat{n}_j^2 + \hat{n}_{j-1}^2 \hat{b}_j^\dagger \hat{b}_{j-1} \right), \tag{A.1}$$

$$\hat{H}_{1b} = -J \sum_j \left(\hat{b}_j^\dagger \hat{b}_{j+1} (1 - \delta_{n_j,0}) + (1 - \delta_{n_{j-1},0}) \hat{b}_j^\dagger \hat{b}_{j-1} \right). \tag{A.2}$$

These two Hamiltonians have the same constraints as the Hamiltonian $\hat{H}_1$ and therefore the same graphs as in Fig. 2.1. However, the particle number operators $\hat{n}_j$ are squared in $\hat{H}_{1a}$ and replaced with delta functions $(1 - \delta_{n_j,0})$ in $\hat{H}_{1b}$. This makes the minimal and extended clusters even less connected to the rest of the configurations in the case of $\hat{H}_{1a}$ and more connected in the case of $\hat{H}_{1b}$.

As anticipated, the revivals become more prominent for $\hat{H}_{1a}$, with fidelity peaks reaching more than 95%, while the peaks almost disappear for $\hat{H}_{1b}$, as illustrated in Fig. A.1(a). In addition, the entanglement entropy quickly saturates in the case $\hat{H}_{1b}$, while the growth is significantly suppressed in the case of $\hat{H}_{1a}$, as can be observed in Fig. A.1(b). The distribution of entanglement entropy across all eigenstates is also affected by the change of coefficients (not shown). $\hat{H}_{1a}$ has a spectrum with many low-entropy eigenstates, while the spectrum of $\hat{H}_{1b}$ is almost thermal and resembles that of $\hat{H}_2$. The probability distribution of consecutive gaps in the energy spectrum of $\hat{H}_{1a}$ is close to the Poisson distribution, which implies that $\hat{H}_{1a}$ is almost integrable. On the other hand, the distribution for $\hat{H}_{1b}$ is Wigner-Dyson, like in $\hat{H}_1$.

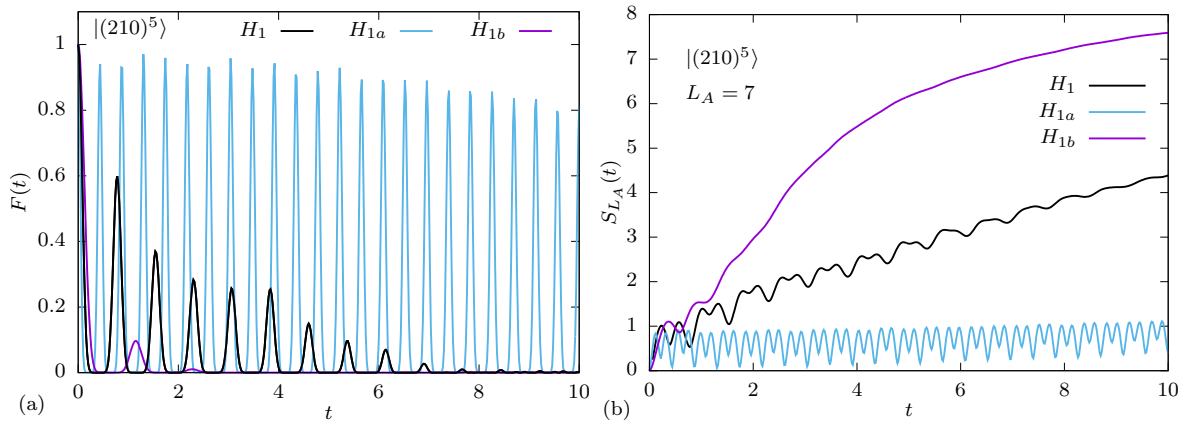

Figure A.1: Time evolution of (a) fidelity $|\langle\psi(t)|\psi(0)\rangle|^2$ and (b) entanglement entropy $S_{L_{\mathrm{A}}=7}(t)$ governed by three different Hamiltonians, $\hat{H}_1$, $\hat{H}_{1\mathrm{a}}$ and $\hat{H}_{1\mathrm{b}}$. System size $L = 15$ and initial state $|(210)^5\rangle$.

Appendix B

Derivation of fidelity in the extended cluster approximation

Here we derive Eq. (2.28) from Chapter 2. For system size $L = 3$, the Hilbert space of the extended cluster is spanned by only four configurations:

$$\begin{pmatrix}1\\0\\0\\0\end{pmatrix} = |300\rangle, \quad \begin{pmatrix}0\\1\\0\\0\end{pmatrix} = |210\rangle, \quad \begin{pmatrix}0\\0\\1\\0\end{pmatrix} = |120\rangle, \quad \begin{pmatrix}0\\0\\0\\1\end{pmatrix} = |111\rangle. \tag{B.1}$$

The Hamiltonian reduced to this subspace is

$$\hat{H}_1^{\check{c}} = -\begin{pmatrix} 0 & 2\sqrt{3} & 0 & 0 \\ 2\sqrt{3} & 0 & 2 & 0 \\ 0 & 2 & 0 & \sqrt{2} \\ 0 & 0 & \sqrt{2} & 0 \end{pmatrix}. \tag{B.2}$$

Its eigenvalues are

$$E_1 = -\alpha, \; E_2 = \alpha, \; E_3 = -\beta, \; E_4 = \beta, \tag{B.3}$$

and its eigenvectors

$$|1\rangle = \begin{pmatrix} a \\ b \\ c \\ d \end{pmatrix}, \; |2\rangle = \begin{pmatrix} -a \\ b \\ -c \\ d \end{pmatrix}, \; |3\rangle = \begin{pmatrix} -c \\ -d \\ a \\ b \end{pmatrix}, \; |4\rangle = \begin{pmatrix} c \\ -d \\ -a \\ b \end{pmatrix}, \tag{B.4}$$

where $\alpha = \sqrt{9+\sqrt{57}} \approx 4.06815$, $\beta = \sqrt{9-\sqrt{57}} \approx 1.20423$, $a \approx 0.591050$, $b \approx 0.694113$, $c \approx 0.388150$ and $d \approx 0.134933$. There are no simple analytical expressions for the coefficients a, b, c and d.

The configuration $|210\rangle$ evolves as

$$\begin{aligned} |\psi_1^{\tilde{c}}(t)\rangle \;\; = \;\; & -2i\,(ab\sin\alpha t + cd\sin\beta t)\,|300\rangle \\ & +2\left(b^2\cos\alpha t + d^2\cos\beta t\right)|210\rangle \\ & -2i\,(bc\sin\alpha t - ad\sin\beta t)\,|120\rangle \\ & +2bd\,(\,\cos\alpha t - \,\cos\beta t)\,|111\rangle, \end{aligned} \tag{B.5}$$

which can also be generalized to larger systems

$$|\Psi_n^{\tilde{c}}(t)\rangle = |(210)^n(t)\rangle = 2^n\left(b^2\cos\alpha t + d^2\cos\beta t\right)^n|(210)^n\rangle + ... \tag{B.6}$$

Finally, the fidelity evolves as

$$F_n^{\tilde{c}}(t) = |\langle\Psi_n^{\tilde{c}}(0)|\Psi_n^{\tilde{c}}(t)\rangle|^2 = 4^n|b^2\cos\alpha t + d^2\cos\beta t|^{2n}. \tag{B.7}$$

The period of revivals is approximately $T \approx \pi/\alpha \approx 0.772241$, and the first peak height exponentially decreases as

$$F_{L=3n}^{\tilde{c}}(T) = 4^n|d^2\cos\frac{\pi\beta}{\alpha} - b^2|^{2n} \approx 0.887017^n \approx \mathrm{e}^{-0.119891n} \approx \mathrm{e}^{-0.039964L}. \tag{B.8}$$

Eqs. (B.6) and (B.7) are exact for non-translation-invariant initial states, but just an approximation for the translation symmetric case. This is due to the fact that different translations of 300, 210 and 120 no longer evolve independently in that case, as they are connected to each other through the configuration 111. However, this approximation becomes better with increasing the system size, as the configuration $(111)^n$ becomes further away from the initial state $(210)^n$ and the probability that this configuration will be reached decreases.

Appendix C

The effective model from Chapter 3

In this Appendix we derive the effective Hamiltonian $\hat{H}_{\text{eff},1}$ (3.7) which corresponds to the time-dependent Hamiltonian (3.3) from Chapter 3. We also show the explicit form of its momentum-space representation $\hat{\mathcal{H}}_{\text{eff},1}(\mathbf{k})$.

C.1 Real space

After a unitary transformation into the rotating frame $\tilde{\psi} = \mathrm{e}^{-i\hat{W}t}\psi$, where $\tilde{\psi}$ and ψ are the old and the new wave functions, and $\hat{W}$ is the staggered potential, the new time-dependent Hamiltonian that describes the experimental setup is given by [70]

$$\hat{H}(t) = J_y \sum_{l,m} \left(\hat{a}^\dagger_{l,m+1}\hat{a}_{l,m} + \hat{a}^\dagger_{l,m-1}\hat{a}_{l,m} \right) + \hat{V}^{(+1)}\mathrm{e}^{i\omega t} + \hat{V}^{(-1)}\mathrm{e}^{-i\omega t} + \frac{U}{2}\sum_{l,m} \hat{n}_{l,m}\left(\hat{n}_{l,m} - 1\right), \quad \text{(C.1)}$$

where

$$\hat{V}^{(+1)} = \kappa/2 \sum_{l,m} \hat{n}_{l,m} g(l,m) - J_x \sum_{l_{\text{odd}},m} \left(\hat{a}^\dagger_{l+1,m}\hat{a}_{l,m} + \hat{a}^\dagger_{l-1,m}\hat{a}_{l,m} \right) \quad \text{(C.2)}$$

$$\hat{V}^{(-1)} = \kappa/2 \sum_{l,m} \hat{n}_{l,m} g^*(l,m) - J_x \sum_{l_{\text{even}},m} \left(\hat{a}^\dagger_{l+1,m}\hat{a}_{l,m} + \hat{a}^\dagger_{l-1,m}\hat{a}_{l,m} \right) \quad \text{(C.3)}$$

$$g(l,m) = \cos(l\pi/2 - \pi/4)\mathrm{e}^{i(\phi_0 - m\pi/2)} + \cos(l\pi/2 + \pi/4)\mathrm{e}^{i(m\pi/2 - \phi_0 - \pi/2)}. \quad \text{(C.4)}$$

The kick operator is given by

$$\hat{K}(t) = \frac{1}{i\omega}\left(\hat{V}^{(+1)}\mathrm{e}^{i\omega t} - \hat{V}^{(-1)}\mathrm{e}^{-i\omega t} \right) + \mathcal{O}\left(\frac{1}{\omega^2}\right), \quad \text{(C.5)}$$

and the effective Hamiltonian by

$$\hat{H}_{\text{eff}} = \underbrace{\hat{H}_0}_{\hat{H}^{(0)}_{\text{eff}}} + \underbrace{\frac{1}{\omega}\left[\hat{V}^{(+1)}, \hat{V}^{(-1)}\right]}_{\hat{H}^{(1)}_{\text{eff}}} + \underbrace{\frac{1}{2\omega^2}\left(\left[\left[\hat{V}^{(+1)}, \hat{H}_0\right], \hat{V}^{(-1)}\right] + \left[\left[\hat{V}^{(-1)}, \hat{H}_0\right], \hat{V}^{(+1)}\right]\right)}_{\hat{H}^{(2)}_{\text{eff}}} + \mathcal{O}\left(\frac{1}{\omega^3}\right). \tag{C.6}$$

If we assume that the driving frequency is high and interactions are weak, the interaction term and almost all $\mathcal{O}\left(\frac{1}{\omega^2}\right)$ terms can be neglected. After substituting Eqs. (C.1), (C.2) and (C.3) into Eq. (C.6) we obtain:

$$\hat{H}^{(0)}_{\text{eff}} = -J_y \sum_{l,m}\left(\hat{a}^\dagger_{l,m+1}\hat{a}_{l,m} + \hat{a}^\dagger_{l,m-1}\hat{a}_{l,m}\right) \tag{C.7}$$

$$\begin{aligned}\hat{H}^{(1)}_{\text{eff}} =& \frac{1}{\omega}\left[\frac{\kappa}{2}\sum_{l,m}\hat{a}^\dagger_{l,m}\hat{a}_{l,m}\; g(l,m) - J_x \sum_{l_{\text{odd}},m}\left(\hat{a}^\dagger_{l+1,m}\hat{a}_{l,m} + \hat{a}^\dagger_{l-1,m}\hat{a}_{l,m}\right),\right.\\ &\left.\frac{\kappa}{2}\sum_{l,m}\hat{a}^\dagger_{l,m}\hat{a}_{l,m}\; g^*(l,m) - J_x \sum_{l_{\text{even}},m}\left(\hat{a}^\dagger_{l+1,m}\hat{a}_{l,m} + \hat{a}^\dagger_{l-1,m}\hat{a}_{l,m}\right)\right]\\ =& \hat{H}_1 + \hat{H}_2 + \hat{H}_3 + \hat{H}_4.\end{aligned} \tag{C.8}$$

We will now separately calculate each term:

$$\begin{aligned}\hat{H}_1 =& -\frac{J_x\kappa}{2\omega}\sum_{l_{\text{odd}},m,l',m'} g^*(l',m')\left[\hat{a}^\dagger_{l+1,m}\hat{a}_{l,m} + \hat{a}^\dagger_{l-1,m}\hat{a}_{l,m}, \hat{a}^\dagger_{l',m'}\hat{a}_{l',m'}\right]\\ =& -\frac{J_x\kappa}{2\omega}\sum_{l_{\text{odd}},m}\left[\Big(g^*(l,m) - g^*(l+1,m)\Big)\hat{a}^\dagger_{l+1,m}\hat{a}_{l,m} + \Big(g^*(l,m) - g^*(l-1,m)\Big)\hat{a}^\dagger_{l-1,m}\hat{a}_{l,m}\right]\end{aligned} \tag{C.9}$$

$$\begin{aligned}\hat{H}_2 =& -\frac{J_x\kappa}{2\omega}\sum_{l_{\text{even}},m,l',m'} g(l',m')\left[\hat{a}^\dagger_{l',m'}\hat{a}_{l',m'}, \hat{a}^\dagger_{l+1,m}\hat{a}_{l,m} + \hat{a}^\dagger_{l-1,m}\hat{a}_{l,m}\right]\\ =& \frac{J_x\kappa}{2\omega}\sum_{l_{\text{even}},m}\left[\Big(g(l,m) - g(l+1,m)\Big)\hat{a}^\dagger_{l+1,m}\hat{a}_{l,m} + \Big(g(l,m) - g(l-1,m)\Big)\hat{a}^\dagger_{l-1,m}\hat{a}_{l,m}\right]\end{aligned} \tag{C.10}$$

$$\begin{aligned}\hat{H}_3 =& \frac{J_x^2}{\omega}\sum_{l_{\text{odd}},m,l'_{\text{even}},m'}\left[\hat{a}^\dagger_{l+1,m}\hat{a}_{l,m} + \hat{a}^\dagger_{l-1,m}\hat{a}_{l,m}, \hat{a}^\dagger_{l'+1,m'}\hat{a}_{l',m'} + \hat{a}^\dagger_{l'-1,m'}\hat{a}_{l',m'}\right]\\ =& \frac{J_x^2}{\omega}\sum_{l_{\text{odd}},m}\left(2\hat{a}^\dagger_{l+1,m}\hat{a}_{l+1,m} + \hat{a}^\dagger_{l+3,m}\hat{a}_{l+1,m} + \hat{a}^\dagger_{l-1,m}\hat{a}_{l+1,m} - 2\hat{a}^\dagger_{l,m}\hat{a}_{l,m} - \hat{a}^\dagger_{l+2,m}\hat{a}_{l,m} - \hat{a}^\dagger_{l-2,m}\hat{a}_{l,m}\right)\\ =& \frac{J_x^2}{\omega}\sum_{l,m}(-1)^l\left(2\hat{a}^\dagger_{l,m}\hat{a}_{l,m} + \hat{a}^\dagger_{l+2,m}\hat{a}_{l,m} + \hat{a}^\dagger_{l-2,m}\hat{a}_{l,m}\right)\end{aligned} \tag{C.11}$$

$$\hat{H}_4 = \frac{\kappa^2}{4\omega} \sum_{l,m,l',m'} g(l,m)g^*(l',m') \left[\hat{a}^\dagger_{l,m}\hat{a}_{l,m}, \hat{a}^\dagger_{l',m'}\hat{a}_{l',m'} \right] = 0. \tag{C.12}$$

Using trigonometric identities and

$$\begin{aligned} g(l,m) - g(l \pm 1, m) = \pm \sqrt{2} \Big(& \sin((2l \pm 1 - 1)\pi/4) e^{i(\pi/4 - m\pi/2)} \\ & + \sin((2l \pm 1 + 1)\pi/4) e^{i(m\pi/2 - 3\pi/4)} \Big), \end{aligned} \tag{C.13}$$

we can rewrite the sum of terms (C.9) and (C.10) in a more convenient form

$$\hat{H}_1 + \hat{H}_2 = \frac{J_x \kappa}{\sqrt{2}\omega} \sum_{l,m} \left(e^{i\left((m-l)\pi/2 - \pi/4\right)} \hat{a}^\dagger_{l,m}\hat{a}_{l-1,m} + e^{-i\left((m-l-1)\pi/2 - \pi/4\right)} \hat{a}^\dagger_{l,m}\hat{a}_{l+1,m} \right). \tag{C.14}$$

The only $\mathcal{O}\left(\frac{1}{\omega^2}\right)$ ($\hat{H}^{(2)}_{\text{eff}}$) term that cannot be neglected in the parameter range that we use is [70]

$$\frac{J_y}{2} \frac{\kappa^2}{\omega^2} \sum_{l,m} \left(\hat{a}^\dagger_{l,m+1}\hat{a}_{l,m} + \hat{a}^\dagger_{l,m-1}\hat{a}_{l,m} \right). \tag{C.15}$$

Finally, the effective Hamiltonian becomes

$$\begin{aligned} \hat{H}_{\text{eff},1} = & \frac{J_x \kappa}{\sqrt{2}\omega} \sum_{l,m} \left(e^{i\left((m-l-1)\pi/2 - \pi/4\right)} \hat{a}^\dagger_{l+1,m}\hat{a}_{l,m} + e^{-i\left((m-l)\pi/2 - \pi/4\right)} \hat{a}^\dagger_{l-1,m}\hat{a}_{l,m} \right) \\ & - J_y \left(1 - \frac{1}{2}\frac{\kappa^2}{\omega^2} \right) \sum_{l,m} \left(\hat{a}^\dagger_{l,m+1}\hat{a}_{l,m} + \hat{a}^\dagger_{l,m-1}\hat{a}_{l,m} \right) \qquad \text{(C.16)} \\ & + \frac{J_x^2}{\omega} \sum_{l,m} (-1)^l \left(2\hat{a}^\dagger_{l,m}\hat{a}_{l,m} + \hat{a}^\dagger_{l+2,m}\hat{a}_{l,m} + \hat{a}^\dagger_{l-2,m}\hat{a}_{l,m} \right) \qquad \text{(C.17)} \end{aligned}$$

with the renormalized nearest-neighbor hopping amplitudes

$$J'_x = \frac{J_x \kappa}{\sqrt{2}\omega} = J_y \tag{C.18}$$

and

$$J'_y = J_y \left(1 - \frac{1}{2}\frac{\kappa^2}{\omega^2} \right), \tag{C.19}$$

and a next-nearest-neighbor along $\mathbf{e}_x$ hopping term proportional to $\frac{J_x^2}{\omega}$ in (C.17).

C.2 Momentum space

If we choose the unit cell as in Fig. 3.1(a) (lattice sites $\mathtt{A} = (1,0)$, $\mathtt{B} = (2,0)$, $\mathtt{C} = (3,0)$ and $\mathtt{D} = (4,0)$), the momentum-space representation of the effective Hamiltonian without correction

$\hat{H}_{\text{eff},0}$ (3.6) is given by a 4×4 matrix

$$\hat{\mathcal{H}}_{\text{eff},0}(\mathbf{k}) = \begin{pmatrix} 0 & J'_x e^{-i\frac{3\pi}{4}} - J'_y e^{-i\mathbf{k}\mathbf{R}_2} & 0 & J'_x e^{-i\frac{3\pi}{4}-i\mathbf{k}\mathbf{R}_1} - J'_y e^{i\mathbf{k}(\mathbf{R}_2-\mathbf{R}_1)} \\ J'_x e^{i\frac{3\pi}{4}} - J'_y e^{i\mathbf{k}\mathbf{R}_2} & 0 & J'_x e^{-i\frac{\pi}{4}} - J'_y e^{-i\mathbf{k}\mathbf{R}_2} & 0 \\ 0 & J'_x e^{i\frac{\pi}{4}} - J'_y e^{i\mathbf{k}\mathbf{R}_2} & 0 & J'_x e^{i\frac{\pi}{4}} - J'_y e^{-i\mathbf{k}\mathbf{R}_2} \\ J'_x e^{i\frac{3\pi}{4}+i\mathbf{k}\mathbf{R}_1} - J'_y e^{i\mathbf{k}(\mathbf{R}_1-\mathbf{R}_2)} & 0 & J'_x e^{-i\frac{\pi}{4}} - J'_y e^{i\mathbf{k}\mathbf{R}_2} & 0 \end{pmatrix}, \quad \text{(C.20)}$$

where $\mathbf{R}_1$ and $\mathbf{R}_2$ are the lattice vectors $\mathbf{R}_1 = (4,0)$ and $\mathbf{R}_2 = (1,1)$, and $\mathbf{k}$ is in the first Brillouin zone, which is given by the reciprocal lattice vectors $\mathbf{b}_1 = \frac{\pi}{2}(1,-1)$ and $\mathbf{b}_2 = 2\pi(0,1)$.

When the $\frac{J_x^2}{\omega}$ correction is included in the effective Hamiltonian, $\hat{H}_{\text{eff},1}$ (3.7), the unit cell is doubled, see Fig. 3.1(b), and the first Brillouin zone is therefore halved. If we now choose the lattice sites $\mathtt{a} = (1,0)$, $\mathtt{B} = (2,0)$, $\mathtt{c} = (3,0)$, $\mathtt{D} = (4,0)$, $\mathtt{A} = (2,1)$, $\mathtt{b} = (3,1)$, $\mathtt{C} = (4,1)$ and $\mathtt{d} = (5,1)$ for the unit cell, the momentum-space representation of the effective Hamiltonian will be an 8×8 matrix

$$\hat{\mathcal{H}}_{\text{eff},1}(\mathbf{k}) = \begin{pmatrix} -\frac{2J_x^2}{\omega} & J'_x e^{-i\frac{3\pi}{4}} & -\frac{J_x^2}{\omega}(1+e^{i\mathbf{k}\mathbf{R}_1}) & J'_x e^{-i(\frac{3\pi}{4}-\mathbf{k}\mathbf{R}_1)} & 0 & -J'_y e^{i\mathbf{k}\mathbf{R}_2} & 0 & -J'_y e^{i\mathbf{k}\mathbf{R}_1} \\ J'_x e^{i\frac{3\pi}{4}} & \frac{2J_x^2}{\omega} & J'_x e^{-i\frac{\pi}{4}} & \frac{J_x^2}{\omega}(1+e^{i\mathbf{k}\mathbf{R}_1}) & -J'_y & 0 & -J'_y e^{i\mathbf{k}\mathbf{R}_2} & 0 \\ -\frac{J_x^2}{\omega}(1+e^{-i\mathbf{k}\mathbf{R}_1}) & J'_x e^{i\frac{\pi}{4}} & -\frac{2J_x^2}{\omega} & J'_x e^{i\frac{\pi}{4}} & 0 & -J'_y & 0 & -J'_y e^{i\mathbf{k}\mathbf{R}_2} \\ J'_x e^{i(\frac{3\pi}{4}-\mathbf{k}\mathbf{R}_1)} & \frac{J_x^2}{\omega}(1+e^{-i\mathbf{k}\mathbf{R}_1}) & J'_x e^{-i\frac{\pi}{4}} & \frac{2J_x^2}{\omega} & -J'_y e^{-i\mathbf{k}(\mathbf{R}_1-\mathbf{R}_2)} & 0 & -J'_y & 0 \\ 0 & 0 & 0 & -J'_y e^{i\mathbf{k}(\mathbf{R}_1-\mathbf{R}_2)} & \frac{2J_x^2}{\omega} & J'_x e^{-i\frac{3\pi}{4}} & \frac{J_x^2}{\omega}(1+e^{i\mathbf{k}\mathbf{R}_1}) & J'_x e^{-i(\frac{3\pi}{4}-\mathbf{k}\mathbf{R}_1)} \\ -J'_y e^{-i\mathbf{k}\mathbf{R}_2} & 0 & -J'_y & 0 & J'_x e^{i\frac{3\pi}{4}} & -\frac{2J_x^2}{\omega} & J'_x e^{-i\frac{\pi}{4}} & -\frac{J_x^2}{\omega}(1+e^{i\mathbf{k}\mathbf{R}_1}) \\ 0 & -J'_y e^{-i\mathbf{k}\mathbf{R}_2} & 0 & -J'_y & \frac{J_x^2}{\omega}(1+e^{-i\mathbf{k}\mathbf{R}_1}) & J'_x e^{i\frac{\pi}{4}} & \frac{2J_x^2}{\omega} & J'_x e^{i\frac{\pi}{4}} \\ -J'_y e^{-i\mathbf{k}\mathbf{R}_1} & 0 & -J'_y e^{-i\mathbf{k}\mathbf{R}_2} & 0 & J'_x e^{i(\frac{3\pi}{4}-\mathbf{k}\mathbf{R}_1)} & -\frac{J_x^2}{\omega}(1+e^{-i\mathbf{k}\mathbf{R}_1}) & J'_x e^{-i\frac{\pi}{4}} & -\frac{2J_x^2}{\omega} \end{pmatrix}, \quad \text{(C.21)}$$

with the lattice vectors $\mathbf{R}_1 = (4,0)$ and $\mathbf{R}_2 = (2,2)$. The reciprocal lattice vectors are then $\mathbf{b}_1 = \frac{\pi}{2}(1,-1)$ and $\mathbf{b}_2 = \pi(0,1)$.

The energy bands of $\hat{\mathcal{H}}_{\text{eff},1}(\mathbf{k})$ are shown in Figs. 3.2 and C.1.

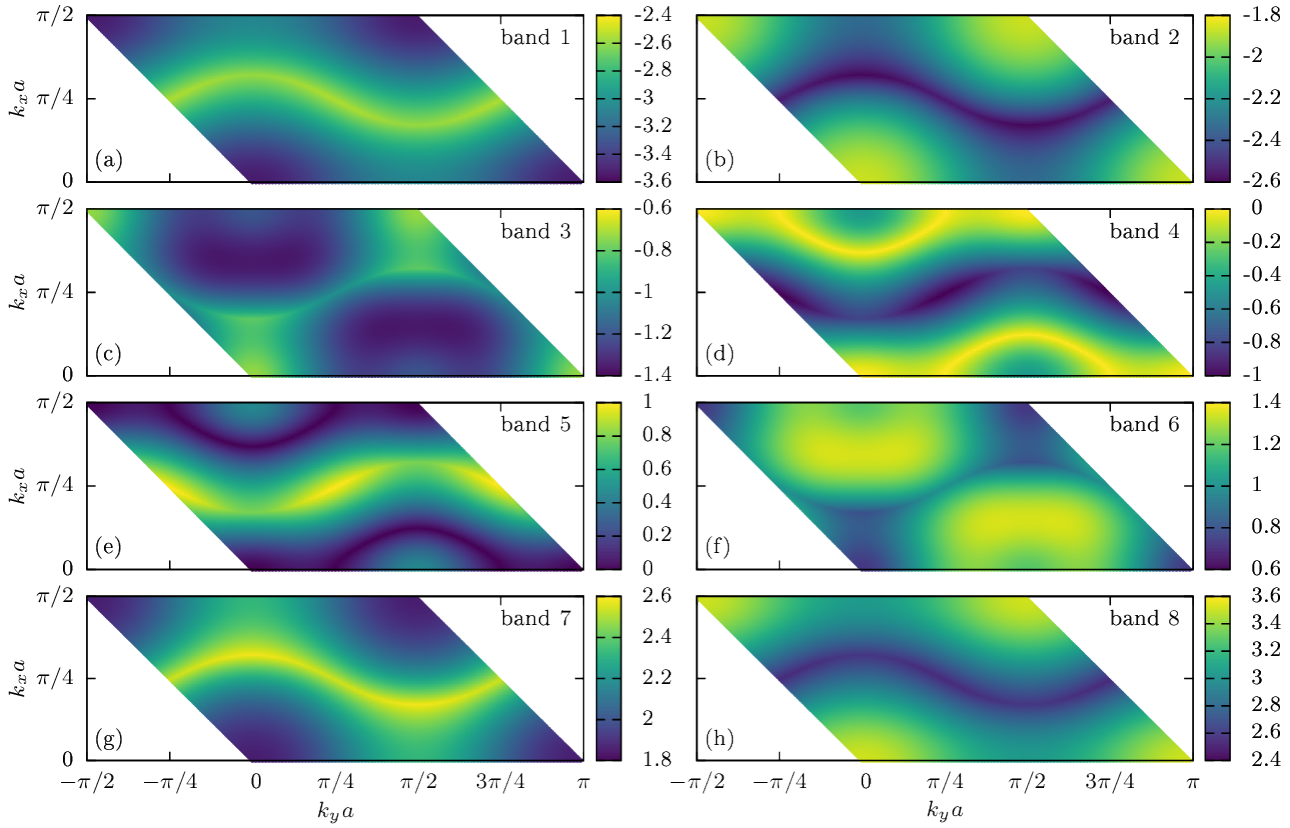

Figure C.1: Eight energy subbands of $\hat{\mathcal{H}}_{\text{eff},1}(\mathbf{k})$ for the driving frequency $\omega = 20$. Subbands 1 and 2 form the lowest band with Chern number $c_1 = 1$, subbands 3, 4, 5, and 6 form the middle band with $c_2 = -2$, and subbands 7 and 8 form the highest band with $c_3 = 1$.

Appendix D

Description of incoherent bosons

Here we explain in more details the method which we use to treat weakly interacting bosons in Chapter 3. In a typical condensed-matter system constituent particles are electrons. Due to their fermionic statistics, at low enough temperatures, and with Fermi energy above the lowest band, that band of the topological model is uniformly occupied, and consequently the transverse Hall conductivity can be expressed in terms of the Chern number (1.5) [69]. In contrast, weakly interacting bosons in equilibrium form a Bose-Einstein condensate in the band minima and only probe the local Berry curvature [167].

Yet in the experiment [70] the Chern number was successfully measured using bosonic atoms of ^{87}Rb. This was possible because in the process of ramping up the drive (3.4), the initial Bose-Einstein condensate was transferred into an incoherent bosonic mixture. Conveniently, it turned out that the bosonic distribution over the states of the lowest band of the effective Floquet Hamiltonian was nearly uniform. Motivated by the experimental procedure, we model the initial bosonic state by a statistical matrix

$$\rho(t=0) = \prod_{k=1}^{N_m} |k, N_p\rangle\langle k, N_p| \tag{D.1}$$

where the states $|k\rangle = a_k^\dagger|0\rangle$ approximately correspond to the lowest-band eigenstates of $\hat{H}_{\text{eff}}$ and each of these N_m states is occupied by N_p atoms $|k, N_p\rangle = \mathcal{N}(a_k^\dagger)^{N_p}|0\rangle$.

A procedure for selecting the states $|k\rangle$ is described in Refs. [70, 168]. In order to probe the Chern number of the lowest band, the states $|k\rangle$ should correspond closely to the lowest-band eigenstates of $\hat{H}_{\text{eff}}$. At the same time, in the experiment in the initial moment the atomic cloud is spatially localized. According to Refs. [70, 168] the optimal approach is to consider a steep confining potential and to use the low-lying eigenstates of

$$\hat{H}_{\text{initial}} = \hat{h}^{\text{eff}} + \left(\frac{r}{r_0}\right)^\zeta, \tag{D.2}$$

where in our calculations $\hat{h}^{\text{eff}}$ is either $\hat{H}_{\text{eff},0}$ from Eq. (3.6) or $\hat{H}_{\text{eff},1}$ from Eq. (3.7) and the parameters of the confining potential are set to $r_0 = 20, \zeta = 20$.

The dynamics of the initial state (D.1) is induced by a double quench: at $t_0 = 0$ the atomic cloud is released from the confining potential and exposed to a uniform force of intensity F along the y direction. During the whole procedure the driving providing the laser-assisted tunneling, defined in Eq. (3.4), is running.

The main observables of interest are the center-of-mass position along x direction

$$x(t) = \Big\langle \sum_{l,m} l |\psi_{l,m}(t)|^2 \Big\rangle, \tag{D.3}$$

and the population of the ith band of the effective model

$$\eta_i(t) = \Big\langle \sum_{|k\rangle \in i\text{-th band}} \Big| \sum_{l,m} \alpha_{lm}^{k*} \psi_{lm}(t) \Big|^2 \Big\rangle, \tag{D.4}$$

where the states $|k\rangle = \sum_{l,m} \alpha_{lm}^{k} |l,m\rangle$ correspond to the eigenstates of the effective model. Here, angle brackets $\langle\ \rangle$ denote averaging over N_{samples} sets of initial conditions.

In the case of non-interacting particles, these and other quantities can be numerically accessed by solving the single-particle time-dependent Schrödinger equation for N_m different initial states $|k\rangle$. This is equivalent to sampling the initial state according to Eq. (3.8).

In the end, we give two technical remarks. First, all our calculations are done in the rotating frame; see Eq. (C.1) in Appendix C. The staggered potential (3.2) is removed in this way. Second, in the case when the evolution is governed by the time-dependent Hamiltonian (3.9), the initial state is multiplied by the operator $\mathrm{e}^{-i\hat{K}(0)}$ in order to properly compare these results to the ones obtained from the evolution governed by the effective Hamiltonian (3.10); see Eq. (3.5).

Appendix

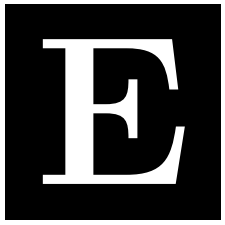

Initial quadratic regime

In this Appendix we explain the initial quadratic behavior exhibited by several observables in Chapter 3. For simplicity, we will consider only the case without the confining potential and with very weak force $F = 0.01$. The initial state is a Bose-Einstein condensate in one of the eigenstates of the effective Hamiltonian. The results are later averaged over all first band eigenstates.

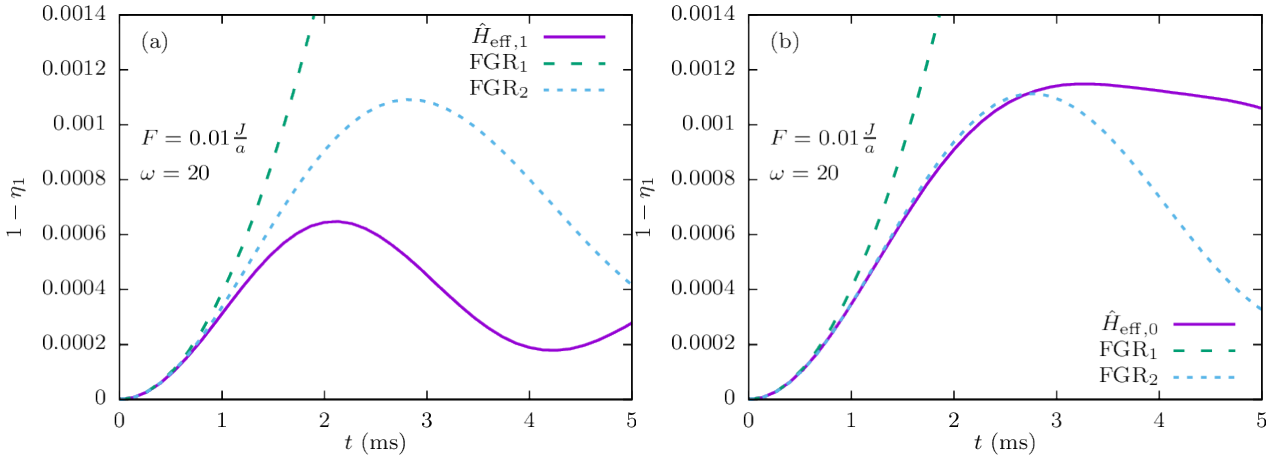

Figure E.1: Population in higher bands, comparison of numerical results (solid line) with the Fermi's golden rule in the first and second approximation (dashed lines). Band populations are calculated for an initial BEC in an eigenstate of the effective Hamiltonian and then averaged over (approximately) all states in the first band. (a) Initial state and evolution from the effective Hamiltonian with correction $\hat{H}_{\text{eff},1}$, Eq. (3.7). (b) Without the correction, $\hat{H}_{\text{eff},0}$, Eq. (3.6).

Fermi's golden rule predicts that the probability for transition from an initial state ψ_i to a final state ψ_f, induced by a perturbation $\Delta\hat{H}$, is proportional to the square of matrix elements $|\langle\psi_i|\Delta\hat{H}|\psi_f\rangle|^2$. In this case, the perturbation is $\Delta\hat{H} = F\hat{y}$. If we assume that the probability of a particle being in the initial state is always $P_i(t) = |\psi_i(t)|^2 \approx 1$, Fermi's golden rule predicts [236]

$$P_{i\to f}^{\text{FGR}_1}(t) = \frac{1}{\hbar^2}|\langle\psi_i|\Delta\hat{H}|\psi_f\rangle|^2 t^2. \tag{E.1}$$

If we now also consider transitions from the other states to the initial state, but keep the assumption that the populations in other states are small $P_{j\neq i}(t) = |\psi_{j\neq i}(t)|^2 \ll 1$, the time-dependent perturbation theory then predicts [236]

$$P_{i\to f}^{\mathrm{FGR}_2}(t) = |\langle i|\Delta\hat{H}|f\rangle|^2 \frac{1 - 2\mathrm{e}^{-\frac{\Gamma}{2\hbar}t}\cos\left(\frac{E_f - E_i}{\hbar}t\right) + \mathrm{e}^{-\frac{\Gamma}{\hbar}t}}{\left(E_f - E_i\right)^2 + \frac{\Gamma^2}{4}}, \tag{E.2}$$

where $\Gamma = \frac{2\pi}{\hbar}|\langle i|\Delta\hat{H}|f\rangle|^2$ and E_i (E_f) is the energy of the initial (final) state.

We plot the numerical results and both theoretical predictions from Fermi's golden rule in Fig. E.1. Here we can see that all three curves agree well for short times, the second approximation longer remains close to the numerical results, and that the initial quadratic regime is reproduced by theory. This is the so-called quantum Zeno regime [195].

Appendix F

Effects of interactions

Here we provide further details about the effects of interactions on the dynamics of weakly interacting incoherent bosons described in Chapter 3. In particular, we consider the evolution of the kinetic and interaction energy, as well as the probability density distribution in momentum space.

F.1 Energy

Time evolution of kinetic and interaction energy per particle for different interaction strengths is plotted in Fig. F.1. Here we define the kinetic energy per particle as the expectation value of the time-dependent Hamiltonian (C.1) divided by the total number of particles

$$E_{\mathrm{kin}}(t) = \frac{1}{N}\Big\langle \sum_{l,m,i,j} \psi^*_{l,m}(t) H_{lm,ij}(t) \psi_{i,j}(t) \Big\rangle, \tag{F.1}$$

while the interaction energy per particle is

$$E_{\mathrm{int}}(t) = \frac{1}{N}\frac{U}{2}\Big\langle \sum_{l,m} |\psi_{l,m}(t)|^2 \left(|\psi_{l,m}(t)|^2 - 1 \right) \Big\rangle. \tag{F.2}$$

Both energies grow with increasing interaction coefficient U.

When the interactions are strong enough and after long enough time, the atoms become equally distributed between the eigenstates of the Hamiltonian $\hat{H}(t)$. As the energy spectrum of $\hat{H}(t)$ is symmetric around zero, the expectation value of $\hat{H}(t)$ (kinetic energy) should be zero when all bands are equally populated. We can see this in Fig. F.1(a), where the kinetic energy approaches zero at $t \approx 50$ ms for the case $U = 0.05$.

The interaction energy at first rapidly decreases, as the cloud rapidly expands after turning off the confinement potential $\hat{V}_{\mathrm{conf}}$, and after that continues to slowly decrease as the cloud

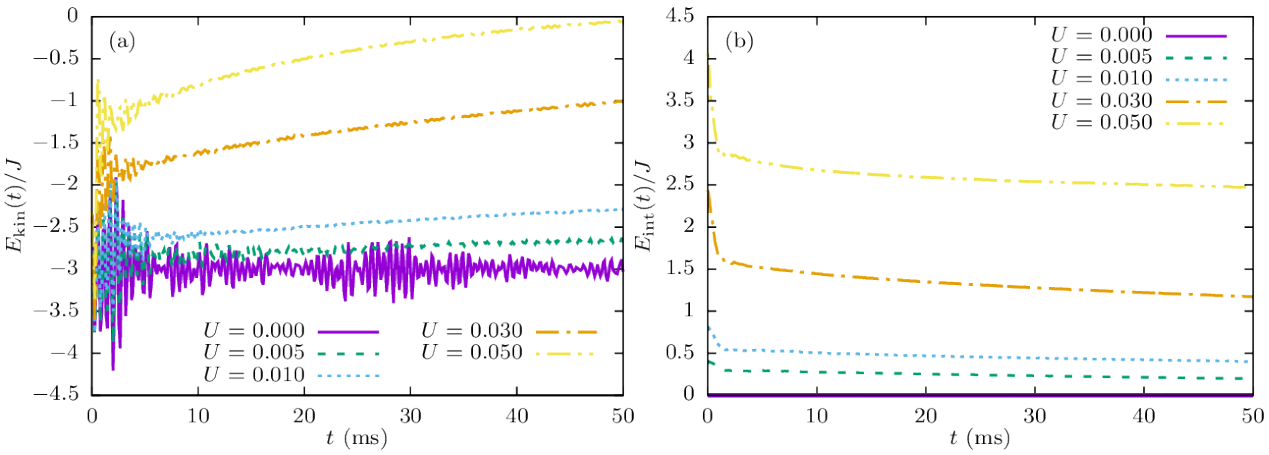

Figure F.1: (a) Kinetic energy per particle (expectation value of the time-dependent Hamiltonian $E_{\mathrm{kin}}(t) = \frac{1}{N}\left\langle \sum_{l,m,i,j} \psi^*_{l,m}(t) H_{lm,ij}(t) \psi_{i,j}(t) \right\rangle$ divided by the total number of particles N) for several different interaction strengths. (b) Interaction energy per particle $E_{\mathrm{int}}(t) = \frac{1}{N}\frac{U}{2}\left\langle \sum_{l,m} |\psi_{l,m}(t)|^2 \left(|\psi_{l,m}(t)|^2 - 1\right) \right\rangle$. U is given in units where $J = 1$.

slowly expands; see Fig. F.1(b).

These considerations also provide a possibility to discuss the applicability of the approximative method introduced in Section 3.3. As we work in the regime of high frequency $\omega = 20$, we find that for weak interaction, at short enough times of propagation, the energy is approximately conserved. At stronger values of $U \geq 0.01$ we observe a slow increase in the total energy on the considered time scales. In both cases we do not find the onset of parametric instabilities [174]. If present, these instabilities are signaled by an order of magnitude increase in energy on a short time scale, that we do not find.

In addition, the two-body interaction can deplete the occupancies of initial coherent modes [172, 184] and limit the validity of our approach. In principle, these types of processes can be addressed by including quantum fluctuations along the lines of the full truncated Wigner approach [187]. Yet, we set our parameters in such a way that these additional contributions are small.

F.2 Momentum-space density distribution

The momentum-space probability densities at the initial moment and after 75 driving periods (50 ms) are shown in Fig. F.2. The interactions deplete the lowest band, but also smooth out the density distribution.

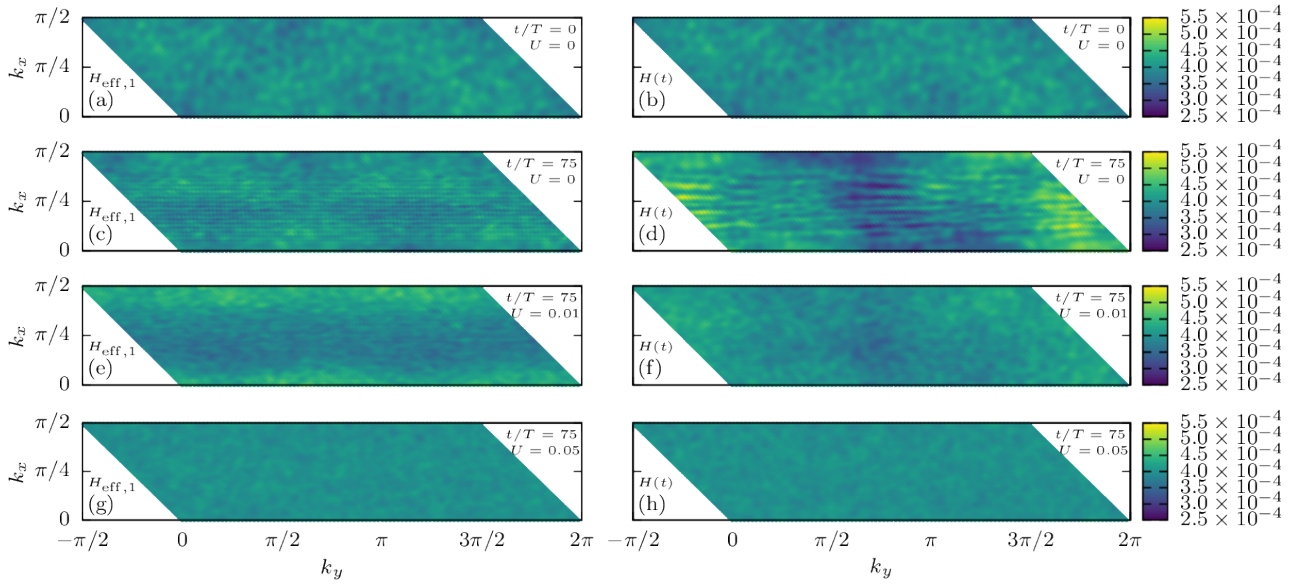

Figure F.2: Momentum-space density distribution in all bands, $\eta_1(\mathbf{k}) + \eta_2(\mathbf{k}) + \eta_3(\mathbf{k})$. U is given in units where $J = 1$. Left: evolution using the time-dependent Hamiltonian $\hat{H}_{\mathrm{eff},1}$. Right: evolution using the time-dependent Hamiltonian $\hat{H}(t)$. (a), (b) Initial state. (c), (d) Final state after 50 ms (75 driving periods), noninteracting case $U = 0$. (e), (f) $U = 0.01$. (g), (h) $U = 0.05$.

Appendix G

The effective model from Chapter 4

In this appendix we review the derivation of the model given in Eq. (4.1) from Chapter 4. The system is described by

$$\hat{H}_{\text{lab}}(t) = \hat{H}_{BH} + \hat{H}_{\text{drive}}(t) + \omega\,\hat{V}, \tag{G.1}$$

where we start with the Bose-Hubbard model

$$\begin{aligned}\hat{H}_{BH} = &- J_x \sum_{m,n} \left(\hat{a}^\dagger_{m+1,n}\hat{a}_{m,n} + \text{H. c.}\right) - J_y \sum_{m,n} \left(\hat{a}^\dagger_{m,n+1}\hat{a}_{m,n} + \text{H. c.}\right) \\ &+ \frac{U}{2}\sum_{m,n} \hat{n}_{m,n}(\hat{n}_{m,n} - 1),\end{aligned} \tag{G.2}$$

and we introduce an offset $\omega\hat{V}$:

$$\hat{V} = \sum_{m,n} n\,\hat{n}_{m,n}. \tag{G.3}$$

This shifted Bose-Hubbard model is exposed to a suitable resonant driving scheme:

$$\hat{H}_{\text{drive}}(t) = \frac{\kappa}{2}\sum_{m,n} \sin\left(\omega t - \phi_{m,n} + \frac{\phi}{2}\right)\hat{n}_{m,n}, \quad \phi_{m,n} = (m+n)\,\phi. \tag{G.4}$$

We assume periodic boundary conditions compatible with the driving term (G.4) in the laboratory frame. To this purpose we use vectors $\mathbf{R}_1 = 4\,\mathbf{e}_x$ and $\mathbf{R}_2 = -\mathbf{e}_x + \mathbf{e}_y$ as presented in Fig. 4.1. For simplicity, we work in the rotating frame

$$|\psi_{\text{rot}}(t)\rangle = e^{i\omega t\hat{V}}|\psi_{\text{lab}}(t)\rangle \tag{G.5}$$

and derive the Schrödinger equation

$$i\frac{d|\psi_{\text{rot}}(t)\rangle}{dt} = \hat{H}_{\text{rot}}(t)|\psi_{\text{rot}}(t)\rangle, \tag{G.6}$$

where

$$\hat{H}_{\mathrm{rot}}(t) = \left(e^{i\omega t\hat{V}}\hat{H}_{\mathrm{lab}}(t)e^{-i\omega t\hat{V}} - \omega\hat{V}\right). \tag{G.7}$$

Now we calculate $\hat{H}_{\mathrm{rot}}(t)$ explicitly. The only nontrivial action of this rotation on $\hat{H}_{\mathrm{lab}}$ comes from the nearest-neighbor hopping along y direction. Indeed, we have

$$e^{i\omega t\hat{V}}\hat{a}^{\dagger}_{m,n}\hat{a}_{m,n'}e^{-i\omega t\hat{V}} = e^{i\omega t(n-n')}\hat{a}^{\dagger}_{m,n}\hat{a}_{m,n'}. \tag{G.8}$$

In total we obtain

$$\begin{aligned}\hat{H}_{\mathrm{rot}}(t) &= -J_x\sum_{m,n}\left(\hat{a}^{\dagger}_{m+1,n}\hat{a}_{m,n} + \text{H. c. }\right) + \frac{U}{2}\sum_{m,n}\hat{n}_{m,n}(\hat{n}_{m,n}-1)\\ &+ e^{i\omega t}\hat{H}_1 + e^{-i\omega t}\hat{H}_{-1} + e^{-i\omega t(L_y-1)}\hat{H}_{L_y-1} + e^{i\omega t(L_y-1)}\hat{H}_{-L_y+1},\end{aligned} \tag{G.9}$$

with

$$\hat{H}_1 = -J_y\sum_{m,n}^{\mathrm{OBC}}\left(\hat{a}^{\dagger}_{m,n+1}\hat{a}_{m,n} - \frac{i}{4}\kappa e^{i(-\phi_{m,n}+\frac{\phi}{2})}\hat{n}_{m,n}\right), \quad \hat{H}_{-1} = \hat{H}_1^{\dagger}, \tag{G.10}$$

$$\hat{H}_{-L_y+1} = -J_y\sum_{m}\hat{a}^{\dagger}_{m,0}\hat{a}_{m-L_y,L_y-1}, \quad \hat{H}_{L_y-1} = \hat{H}^{\dagger}_{-L_y+1}. \tag{G.11}$$

In the terms $\hat{H}_{-L_y+1}$ and $\hat{H}_{L_y-1}$ we take into account periodic boundary conditions along the direction parallel to $\mathbf{R_2}$ as imposed in the laboratory frame. In order to limit the complexity of the numerical calculation, we keep translational invariance and impose the periodic boundary conditions in both directions in the rotating frame. This implies that we will neglect "phasors" $e^{-i\omega t(L_y-1)}$ and $e^{i\omega t(L_y-1)}$. Under these assumptions, we can recast Eq. (G.9) into the time-dependent Hamiltonian given in Eq. (4.1). In practice, this would require engineering additional non-trivial terms in the laboratory frame.

The leading order of the kick operator is given by

$$\hat{K}(t=0) \approx -\frac{\kappa}{2\omega}\sum_{m,n}\cos(\phi_{m,n}-\phi/2)\hat{n}_{m,n}. \tag{G.12}$$

Bibliography

[1] F. Dalfovo, S. Giorgini, L. P. Pitaevskii, and S. Stringari, Rev. Mod. Phys. **71**, 463 (1999).

[2] R. P. Feynman, Int. J. Theor. Phys. **21**, 467 (1982).

[3] I. M. Georgescu, S. Ashhab, and F. Nori, Rev. Mod. Phys. **86**, 153 (2014).

[4] F. Arute *et al.*, Nature **574**, 505 (2019).

[5] I. Bloch, J. Dalibard, and W. Zwerger, Rev. Mod. Phys. **80**, 885 (2008).

[6] I. Bloch, J. Dalibard, and S. Nascimbène, Nat. Phys. **8**, 267 (2012).

[7] R. Blatt and C. F. Roos, Nat. Phys. **8**, 277 (2012).

[8] A. A. Houck, H. E. Türeci, and J. Koch, Nat. Phys. **8**, 292 (2012).

[9] A. Aspuru-Guzik and P. Walther, Nat. Phys. **8**, 285 (2012).

[10] M. W. Doherty, N. B. Manson, P. Delaney, F. Jelezko, J. Wrachtrup, and L. C. L. Hollenberg, Phys. Rep. **528**, 1 (2013).

[11] R. Schirhagl, K. Chang, M. Loretz, and C. L. Degen, Annu. Rev. Phys. Chem. **65**, 83 (2014).

[12] D. Greif, T. Uehlinger, G. Jotzu, L. Tarruell, and T. Esslinger, Science **340**, 1307 (2013).

[13] P. T. Brown *et al.*, Science **363**, 379 (2019).

[14] W. Xu, W. R. McGehee, W. N. Morong, and B. DeMarco, Nat. Commun. **10**, 1588 (2019).

[15] A. Mott, J. Job, J.-R. Vlimant, D. Lidar, and M. Spiropulu, Nature **550**, 375 (2017).

[16] J. R. Muñoz de Nova, K. Golubkov, V. I. Kolobov, and J. Steinhauer, Nature **569**, 688 (2019).

[17] B.-X. Wang, M.-J. Tao, Q. Ai, T. Xin, N. Lambert, D. Ruan, Y.-C. Cheng, F. Nori, F.-G. Deng, and G.-L. Long, npj Quantum Inf. **4**, 52 (2018).

[18] C. Gross and I. Bloch, Science **357**, 995 (2017).

[19] M. P. A. Fisher, P. B. Weichman, G. Grinstein, and D. S. Fisher, Phys. Rev. B **40**, 546 (1989).

[20] J. Hubbard, Proc. R. Soc. Lond. A **276**, 238 (1963).

[21] M. Greiner, O. Mandel, T. Esslinger, T. W. Hänsch, and I. Bloch, Nature **415**, 39 (2002).

[22] T. Langen, R. Geiger, and J. Schmiedmayer, Annu. Rev. Condens. Matter Phys. **6**, 201 (2015).

[23] T. Kinoshita, T. Wenger, and D. S. Weiss, Nature **440**, 900 (2006).

[24] S. Trotzky, Y. A. Chen, A. Flesch, I. P. McCulloch, U. Schollwöck, J. Eisert, and I. Bloch, Nat. Phys. **8**, 325 (2012).

[25] M. Gring, M. Kuhnert, T. Langen, T. Kitagawa, B. Rauer, M. Schreitl, I. Mazets, D. A. Smith, E. Demler, and J. Schmiedmayer, Science **337**, 1318 (2012).

[26] T. Langen, R. Geiger, M. Kuhnert, B. Rauer, and J. Schmiedmayer, Nat. Phys. **9**, 640 (2013).

[27] T. Langen, S. Erne, R. Geiger, B. Rauer, T. Schweigler, M. Kuhnert, W. Rohringer, I. E. Mazets, T. Gasenzer, and J. Schmiedmayer, Science **348**, 207 (2015).

[28] A. M. Kaufman, M. E. Tai, A. Lukin, M. Rispoli, R. Schittko, P. M. Preiss, and M. Greiner, Science **353**, 794 (2016).

[29] Y. Tang, W. Kao, K.-Y. Li, S. Seo, K. Mallayya, M. Rigol, S. Gopalakrishnan, and B. L. Lev, Phys. Rev. X **8**, 021030 (2018).

[30] M. Srednicki, Phys. Rev. E **50**, 888 (1994).

[31] J. M. Deutsch, Phys. Rev. A **43**, 2046 (1991).

[32] M. Rigol, V. Dunjko, and M. Olshanii, Nature **452**, 854 (2008).

[33] L. D'Alessio, Y. Kafri, A. Polkovnikov, and M. Rigol, Adv. Phys. **65**, 239 (2016).

[34] B. Sutherland, *Beautiful models: 70 years of exactly solved quantum many-body problems* (World Scientific Publishing Company, River Edge, 2004).

[35] D. A. Abanin, E. Altman, I. Bloch, and M. Serbyn, Rev. Mod. Phys. **91**, 021001 (2019).

[36] M. Schreiber, S. S. Hodgman, P. Bordia, H. P. Lüschen, M. H. Fischer, R. Vosk, E. Altman, U. Schneider, and I. Bloch, Science **349**, 842 (2015).

[37] J.-y. Choi, S. Hild, J. Zeiher, P. Schauss, A. Rubio-Abadal, T. Yefsah, V. Khemani, D. A. Huse, I. Bloch, and C. Gross, Science **352**, 1547 (2016).

[38] J. Smith, A. Lee, P. Richerme, B. Neyenhuis, P. W. Hess, P. Hauke, M. Heyl, D. A. Huse, and C. Monroe, Nat. Phys. **12**, 907 (2016).

[39] P. Roushan *et al.*, Science **358**, 1175 (2017).

[40] N. Laflorencie, Phys. Rep. **646**, 1 (2016).

[41] C. Gogolin and J. Eisert, Rep. Prog. Phys. **79**, 056001 (2016).

[42] J. Eisert, M. Cramer, and M. B. Plenio, Rev. Mod. Phys. **82**, 277 (2010).

[43] M. Serbyn, Z. Papić, and D. A. Abanin, Phys. Rev. Lett. **110**, 260601 (2013).

[44] R. Nandkishore and D. A. Huse, Annu. Rev. Condens. Matter Phys. **6**, 15 (2015).

[45] W. W. Ho and D. A. Abanin, Phys. Rev. B **95**, 094302 (2017).

[46] H. Bernien, S. Schwartz, A. Keesling, H. Levine, A. Omran, H. Pichler, S. Choi, A. S. Zibrov, M. Endres, M. Greiner, V. Vuletić, and M. D. Lukin, Nature **551**, 579 (2017).

[47] C. J. Turner, A. A. Michailidis, D. A. Abanin, M. Serbyn, and Z. Papić, Nat. Phys. **14**, 745 (2018).

[48] C. J. Turner, A. A. Michailidis, D. A. Abanin, M. Serbyn, and Z. Papić, Phys. Rev. B **98**, 155134 (2018).

[49] E. J. Heller, Phys. Rev. Lett. **53**, 1515 (1984).

[50] S. Moudgalya, S. Rachel, B. A. Bernevig, and N. Regnault, Phys. Rev. B **98**, 235155 (2018).

[51] S. Moudgalya, N. Regnault, and B. A. Bernevig, Phys. Rev. B **98**, 235156 (2018).

[52] C.-J. Lin and O. I. Motrunich, Phys. Rev. Lett. **122**, 173401 (2019).

[53] V. Khemani, C. R. Laumann, and A. Chandran, Phys. Rev. B **99**, 161101 (2019).

[54] A. A. Michailidis, C. J. Turner, Z. Papić, D. A. Abanin, and M. Serbyn, Phys. Rev. X **10**, 011055 (2020).

[55] A. J. A. James, R. M. Konik, and N. J. Robinson, Phys. Rev. Lett. **122**, 130603 (2019).

[56] N. J. Robinson, A. J. A. James, and R. M. Konik, Phys. Rev. B **99**, 195108 (2019).

[57] T. Iadecola and M. Žnidarič, Phys. Rev. Lett. **123**, 036403 (2019).

[58] A. Haldar, D. Sen, R. Moessner, and A. Das, arXiv e-prints (2019), arXiv:1909.04064.

[59] M. Schecter and T. Iadecola, Phys. Rev. Lett. **123**, 147201 (2019).

[60] T. Iadecola, M. Schecter, and S. Xu, Phys. Rev. B **100**, 184312 (2019).

[61] T. Iadecola and M. Schecter, Phys. Rev. B **101**, 024306 (2020).

[62] S. Moudgalya, B. A. Bernevig, and N. Regnault, arXiv e-prints (2019), arXiv:1906.05292.

[63] S. Pai and M. Pretko, Phys. Rev. Lett. **123**, 136401 (2019).

[64] P. Sala, T. Rakovszky, R. Verresen, M. Knap, and F. Pollmann, Phys. Rev. X **10**, 011047 (2020).

[65] V. Khemani, M. Hermele, and R. Nandkishore, Phys. Rev. B **101**, 174204 (2020).

[66] S. Ok, K. Choo, C. Mudry, C. Castelnovo, C. Chamon, and T. Neupert, Phys. Rev. Research **1**, 033144 (2019).

[67] K. Bull, I. Martin, and Z. Papić, Phys. Rev. Lett. **123**, 030601 (2019).

[68] D. R. Hofstadter, Phys. Rev. B **14**, 2239 (1976).

[69] D. J. Thouless, M. Kohmoto, M. P. Nightingale, and M. den Nijs, Phys. Rev. Lett. **49**, 405 (1982).

[70] M. Aidelsburger, M. Lohse, C. Schweizer, M. Atala, J. T. Barreiro, S. Nascimbène, N. R. Cooper, I. Bloch, and N. Goldman, Nat. Phys. **11**, 162 (2015).

[71] D. Xiao, M.-C. Chang, and Q. Niu, Rev. Mod. Phys. **82**, 1959 (2010).

[72] M. V. Berry, Proc. R. Soc. Lond. A **392**, 45 (1984).

[73] A. L. Fetter, Rev. Mod. Phys. **81**, 647 (2009).

[74] Y.-J. Lin, R. L. Compton, K. Jiménez-García, J. V. Porto, and I. B. Spielman, Nature **462**, 628 (2009).

[75] J. Dalibard, F. Gerbier, G. Juzeliūnas, and P. Öhberg, Rev. Mod. Phys. **83**, 1523 (2011).

[76] F. D. M. Haldane, Phys. Rev. Lett. **61**, 2015 (1988).

[77] M. Aidelsburger, M. Atala, M. Lohse, J. T. Barreiro, B. Paredes, and I. Bloch, Phys. Rev. Lett. **111**, 185301 (2013).

[78] H. Miyake, G. A. Siviloglou, C. J. Kennedy, W. C. Burton, and W. Ketterle, Phys. Rev. Lett. **111**, 185302 (2013).

[79] G. Jotzu, M. Messer, R. Desbuquois, M. Lebrat, T. Uehlinger, D. Greif, and T. Esslinger, Nature **515**, 237 (2014).

[80] M. E. Tai, A. Lukin, M. Rispoli, R. Schittko, T. Menke, Dan Borgnia, P. M. Preiss, F. Grusdt, A. M. Kaufman, and M. Greiner, Nature **546**, 519 (2017).

[81] M. Grifoni and P. Hänggi, Phys. Rep. **304**, 229 (1998).

[82] N. Goldman and J. Dalibard, Phys. Rev. X **4**, 031027 (2014).

[83] N. Goldman, J. Dalibard, M. Aidelsburger, and N. R. Cooper, Phys. Rev. A **91**, 033632 (2015).

[84] A. Eckardt and E. Anisimovas, New J. Phys. **17**, 093039 (2015).

[85] M. Aidelsburger, S. Nascimbene, and N. Goldman, C. R. Phys. **19**, 394 (2018).

[86] A. Eckardt, Rev. Mod. Phys. **89**, 011004 (2017).

[87] N. R. Cooper, J. Dalibard, and I. B. Spielman, Rev. Mod. Phys. **91**, 015005 (2019).

[88] G. Sun and A. Eckardt, Phys. Rev. Research **2**, 013241 (2020).

[89] G. Floquet, Ann. Sci. Éc. Norm. Supér. **12**, 47 (1883).

[90] T. P. Grozdanov and M. J. Raković, Phys. Rev. A **38**, 1739 (1988).

[91] W. Magnus, Comm. Pure Appl. Math. **7**, 649 (1954).

[92] S. Blanes, F. Casas, J. A. Oteo, and J. Ros, Phys. Rep. **470**, 151 (2009).

[93] M. Bukov, L. D'Alessio, and A. Polkovnikov, Adv. Phys. **64**, 139 (2015).

[94] L. D'Alessio and M. Rigol, Phys. Rev. X **4**, 041048 (2014).

[95] A. Lazarides, A. Das, and R. Moessner, Phys. Rev. E **90**, 012110 (2014).

[96] M. Bukov, S. Gopalakrishnan, M. Knap, and E. Demler, Phys. Rev. Lett. **115**, 205301 (2015).

[97] T. Mori, T. Kuwahara, and K. Saito, Phys. Rev. Lett. **116**, 120401 (2016).

[98] D. A. Abanin, W. De Roeck, W. W. Ho, and F. Huveneers, Phys. Rev. B **95**, 014112 (2017).

[99] C. Nayak, S. H. Simon, A. Stern, M. Freedman, and S. Das Sarma, Rev. Mod. Phys. **80**, 1083 (2008).

[100] S. Sridhar, Phys. Rev. Lett. **67**, 785 (1991).

[101] C. M. Marcus, A. J. Rimberg, R. M. Westervelt, P. F. Hopkins, and A. C. Gossard, Phys. Rev. Lett. **69**, 506 (1992).

[102] P. B. Wilkinson, T. M. Fromhold, L. Eaves, F. W. Sheard, N. Miura, and T. Takamasu, Nature **380**, 608 (1996).

[103] W. W. Ho, S. Choi, H. Pichler, and M. D. Lukin, Phys. Rev. Lett. **122**, 040603 (2019).

[104] P. Schauss, M. Cheneau, M. Endres, T. Fukuhara, S. Hild, A. Omran, T. Pohl, C. Gross, S. Kuhr, and I. Bloch, Nature **491**, 87 (2012).

[105] H. Labuhn, D. Barredo, S. Ravets, S. de Léséleuc, T. Macrì, T. Lahaye, and A. Browaeys, Nature **534**, 667 (2016).

[106] P. Calabrese and J. Cardy, Phys. Rev. Lett. **96**, 136801 (2006).

[107] G. Kucsko *et al.*, Phys. Rev. Lett. **121**, 023601 (2018).

[108] S. Choi, C. J. Turner, H. Pichler, W. W. Ho, A. A. Michailidis, Z. Papić, M. Serbyn, M. D. Lukin, and D. A. Abanin, Phys. Rev. Lett. **122**, 220603 (2019).

[109] K. Bull, J.-Y. Desaules, and Z. Papić, Phys. Rev. B **101**, 165139 (2020).

[110] M. Kormos, M. Collura, G. Takács, and P. Calabrese, Nat. Phys. **13**, 246 (2016).

[111] O. Vafek, N. Regnault, and B. A. Bernevig, SciPost Phys. **3**, 043 (2017).

[112] N. Shiraishi and T. Mori, Phys. Rev. Lett. **119**, 030601 (2017).

[113] I. Lesanovsky and H. Katsura, Phys. Rev. A **86**, 041601 (2012).

[114] A. Feiguin, S. Trebst, A. W. W. Ludwig, M. Troyer, A. Kitaev, Z. Wang, and M. H. Freedman, Phys. Rev. Lett. **98**, 160409 (2007).

[115] S. Trebst, E. Ardonne, A. Feiguin, D. A. Huse, A. W. W. Ludwig, and M. Troyer, Phys. Rev. Lett. **101**, 050401 (2008).

[116] A. Chandran, M. D. Schulz, and F. J. Burnell, Phys. Rev. B **94**, 235122 (2016).

[117] Z. Lan and S. Powell, Phys. Rev. B **96**, 115140 (2017).

[118] A. Chandran, F. J. Burnell, and S. L. Sondhi, Phys. Rev. B **101**, 075104 (2020).

[119] Z. Lan, M. van Horssen, S. Powell, and J. P. Garrahan, Phys. Rev. Lett. **121**, 040603 (2018).

[120] A. Smith, J. Knolle, R. Moessner, and D. L. Kovrizhin, Phys. Rev. Lett. **119**, 176601 (2017).

[121] M. Brenes, M. Dalmonte, M. Heyl, and A. Scardicchio, Phys. Rev. Lett. **120**, 030601 (2018).

[122] F. M. Surace, P. P. Mazza, G. Giudici, A. Lerose, A. Gambassi, and M. Dalmonte, Phys. Rev. X **10**, 021041 (2020).

[123] G. Magnifico, M. Dalmonte, P. Facchi, S. Pascazio, F. V. Pepe, and E. Ercolessi, Quantum **4**, 281 (2020).

[124] F. Görg, M. Messer, K. Sandholzer, G. Jotzu, R. Desbuquois, and T. Esslinger, Nature **553**, 481 (2018).

[125] C. Schweizer, F. Grusdt, M. Berngruber, L. Barbiero, E. Demler, N. Goldman, I. Bloch, and M. Aidelsburger, Nat. Phys. **15**, 1168 (2019).

[126] K. Binder and A. P. Young, Rev. Mod. Phys. **58**, 801 (1986).

[127] L. Berthier and G. Biroli, Rev. Mod. Phys. **83**, 587 (2011).

[128] G. Biroli and J. P. Garrahan, J. Chem. Phys. **138**, 12A301 (2013).

[129] G. H. Fredrickson and H. C. Andersen, Phys. Rev. Lett. **53**, 1244 (1984).

[130] R. G. Palmer, D. L. Stein, E. Abrahams, and P. W. Anderson, Phys. Rev. Lett. **53**, 958 (1984).

[131] G. Carleo, F. Becca, M. Schiró, and M. Fabrizio, Sci. Rep. **2**, 243 (2012).

[132] W. De Roeck and F. Huveneers, Commun. Math. Phys **332**, 1017 (2014).

[133] M. Schiulaz and M. Müller, AIP Conf. Ser. **1610**, 11 (2014).

[134] N. Y. Yao, C. R. Laumann, J. I. Cirac, M. D. Lukin, and J. E. Moore, Phys. Rev. Lett. **117**, 240601 (2016).

[135] Z. Papić, E. M. Stoudenmire, and D. A. Abanin, Ann. Phys. **362**, 714 (2015).

[136] M. van Horssen, E. Levi, and J. P. Garrahan, Phys. Rev. B **92**, 100305 (2015).

[137] T. Veness, F. H. L. Essler, and M. P. A. Fisher, Phys. Rev. B **96**, 195153 (2017).

[138] A. Smith, J. Knolle, D. L. Kovrizhin, and R. Moessner, Phys. Rev. Lett. **118**, 266601 (2017).

[139] I. H. Kim and J. Haah, Phys. Rev. Lett. **116**, 027202 (2016).

[140] H. Yarloo, A. Langari, and A. Vaezi, Phys. Rev. B **97**, 054304 (2018).

[141] A. A. Michailidis, M. Žnidarič, M. Medvedyeva, D. A. Abanin, T. Prosen, and Z. Papić, Phys. Rev. B **97**, 104307 (2018).

[142] M. van Horssen, E. Levi, and J. P. Garrahan, Phys. Rev. B **92**, 100305 (2015).

[143] B. Sutherland, Phys. Rev. B **34**, 5208 (1986).

[144] M. Inui, S. A. Trugman, and E. Abrahams, Phys. Rev. B **49**, 3190 (1994).

[145] V. Oganesyan and D. A. Huse, Phys. Rev. B **75**, 155111 (2007).

[146] M. L. Mehta, *Random matrices*, Vol. 142 (Elsevier, Amsterdam, 2004).

[147] V. Alba, M. Fagotti, and P. Calabrese, J. Stat. Mech. **2009**, P10020 (2009).

[148] F. Heidrich-Meisner, S. R. Manmana, M. Rigol, A. Muramatsu, A. E. Feiguin, and E. Dagotto, Phys. Rev. A **80**, 041603 (2009).

[149] J. P. Ronzheimer, M. Schreiber, S. Braun, S. S. Hodgman, S. Langer, I. P. McCulloch, F. Heidrich-Meisner, I. Bloch, and U. Schneider, Phys. Rev. Lett. **110**, 205301 (2013).

[150] M. Greiner, O. Mandel, T. W. Hänsch, and I. Bloch, Nature **419**, 51 (2002).

[151] C. Kollath, A. M. Läuchli, and E. Altman, Phys. Rev. Lett. **98**, 180601 (2007).

[152] M. Schecter and T. Iadecola, Phys. Rev. B **98**, 035139 (2018).

[153] M. Eckholt and J. J. García-Ripoll, New J. Phys. **11**, 093028 (2009).

[154] G. Mazzarella, S. M. Giampaolo, and F. Illuminati, Phys. Rev. A **73**, 013625 (2006).

[155] U. Bissbort, F. Deuretzbacher, and W. Hofstetter, Phys. Rev. A **86**, 023617 (2012).

[156] D.-S. Lühmann, O. Jürgensen, and K. Sengstock, New J. Phys. **14**, 033021 (2012).

[157] O. Dutta, M. Gajda, P. Hauke, M. Lewenstein, D.-S. Lühmann, B. A. Malomed, T. Sowiński, and J. Zakrzewski, Rep. Prog. Phys. **78**, 066001 (2015).

[158] O. Jürgensen, F. Meinert, M. J. Mark, H.-C. Nägerl, and D.-S. Lühmann, Phys. Rev. Lett. **113**, 193003 (2014).

[159] S. Baier, M. J. Mark, D. Petter, K. Aikawa, L. Chomaz, Z. Cai, M. Baranov, P. Zoller, and F. Ferlaino, Science **352**, 201 (2016).

[160] A. Eckardt, M. Holthaus, H. Lignier, A. Zenesini, D. Ciampini, O. Morsch, and E. Arimondo, Phys. Rev. A **79**, 013611 (2009).

[161] F. Meinert, M. J. Mark, K. Lauber, A. J. Daley, and H.-C. Nägerl, Phys. Rev. Lett. **116**, 205301 (2016).

[162] H. Zhao, J. Knolle, and F. Mintert, Phys. Rev. A **100**, 053610 (2019).

[163] L. Barbiero, C. Schweizer, M. Aidelsburger, E. Demler, N. Goldman, and F. Grusdt, Sci. Adv. **5**, eaav7444 (2019).

[164] N. Pancotti, G. Giudice, J. I. Cirac, J. P. Garrahan, and M. C. Bañuls, Physical Review X **10**, 021051 (2020).

[165] H. Zhao, J. Vovrosh, F. Mintert, and J. Knolle, Phys. Rev. Lett. **124**, 160604 (2020).

[166] C. J. Fujiwara, K. Singh, Z. A. Geiger, R. Senaratne, S. V. Rajagopal, M. Lipatov, and D. M. Weld, Phys. Rev. Lett. **122**, 010402 (2019).

[167] H. M. Price and N. R. Cooper, Phys. Rev. A **85**, 033620 (2012).

[168] A. Dauphin and N. Goldman, Phys. Rev. Lett. **111**, 135302 (2013).

[169] M. Bukov and A. Polkovnikov, Phys. Rev. A **90**, 043613 (2014).

[170] H. M. Price, O. Zilberberg, T. Ozawa, I. Carusotto, and N. Goldman, Phys. Rev. B **93**, 245113 (2016).

[171] S. Mugel, A. Dauphin, P. Massignan, L. Tarruell, M. Lewenstein, C. Lobo, and A. Celi, SciPost Phys. **3**, 012 (2017).

[172] S. Choudhury and E. J. Mueller, Phys. Rev. A **92**, 063639 (2015).

[173] C. J. Kennedy, W. C. Burton, W. C. Chung, and W. Ketterle, Nat. Phys. **11**, 859 (2015).

[174] S. Lellouch, M. Bukov, E. Demler, and N. Goldman, Phys. Rev. X **7**, 021015 (2017).

[175] K. Plekhanov, G. Roux, and K. Le Hur, Phys. Rev. B **95**, 045102 (2017).

[176] S. Lellouch and N. Goldman, Quantum Sci. Technol. **3**, 024011 (2018).

[177] E. Michon, C. Cabrera-Gutiérrez, A. Fortun, M. Berger, M. Arnal, V. Brunaud, J. Billy, C. Petitjean, P. Schlagheck, and D. Guéry-Odelin, New J. Phys. **20**, 053035 (2018).

[178] K. Wintersperger, M. Bukov, J. Näger, S. Lellouch, E. Demler, U. Schneider, I. Bloch, N. Goldman, and M. Aidelsburger, Phys. Rev. X **10**, 011030 (2020).

[179] T. Boulier, J. Maslek, M. Bukov, C. Bracamontes, E. Magnan, S. Lellouch, E. Demler, N. Goldman, and J. V. Porto, Phys. Rev. X **9**, 011047 (2019).

[180] K. Lelas, N. Drpić, T. Dubček, D. Jukić, R. Pezer, and H. Buljan, New J. Phys. **18**, 095002 (2016).

[181] J. Motruk and F. Pollmann, Phys. Rev. B **96**, 165107 (2017).

[182] W. W. Ho and D. A. Abanin, arXiv e-prints (2016), arXiv:1611.05024.

[183] A. Dauphin, D.-T. Tran, M. Lewenstein, and N. Goldman, 2D Mater. **4**, 024010 (2017).

[184] T. Bilitewski and N. R. Cooper, Phys. Rev. A **91**, 063611 (2015).

[185] T. Fukui, Y. Hatsugai, and H. Suzuki, J. Phys. Soc. Jpn. **74**, 1674 (2005).

[186] Y. Kagan and B. V. Svistunov, Phys. Rev. Lett. **79**, 3331 (1997).

[187] A. Polkovnikov, Ann. Phys. **325**, 1790 (2010).

[188] H. Buljan, O. Cohen, J. W. Fleischer, T. Schwartz, M. Segev, Z. H. Musslimani, N. K. Efremidis, and D. N. Christodoulides, Phys. Rev. Lett. **92**, 223901 (2004).

[189] O. Cohen, H. Buljan, T. Schwartz, J. W. Fleischer, and M. Segev, Phys. Rev. E **73**, 015601 (2006).

[190] L. Pitaevskii and S. Stringari, *Bose-Einstein Condensation* (Clarendon Press, Oxford, 2003).

[191] C. J. Pethick and H. Smith, *Bose-Einstein Condensation in Dilute Gases* (Cambridge Univesity Press, Cambridge, 2008).

[192] M. D. S. Gardiner, N. Proukakis and M. Szymanska, *Finite Temperature and Non-Equilibrium Dynamics* (Imperial College Press, London, 2013).

[193] T. Kuwahara, T. Mori, and K. Saito, Ann. Phys. **367**, 96 (2016).

[194] D. Abanin, W. De Roeck, W. W. Ho, and F. Huveneers, Commun. Math. Phys. **354**, 809 (2017).

[195] V. Debierre, I. Goessens, E. Brainis, and T. Durt, Phys. Rev. A **92**, 023825 (2015).

[196] G. J. Milburn, J. Corney, E. M. Wright, and D. F. Walls, Phys. Rev. A **55**, 4318 (1997).

[197] S. Raghavan, A. Smerzi, S. Fantoni, and S. R. Shenoy, Phys. Rev. A **59**, 620 (1999).

[198] D. Cocks, P. P. Orth, S. Rachel, M. Buchhold, K. Le Hur, and W. Hofstetter, Phys. Rev. Lett. **109**, 205303 (2012).

[199] N. K. Wilkin and J. M. F. Gunn, Phys. Rev. Lett. **84**, 6 (2000).

[200] N. R. Cooper, N. K. Wilkin, and J. M. F. Gunn, Phys. Rev. Lett. **87**, 120405 (2001).

[201] B. Paredes, P. Fedichev, J. I. Cirac, and P. Zoller, Phys. Rev. Lett. **87**, 010402 (2001).

[202] M. Popp, B. Paredes, and J. I. Cirac, Phys. Rev. A **70**, 053612 (2004).

[203] A. S. Sørensen, E. Demler, and M. D. Lukin, Phys. Rev. Lett. **94**, 086803 (2005).

[204] E. H. Rezayi, N. Read, and N. R. Cooper, Phys. Rev. Lett. **95**, 160404 (2005).

[205] M. Hafezi, A. S. Sørensen, E. Demler, and M. D. Lukin, Phys. Rev. A **76**, 023613 (2007).

[206] B. Juliá-Díaz, D. Dagnino, K. J. Günter, T. Grass, N. Barberán, M. Lewenstein, and J. Dalibard, Phys. Rev. A **84**, 053605 (2011).

[207] B. Juliá-Díaz, T. Grass, N. Barberán, and M. Lewenstein, New J. Phys. **14**, 055003 (2012).

[208] T. Grass, B. Juliá-Díaz, and M. Lewenstein, Phys. Rev. A **89**, 013623 (2014).

[209] A. Petrescu, M. Piraud, G. Roux, I. P. McCulloch, and K. Le Hur, Phys. Rev. B **96**, 014524 (2017).

[210] M. Calvanese Strinati, E. Cornfeld, D. Rossini, S. Barbarino, M. Dalmonte, R. Fazio, E. Sela, and L. Mazza, Phys. Rev. X **7**, 021033 (2017).

[211] Y.-C. He, F. Grusdt, A. Kaufman, M. Greiner, and A. Vishwanath, Phys. Rev. B **96**, 201103 (2017).

[212] P. Rosson, M. Lubasch, M. Kiffner, and D. Jaksch, Phys. Rev. A **99**, 033603 (2019).

[213] M. Calvanese Strinati, S. Sahoo, K. Shtengel, and E. Sela, Phys. Rev. B **99**, 245101 (2019).

[214] N. Fläschner, B. S. Rem, M. Tarnowski, D. Vogel, D.-S. Lühmann, K. Sengstock, and C. Weitenberg, Science **352**, 1091 (2016).

[215] P. Ponte, A. Chandran, Z. Papić, and D. A. Abanin, Ann. Phys. **353**, 196 (2015).

[216] D. A. Abanin, W. De Roeck, and F. Huveneers, Phys. Rev. Lett. **115**, 256803 (2015).

[217] F. Machado, G. D. Kahanamoku-Meyer, D. V. Else, C. Nayak, and N. Y. Yao, Phys. Rev. Research **1**, 033202 (2019).

[218] A. Haldar, R. Moessner, and A. Das, Phys. Rev. B **97**, 245122 (2018).

[219] K. Seetharam, P. Titum, M. Kolodrubetz, and G. Refael, Phys. Rev. B **97**, 014311 (2018).

[220] M. Messer, K. Sandholzer, F. Görg, J. Minguzzi, R. Desbuquois, and T. Esslinger, Phys. Rev. Lett. **121**, 233603 (2018).

[221] A. G. Grushin, A. Gómez-León, and T. Neupert, Phys. Rev. Lett. **112**, 156801 (2014).

[222] M. Račiūnas, G. Žlabys, A. Eckardt, and E. Anisimovas, Phys. Rev. A **93**, 043618 (2016).

[223] R. B. Laughlin, Phys. Rev. Lett. **50**, 1395 (1983).

[224] F. D. M. Haldane and E. H. Rezayi, Phys. Rev. B **31**, 2529 (1985).

[225] A. Sterdyniak, N. Regnault, and G. Möller, Phys. Rev. B **86**, 165314 (2012).

[226] A. Sterdyniak, N. Regnault, and B. A. Bernevig, Phys. Rev. Lett. **106**, 100405 (2011).

[227] O. S. Zozulya, M. Haque, and K. Schoutens, Phys. Rev. A **78**, 042326 (2008).

[228] M. Haque, O. S. Zozulya, and K. Schoutens, J. Phys. A: Math. Theor. **42**, 504012 (2009).

[229] N. Regnault and B. A. Bernevig, Phys. Rev. X **1**, 021014 (2011).

[230] B. A. Bernevig and N. Regnault, Phys. Rev. B **85**, 075128 (2012).

[231] M. Bukov, M. Heyl, D. A. Huse, and A. Polkovnikov, Phys. Rev. B **93**, 155132 (2016).

[232] D. T. Tran, A. Dauphin, A. G. Grushin, P. Zoller, and N. Goldman, Sci. Adv. **3**, e1701207 (2017).

[233] A. Hudomal, I. Vasić, H. Buljan, W. Hofstetter, and A. Balaž, Phys. Rev. A **98**, 053625 (2018).

[234] C. Repellin and N. Goldman, Phys. Rev. Lett. **122**, 166801 (2019).

[235] M. Račiūnas, F. N. Ünal, E. Anisimovas, and A. Eckardt, Phys. Rev. A **98**, 063621 (2018).

[236] E. Merzbacher, *Quantum Mechanics*, 3rd ed. (Wiley, Hoboken, 1998).

Biography of the author

Ana Hudomal was born on March 8th, 1991 in Belgrade, Republic of Serbia. She completed elementary and high-school education in Belgrade. In 2010 she started BSc studies in Theoretical and Experimental Physics at the Faculty of Physics, University of Belgrade and graduated in July 2014 (GPA 10.0/10.0). She then continued with MSc studies, also at the Faculty of Physics, University of Belgrade, and defended her MSc thesis in October 2015 (GPA 10.0/10.0). The title of her MSc thesis was *"New Periodic Solutions to the Three-Body Problem and Gravitational Waves"* and it was supervised by Dr. Veljko Dmitrašinović, Research Professor at the Institute of Physics Belgrade. During her studies, she received scholarships from the National Foundation for Development of Science and Art Youth (2007-2011), the City of Belgrade (2011-2013), and the Fund for Young Talents of the Republic of Serbia (2013-2015).

In November 2015 Ana Hudomal started PhD studies in the field of condensed matter physics at the Faculty of Physics, University of Belgrade, under the supervision of Dr. Ivana Vasić, Associate Research Professor at the Institute of Physics Belgrade. Since March 2016, Ana Hudomal is employed at the Institute of Physics Belgrade as a Research Assistant at the Scientific Computing Laboratory of the National Center of Excellence for the Study of Complex Systems. During this time she participated in several research projects, including the national research project ON171017 *"Modeling and Numerical Simulations of Complex Many-Particle Systems"* funded by the Ministry of Education, Science, and Technological Development of the Republic of Serbia, and multiple bilateral projects.

Ana Hudomal has so far published five papers in peer-reviewed international journals:

1. **A. Hudomal**, I. Vasić, N. Regnault, and Z. Papić, *"Quantum scars of bosons with correlated hopping"*, Commun. Phys. **3**, 99 (2020).
2. **A. Hudomal**, N. Regnault, and I. Vasić, *"Bosonic fractional quantum Hall states in driven optical lattices"*, Phys. Rev. A **100**, 053624 (2019).
3. **A. Hudomal**, I. Vasić, H. Buljan, W. Hofstetter, and A. Balaž, *"Dynamics of weakly interacting bosons in optical lattices with flux"*, Phys. Rev. A **98**, 053625 (2018).
4. V. Dmitrašinović, **A. Hudomal**, M. Shibayama, and A. Sugita,*"Linear stability of periodic three-body orbits with zero angular momentum and topological dependence of Kepler's third law: a numerical test"*, J. Phys. A: Math. Theor. **51**, 315101 (2018).
5. V. Dmitrašinović, M. Šuvakov, and **A. Hudomal**, *"Gravitational waves from periodic three-body systems"*, Phys. Rev. Lett. **113**, 101102 (2014).

Three of these papers (1-3) are directly related to the research presented in this thesis. The other two papers (4-5) are the result of the research conducted during her MSc studies. Ana Hudomal has also presented her research through one talk and several poster presentations at international schools, workshops and conferences.

Изјава о ауторству

Име и презиме аутора – **Ана Худомал**

Број индекса – **2015/8006**

Изјављујем

да је докторска дисертација под насловом

Numerical study of quantum gases in optical lattices and in synthetic magnetic fields (Нумеричко проучавање квантних гасова у оптичким решеткама и у синтетичким магнетним пољима)

- резултат сопственог истраживачког рада;
- да дисертација у целини ни у деловима није била предложена за стицање друге дипломе према студијским програмима других високошколских установа;
- да су резултати коректно наведени и
- да нисам кршио/ла ауторска права и користио/ла интелектуалну својину других лица.

Потпис аутора

У Београду, 27. 08. 2020. год.

Изјава о истоветности штампане и електронске верзије докторског рада

Име и презиме аутора – **Ана Худомал**

Број индекса – **2015/8006**

Студијски програм – **Физика**

Наслов рада – **Numerical study of quantum gases in optical lattices and in synthetic magnetic fields (Нумеричко проучавање квантних гасова у оптичким решеткама и у синтетичким магнетним пољима)**

Ментор – **др Ивана Васић**

Изјављујем да је штампана верзија мог докторског рада истоветна електронској верзији коју сам предао/ла ради похрањивања у **Дигиталном репозиторијуму Универзитета у Београду.**

Дозвољавам да се објаве моји лични подаци везани за добијање академског назива доктора наука, као што су име и презиме, година и место рођења и датум одбране рада.

Ови лични подаци могу се објавити на мрежним страницама дигиталне библиотеке, у електронском каталогу и у публикацијама Универзитета у Београду.

Потпис аутора

У Београду, 27. 08. 2020. год.

Ana Hudomal

Изјава о коришћењу

Овлашћујем Универзитетску библиотеку „Светозар Марковић“ да у Дигитални репозиторијум Универзитета у Београду унесе моју докторску дисертацију под насловом:

Numerical study of quantum gases in optical lattices and in synthetic magnetic fields (Нумеричко проучавање квантних гасова у оптичким решеткама и у синтетичким магнетним пољима)

која је моје ауторско дело.

Дисертацију са свим прилозима предао/ла сам у електронском формату погодном за трајно архивирање.

Моју докторску дисертацију похрањену у Дигиталном репозиторијуму Универзитета у Београду и доступну у отвореном приступу могу да користе сви који поштују одредбе садржане у одабраном типу лиценце Креативне заједнице (Creative Commons) за коју сам се одлучио/ла.

1. Ауторство (CC BY)

2. Ауторство – некомерцијално (CC BY-NC)

3. Ауторство – некомерцијално – без прерада (CC BY-NC-ND)

④ **Ауторство – некомерцијално – делити под истим условима (CC BY-NC-SA)**

5. Ауторство – без прерада (CC BY-ND)

6. Ауторство – делити под истим условима (CC BY-SA)

(Молимо да заокружите само једну од шест понуђених лиценци.
Кратак опис лиценци је саставни део ове изјаве).

Потпис аутора

У Београду, 27. 08. 2020. год.

Ана Худомал

1. **Ауторство**. Дозвољавате умножавање, дистрибуцију и јавно саопштавање дела, и прераде, ако се наведе име аутора на начин одређен од стране аутора или даваоца лиценце, чак и у комерцијалне сврхе. Ово је најслободнија од свих лиценци.

2. **Ауторство – некомерцијално**. Дозвољавате умножавање, дистрибуцију и јавно саопштавање дела, и прераде, ако се наведе име аутора на начин одређен од стране аутора или даваоца лиценце. Ова лиценца не дозвољава комерцијалну употребу дела.

3. **Ауторство – некомерцијално – без прерада**. Дозвољавате умножавање, дистрибуцију и јавно саопштавање дела, без промена, преобликовања или употребе дела у свом делу, ако се наведе име аутора на начин одређен од стране аутора или даваоца лиценце. Ова лиценца не дозвољава комерцијалну употребу дела. У односу на све остале лиценце, овом лиценцом се ограничава највећи обим права коришћења дела.

4. **Ауторство – некомерцијално – делити под истим условима**. Дозвољавате умножавање, дистрибуцију и јавно саопштавање дела, и прераде, ако се наведе име аутора на начин одређен од стране аутора или даваоца лиценце и ако се прерада дистрибуира под истом или сличном лиценцом. Ова лиценца не дозвољава комерцијалну употребу дела и прерада.

5. **Ауторство – без прерада**. Дозвољавате умножавање, дистрибуцију и јавно саопштавање дела, без промена, преобликовања или употребе дела у свом делу, ако се наведе име аутора на начин одређен од стране аутора или даваоца лиценце. Ова лиценца дозвољава комерцијалну употребу дела.

6. **Ауторство – делити под истим условима**. Дозвољавате умножавање, дистрибуцију и јавно саопштавање дела, и прераде, ако се наведе име аутора на начин одређен од стране аутора или даваоца лиценце и ако се прерада дистрибуира под истом или сличном лиценцом. Ова лиценца дозвољава комерцијалну употребу дела и прерада. Слична је софтверским лиценцама, односно лиценцама отвореног кода.